Controlling chemotaxis: A study on novel migration behaviours in multi-signal systems

Adam Oliver Duncan Dowdell

MSci, Applied Mathematics and Physics

Thesis submitted in fulfilment of the requirements for the degree of Doctor of Philosophy

University of Glasgow

College of Medical, Veterinary and Life Sciences

March 2022

Abstract

Directed cell motility plays a crucial role at some stage for most forms of life. Single celled organisms rely on finely controlled motion to hunt or migrate toward optimum environmental conditions. Multicellular organisms require a continual system of simultaneous - and precise - cellular migration, from conception until death, simply in order to develop and survive. These migrations are most often modulated via diffusible extracellular signals, causing the affected cell to move towards or - rarely - away from the source of the signal; this is chemotaxis. The primary aim of this thesis is to come to a fundamental understanding of the relationship between chemotactic signals and the elicited cellular response, from basic singular signals to complex multi-signal systems, and use this knowledge to predict novel migration behaviours. This is achieved using a feedback loop between an iterative process of mathematical modelling, to predict chemotactic responses, and live cell imaging, to validate and improve upon the model. Assays are performed using Insall chambers, a direct visualisation chemotaxis chamber, and the motile amoeba *Dictyostelium discoideum*. A diverse range of extracellular signalling conditions are constructed via the varying chemotactic properties of different derivatives of cAMP, a signalling molecule to which *D. discoideum* are highly chemotactic. Using mathematics as an interface between chemical concentration and subsequent cell-surface receptor activation, many complex migration behaviours were predicted and experimentally verified. Of particular interest are: a robust system by which chemorepulsion - the mechanics of which have been elusive - can be mediated, conditions that can give rise to an inversion of chemotactic directionality in the same gradient, and proof that two signals that cause chemoattraction in isolation can be combined to induce chemorepulsion.

Acknowledgements

Firstly, I would like to thank my supervisor, Robert Insall, for giving me the opportunity to embark on such an exciting, multi-disciplinary research project. It has been such a thrill to apply the knowledge I gained throughout a degree in mathematics and physics to the more unpredictable world of biology, and a real pleasure to have the freedom to put on a lab coat and actually test the validity of mathematical predictions. It has also been great fun putting our heads together and batting around ideas on mathematics and biology in an attempt to unravel some of the mysteries of chemotaxis, and very satisfying when the collaboration has borne fruit. He has been a most wonderful support both scientifically and relative to personal struggles I have experienced over the course of my PhD.

Next I would like to thank Peter Thomason who, despite numerous responsibilities, always found the time to discuss my problems with me and help in any way he could. His unending knowledge, patience and support played a big role in making my PhD experience as manageable as it was, and his companionship contributed largely to making my time in the lab fun and enjoyable. On a similar note I would also like to thank Luke Tweedy for his help regarding anything maths; his extensive expertise streamlined many arduous processes and discussions with him always proved very insightful and helpful. He has been a fantastic support in my research and a lot of fun to collaborate with. I would also like to thank everyone else both in my lab and our adjacent lab, the Laura Machesky group. Everyone is so supportive and friendly and it has provided, simultaneously, the most enjoyable and efficient work environment you could really ask for.

On a more personal note, I would also like to thank my mother and father, who are are always there to offer words of encouragement and pick me up when things get a little much. Their unwavering support provides a foundation on which I have often found hidden reserves of determination and positivity. I would also like to thank all of my amazing friends, who are always there if I need them and provide endless laughter and fun outside of the lab. These fulfilling moments undoubtedly refresh my enthusiasm for my work, so they definitely contributed to making my PhD a smoother experience. Finally, I would like to thank my incredible partner Florencia Scotti; she is my rock and has been there by my side through all the ups and downs relative to both my work and my personal life. Knowing I come home to her makes any day much more manageable.

Author's declaration

I hereby declare that the contents of this thesis have been composed solely by myself, except where explicitly stated otherwise by reference or acknowledgement. No aspect of this work has been submitted for any other degree or professional qualification.

List of Abbreviations

1D: 1-dimensional
2D: 2-dimensional
3D: 3-dimensional
8-CPT-cAMP: 8- (4- Chlorophenylthio)adenosine- 3', 5'- cyclic monophosphate
AprA: autocrine proliferation repressor protein A
Arp2/3: actin related protein 2/3
ATP: adenosine triphosphate
BC: boundary condition
$CaCl_2$: calcium chloride
cAMP: cyclic adenosine monophosphate
cAR: cAMP receptor
Che: chemotaxis protein
CXCL12: C-X-C motif chemokine 12
CXCR4: C-X-C motif chemokine receptor 4
D. discoideum: *Dictyostelium Discoideum*
Dock: dedicator of cytokinesis
E. coli: *Escherichia coli*
Elmo: engulfment and cell motility
EGF: epidermal growth factor
fAR: folic acid receptor
Flim: flagellar motor switch protein
GDP: guanosine diphosphate
GEF: guanine-nucleotide exchange factor
GPCR: G-protein-coupled receptor
GTP: guanosine triphosphate
K. aerogenes: *Klebsiella aerogenes*
K_2HPO_4: dipotassium phosphate
KH_2PO_4: monopotassium phosphate
LHS: left hand side
MCP: methyl-accpeting chemotaxis protein
$MgCl_2$: magnesium chloride
NC4: North Carolina 4
PDGF: platelet derived growth factor
PI3K: phosphoinositide 3-kinase
PIP_2: phosphatidylinositol (4,5)-bisphosphate
PIP_3: phosphatidylinositol (3,4,5)-trisphosphate
Ras: rat sarcoma protein
RHS: right hand side

Rp-cAMPS: Adenosine- 3', 5'- cyclic monophosphorothioate, Rp- isomer
RTK: receptor tyrosine kinase
Sp-8-CPT-cAMPS: 8- (4- Chlorophenylthio)adenosine- 3', 5'- cyclic monophosphorothioate, Sp- isomer
Sp-cAMPS: Adenosine- 3', 5'- cyclic monophosphorothioate, Sp- isomer
vs: versus
WASP: Wiskott-Aldrich syndrome protein

Units

$^{\circ}C$: degrees Celsius
μm: micro-metre
mm: milli-metre
nM: nano-molar
μM: micro-molar
mM: milli-molar
ml: milli-litre
s: second
min: minute
rpm: revolutions per minute

Mathematics

α: intrinsic efficacy
δ: rate of change of fractional proportion of active receptors with space
Ω: fractional proportion of active receptors
∇^2: Laplacian
A, B: constants of integration
C: ligand concentration
D: diffusion coefficient
G: bound receptor complex concentration
k: bound complex association rate
k_{-}: bound complex dissociation rate
K_d: dissociation constant
K_m: Michaelis-Menten constant
L: bridge length
M_C: mass of substance with concentration C
M: chemical gradient steepness
n: number of considered ligands
N: number of cells in the source

Q: degradation parameter in high concentration limit $C >> K_m$

R: degradation parameter in low concentration limit $C << K_m$

t: time

U: unbound receptor concentration

V: volume of the source

V_{max}: maximum rate of degradation

W: cell length

x: distance in x-direction

y: distance in y-direction

z: distance in z-direction

List of Figures

Contents

1 Introduction

1.1 Chemotaxis

The biased migration of motile cells in response to a gradient of a diffusible substance - or chemotaxis - is arguably one of the most critical aspects of cell biology. The activation of cell signalling systems, and subsequent migration, account for a multitude of vitally important developmental, immunological and nourishing processes in both single cell and multicellular organisms [1]. Chemotaxis relies on a sophisticated cocktail of detection, response and feedback systems acting in unison to drive cells, in general, towards a source of chemical stimulus [2]. This type of migration, in the direction of increasing chemical concentration, is known as chemoattraction, with the corresponding chemical stimulus being referred to as a chemoattractant. More rarely, cells may instead travel down the chemical gradient [3]; this is known as chemorepulsion. These behaviours are not be confused with chemokinesis, characterised by a chemically induced increase in random motion [4]. Chemotaxis is of such great import that many correspodingly detrimental conditions can arise if it is performed incorrectly [5].

1.1.1 Immune System Responses

Perhaps one of the most immediately relevant applications of chemotaxis is that of leukocyte migration. Without the ability to sense minute differences in chemoattractant concentration, immune cells would be incapable of detecting sites of infection and otherwise harmless pathogens could run rampant in the body [6]. The neutrophil is the most abundant leukocyte in the body, comprising around 60% of all immune cells, and resides in the bloodstream until chemokines - secreted from a site of infection - are detected [7]. These chemokines, naturally, act as a chemoattract and cause the neutrophils to migrate out of the vasculature and towards the site of inflammation, at which point they digest the foreign body via phagocytosis [8]. Typically, neutrophils combat bacterial or fungal infections [9, 10]. The second most abundant type of immune cell are the lymphocytes, comprising around 30% of leukocytes in the form of B cells and T cells and constituting the adaptive aspect of the immune system, allowing for effective response to practically any form of infection [7]. B cells, for instance, produce pathogen specific antibodies in response to foreign antigens, which then circulate around the body and bind to the corresponding pathogen that stimulated its production, both blocking the target from binding to host cells and marking the target for phagocytic destruction [11]. T cells are specialised to identify host cells which have been infected by a pathogen, through antigens on the cell surface [12]. Once identified, T cells can elicit a multitude of responses including killing the infected cell, recruiting phagocytes or stimulating B cells to aid elimination of the pathogen [13, 14]. Regardless of the method the immune system employs to protect the body from infection, it is clear that biased migration to sources of stimulus, and so chemotaxis, is of vital importance [15]. In cases of extreme systematic inflammation, or sepsis, correct neutrohpil chemotaxis becomes even more vital, with small

deviations from normal function being potentially fatal [16].

1.1.2 Embryonic Development

Aside from contributing hugely to the defence systems of the body, chemotaxis functions as a critically important aspect for many more fundamental biological processes. Perhaps at the forefront of these could be migration of neural crest cells during embryogenesis, ultimately forming the basis of the central nervous system. Each neural crest cell undertakes a specific, heavily regulated, journey to key positions in the embryo where they settle and differentiate into a diverse range of cell types [17]. These include pigment cells, endocrine cells, muscle, bone, tendons, glial cells and neurons [18]. Of particular interest is cellular migration in the developing cerebral cortex, given that the brain is not only the most complex of bodily structures but also, arguably, the most important. Beginning from the neural tube, the progenitors of both glial cells and neurons, neuroepithelial cells, migrate outwards and differentiate [19]. Glial cells form the structural framework of the cerebrum, with neurons migrating along the radial glial cells to their appropriate niche within the developing cortex [20]. The neurons settle in a layered fashion, with the oldest neurons located closest to the lumen and newer ones crawling further out [21]. Chemotaxis becomes critically important during this process, guiding neurons to their correct location and ensuring healthy cerebral development [22]. Specific ligands aid this purpose; for instance neurotrophic factor, which binds to the receptor TrkB and elicits typical migratory morphology in neurons [23]. Once nestled, neurons will then extend out their axons and dendrites; this essentially allows neurons to talk to each other as well as other aspects of the body, such as the muscles [7]. Chemotaxis, unsurprisingly, also plays a role in axonal migration, ensuring that the nervous system is correctly connected [24]. In these kinds of cases, a chemotaxis failure could have catastrophic implications for both brain function and morphology. One resultant condition that can arise from a neuron migration defect is schizencephaly, characterised by unusual clefts in either one or both of the cerebral hemispheres [25]. Patients with a singular cleft are observed to have weakness in one side of the body, or hemiparesis, and at least mild mental deficiencies, and cases with bilateral clefts experience a weakness in all limbs, or tetraparesis, and suffer from severe mental deficiencies [26]. Other key migratory processes in the developing embryo, modulated via chemotaxis, include primordial germ cell migration to the gonadal precursors - leading to the formation of the reproductive system - and myoblast migration to limb buds, contributing to the development of the musculoskeletal system [27, 28]. The chemokine CXCL12, with corresponding receptor CXCR4, has been identified as a key guidance factor for both primordial germ cells and myoblasts [29, 30].

1.1.3 Further Significance

The functional diversity of chemotaxis is truly enormous, with many pathways and applications still waiting to be discovered. Encapsulating even a small fraction of the significance of chemotaxis, across all walks of biology, could easily take up an inordinate portion of this

thesis. With this in mind, however, there are perhaps a few more key implementations of chemotactic systems that are worth noting. Firstly is that of wound healing, wherein chemical stimuli - such as platelet derived growth factors (PDGFs), epidermal growth factor (EGF) and other cytokines - are produced from the bleed controlling clot that forms [31]. As bleeding comes under control, these stimuli act as a chemoattractant guide for inflammatory cells - such as neutrophils, macrophages and lymphocytes - to then aid in clearing away invading bacteria, apoptotic cells and recruiting further leukocytes [32]. Incredibly, as inflammation is resolved, macrophages undergo a functional transition to instead promote regeneration of the damaged tissue, such as by producing a collagen precursor to aid in the reconstruction of the extracellular matrix [33]. Following this, platelets and macrophages produce stimulants for both the chemotaxis and proliferation of endothelial cells, producing a barrier against further infection and bodily fluid loss [34]. As well in this stage, many fibroblasts chemoattract into the site of the wound from surrounding tissues - stimulated primarily by PDGFs and EGF - and synthesise large amounts of collagen help remodel the damaged tissue [35]. If this highly regulated process were to be compromised, for instance via some chemotaxis failure, then wound healing defects can arise [36]. In such cases, wounds can become non-healing and enter a dangerous cycle of self-sustaining inflammation, carrying with it a significant risk of mortality [37].

Next, it is worth mentioning that chemotaxis does not always function to the benefit of the organism in question, as is clearly demonstrated in the case of cancer metastasis, where cells from a malignant cancer tumour invade the surrounding tissue, potentially entering the blood or lymphatic system, and form a secondary cancer somewhere else in the body [38]. Most often it is these metastases that kill a cancer patient [39]. For this case, increased chemotactic prowess translates directly into an increased risk of fatality, due to more effective cancer cell dissemination [40]. CXCL12 also becomes relevant once again as its primary receptor, CXCR4, is expressed in several forms of cancer cell, suggesting that CXCL12 signalling could play a role in cancer invasion and metastasis [41].

1.1.4 Chemorepulsion

A much rarer form of chemotaxis, chemorepulsion is characterised by biased migration away from a source of stimulus. This type of behaviour has been observed in both neurons and neutrophils, suggesting that chemorepulsion could play a role in both cerebral development and the immune system [42, 43]. In the case of neutrophils, despite their intrinsic function of helping the body fight infection, their accumulation at sites of inflammation can actually cause tissue damage, contributing to conditions such as chronic obstructive pulmonary disease [44]. It is in cases such as this that reverse migration of neutrohpils, back into the vasculature, becomes vitally important, with a chemorepulsion failure resulting in an exacerbation of neutrophilic inflammation [45]. Reverse migration is also relevant in other aspects of the immune system, with T-cells being observed to chemorepel away from sources of CXCL12 [46]. It has been shown that tumours expressing high levels of CXCL12 can sub-

sequently repel T-cells, allowing some level of malignant tumour immunity from the natural defence systems of the body [47]. Chemorepulsion is also observed outside of mammalian cell biology, for instance in the soil dwelling amoeba *D. discoideum* [48]. These unicellular organisms have been observed to repel away from each other while in a vegetative state - suggesting the presence of cell secreted chemorepellents [49] - as well as from 8-CPT-cAMP [50], an analogue of the chemoattractant cAMP. Chemorepulsion in vegetative *D. discoideum* is likely explained by autocrine proliferation repressor protein A (AprA), a secreted protein for which colonies of AprA$^-$ cells remain much more closely packed while wild-type colonies disperse radially much more readily [51]. Bacterial chemotaxis, explained in detail further on, accommodates a unique mode of migration away from a source of stimulus that involves temporal distruption of a flagella motor to periodically randomise motion [52]. The direction of motion is randomised very frequently in regions of high repellent concentration and decreases as repellent concentration similarly decreases, leading to larger periods of uninterrupted swimming as the bacteria moves away from the repellent [53]. Irrespective of whether chemorepulsion is of benefit or detriment, it is clear that reverse migration is of utmost importance in the field of chemotaxis.

1.2 Cell Signalling

So far, only the most basic picture of cell signalling has been drawn; some cell expresses a receptor that binds a specific molecule, eliciting a directional response. For a cell in the body this type of simplification is laughable. In reality a cell is immersed in a vast multitude of signalling molecules and expresses an array of function specific receptors, binding only those signalling molecules that are important for the regulation of the cell under question [54]. The various types of receptors that a cell expresses essentially selects which ligands, out of a maelstrom of extracellular stimuli, the cell can see and respond to [55]; they can be viewed as the sensory apparatus of the cell, much like the eyes, nose and ears of a human. As such, the specific receptors expressed by different cells have huge implications for their capabilities and function, of which biased motility is only a small part [56]. Signalling molecules can elicit many other types of cellular response, including differentiation and division, and in some cases the presence of specific ligands is necessary simply for cell survival [57]. When one accounts for the fact that these signals may act in unison, it becomes clear that a practically infinite arsenal of complex changes and decisions is possible. However important chemotaxis may be, it is still just a single cog in much larger machine.

1.2.1 Methods of Signalling

Cell signalling varies hugely in terms of receptor and ligand type, as well as method of ligand delivery, with permutations of these factors meaning that cellular communications can be brought about in a plethora of different ways [58]. A strong starting point, however, is the different types of receptors that a cell can express. Receptors are cell proteins that bind extracellular signal molecules, or ligands, and fall into two primary categories: intra-

cellular and cell-surface. Intracellular receptors, located in the cell cyoplasm, are the least common of the two and bind small hydrophobic ligands that can diffuse through the plasma membrane, such as steroids [59]. Once bound and active, these receptor-ligand pairs often act to mediate gene expression, promoting synthesis of specific proteins through mRNA transcription [60]. Important examples of this class of receptor are the progesterone and mineralocorticoid steroid receptors [61, 62]. Cell-surface receptors are the most prevalent form of receptor, usually binding some sort of extracellular molecule that cannot enter the cytoplasm, transducing this signal into an intracellular one and activing one or more intracellular signalling pathways which ultimately mediates the change in cell behaviour [63]. They fall into three subclasses: ion-channel-coupled receptors, enzyme-coupled receptors and G-protein-coupled receptors. Ion-channel-coupled receptors are a machinery that essentially operates a hydrophilic ion-channel, modulated via receptor-ligand binding, which allows various ions to cross the plasma membrane [64]. Ligand binding can either open or close the channel, depending on the signalling function, but always serves to change the target cell excitability; this then interferes with the activity of voltage sensitive molecules inside the cell, inducing the cell response [65]. This type of receptor has been observed to be upregulated in immune cells during inflammation, binding ATP released from damaged cells and releasing inflammatory cytokines to enhance the immune response [66]. Enzyme-coupled receptors either function directly as enzymes or have an intracellular domain which interacts with an enzyme; these enzymes are, for the most part, protein kinases, and instigate a cellular response by phosphorylating specific proteins in the cell [67]. A particularly important class of enzyme-coupled receptors are receptor tyrosine kinases (RTKs), which bind a large range of growth factors and hormones and phosphorylate only the amino acid tyrosine [68]. They influence a wide range of key biological processes including cell proliferation, differentiation, and regulation of metabolic homeostasis [69]. This means that incorrect RTK activity can have a correspondingly negative impact on the body, giving rise to some cancers [70]. G-protein-coupled receptors (GPCRs) are of particular interest to this work and, as such, shall be covered in depth in a subsequent section.

Aside from functional differences between receptor types, it is also important to consider the processes by which signalling molecules are delivered to target cells, which vary substantially in range and method and fall into five primary signalling classes: contact-dependent, paracrine, autocrine, synaptic and endocrine. Contact-dependent signalling occurs when the signal molecule remains bound to the surface of the signalling cell, meaning that contact between the signalling and target cell is required for receptor-ligand binding, and the desired change in cell behaviour, to occur [71]. As contact-dependent signalling acts over the shortest possible distance, between signal and target cell, it is especially important in early stages of deveopment, when distances are relatively small [72]. This type of communication can also occur over larger distances, however, as in the case of Eph RTKs - an important receptor in axon migration and growth - which have been observed to interact with cell-surface Eph receptor ligands [73]. Paracrine signalling is a mid-range form of cellular

communication in which the signal and target cell are located in a local extracellular environment [74]. Signalling molecules corresponding to this type of communication are known as paracrine factors, and, intuitively, diffuse only over relatively short distances, affecting only neighbouring cells [75]. Autocrine signalling is then essentially a sub-type of paracrine signalling, wherein the target and signal cells are of the same type, stimulating their own response [76]. This type of feedback mechanism has been observed in immune cells, both secreting and responding to ATP [77], and in cancer cells, where this type of autocrine loop acts in a detrimental fashion by promoting metastasis [78]. Synaptic signalling is a form of cellular communication that utilises nerve cells, which, due to their length and connectivity, allows delivery of signal molecules over a very large range [58]. Stimulated neurons will send electrical impulses along the axon to the synapse located at the very end, stimulating the secretion of neurotransmitters which act as ligands for ion-channel-coupled receptors on the target cell [79]. The synapse and post synaptic target cell are usually very closely packed, ensuring that secreted ligands bind only to the desired target cell [7]. As this type of signalling involves a series of electrical impulses, it is only natural that ion-channel-coupled receptors are the target receptors for secreted neurotransmitters, changing the excitability of the post synaptic cell by varying the ion permeability of the plasma membrane [80]. The density of ion-channel-coupled receptors of the post synaptic cell directly correlates with the magnitude of excitation that can be achieved, and effectively specialises the communication between any two neurons [81]. Synaptic plasticity, defined as the ability of neurons to alter the strength of this communication - which must clearly relate to neurotransmitter receptor density - has then been postulated to be of vital contribution to the memory capacity of the brain [82]. The final method of ligand delivery, endocrine signalling, also acts across large distances in the body, but by a very different method: the bloodstream [83]. In this case the signalling cell is an endocrine cell, usually located in the brain, and their signalling molecules are hormones, which, once in the bloodstream, can be carried to any part of the body with ease [84]. Due to the nature of this form of transport, however, the delivery of hormones is slow and concentrations are diluted to a large degree, meaning that target receptors must be able to detect very small concentrations of ligand [85]. Examples of important hormones delivered via endocrine signalling are thyroxine, which impacts metabolic rate [86], and calcitonin, which contributes to calcium homeostasis [87].

1.2.2 G-Protein Coupled Receptors

GPCRs are the most diverse class of cell-surface receptors, mediating a huge range of responses to similarly large range of signalling molecules. To name but a few, GPCRs respond to: light, neurotransmitters, chemokines, hormones and both taste and odour molecules [88, 89]. This means that GPCRs allow for much of the human experience, contributing hugely to sight, smell, taste, growth, mood and much more. Surprisingly, despite an enormous range of function, GPCRs all share a very similar morphology; a single polypeptide chain that weaves across the plasma membrane 7 times, with a receptor binding site usually located at the center [90]. As such, GPCRs are also known as 7-transmembrane receptors.

The polypeptide chain is then coupled to a trimeric G-protein, comprising of an α, β and γ subunit, which can bind either GTP or GDP, via the α subunit, putting the GPCR into an active or inactive state, respectively [91]. When a signal molecule binds to the receptor, a conformational change is induced in the intracellular loops of the transmembrane receptor, altering the protein structure and causing the α subunit of the linked G-protein to exchange GDP for GTP [92]. This then causes the α subunit to dissociate from the $\beta\gamma$ dimer, both of which then seek out target proteins, or second messengers, to relay to signal further, instigating one or more intracellular signalling pathways which ultimately elicits the cellular response [93]. An important, subsequent, aspect of GPCR function is desensitisation, limiting GPCR signalling to avoid unwanted affects such as cellular toxicity [94]. This is accomplished via a combination of GPCR kinases, which phosphorylate active receptors and terminate signalling via G-proteins, and arrestins, which block the coupling of G-proteins to their corresponding receptors [95].

A common second messenger in many GPCR signalling pathways is cAMP, of which variation in intracellular levels can mediate a large range of responses [96]. Extracellular signals can function to either stimulate, activating adenylyl cyclase to synthesise cAMP from ATP, or inhibit, decreasing the catalytic activity of adenylyl cyclase and slowing cAMP synthesis, cAMP production [97]. In the case of the adrenal hormone epinephrine, GPCR binding stimulates cAMP production in heart cells, mediating an increase in heart rate, blood pressure and blood sugar levels in preparation for a flight-or-fight response [98]. Thyroid-stimulating hormone similarly increases levels of intracellular cAMP in the thyroid gland, leading to thyroid cell proliferation and contributing to correct correct thyroid hormone regulation [99]. CXCL12 signalling through the GPCR CXCR4 acts to inhibit adenylyl cyclase - lowering levels of intracellular cAMP - as well as activate phosphoinositide 3-kinase (PI3K), contributing to biased cell migration [100, 101].

1.2.3 Complexities in Receptor Activation

A very intuitive and comfortable assumption would be that each bound ligand causes the correspondingly bound receptor to become active, initiating a specific cellular response. This is, however, a rather simplistic and inflexible model that does not account for any intricacies or inconsistencies in receptor activation that may be elicited by certain ligands [102]. A trivial, but very important, first point to make is that GPCRs exist exclusively in either an active or inactive state [103]. Inactive receptors, naturally, transmit absolutely no information to the cell, whereas active receptors mediate a cascade of intracellular signalling pathways - eliciting a cellular response[104]. A next important point of interest is that unbound receptors can exist in both inactive and constitutively active states, which leads to three distinct ligand classifications - corresponding to their proportional effect on receptor activity [105]. The first, and most common, is that of a positive agonist. This refers to any ligand which causes a proportion of bound, previously inactive, receptors to become active. Second are inverse agonists, which, upon binding to constitutively active receptors, cause a proportion

to become inactive. Lastly are antagonists, which compete for ligand binding sites but elicit absolutely no change in receptor activity. When constitutively active receptors are taken out of consideration inverse agonists and antagonists serve the same function. Ligands exhibiting positive agonism can be further split into two classes: full agonists - any ligand which activates all bound receptors - and partial agonists - any ligand which activates a proportion of bound receptors, eliciting a sub maximal response [106]. This naturally leads one away from the concept of simple and exclusive agonism, as there are clearly discrepancies in activation profiles for different receptor-ligand pairs [107]. Much more sensible is to adopt a concept of variable agonism, accounting for differences in ligand induced receptor activation that can lead to variation in the cellular response.

1.3 Chemotactic Mechanisms

Of particular interest in this thesis are GPCRs specialised to mediate chemotaxis, allowing cells to sense extracellular gradients and migrate towards their source [108, 109]. These types of GPCRs bind signal molecules in the gradient, and, given the distribution of chemotactic receptors is approximately even across the cell surface [110, 111] - meaning that more receptors will be bound and active on the side of the cell closest to the signal source - induce cellular motion in the direction of increasing levels of receptor activation, towards the source of the stimulus. Note that if the concept of variable agonism is applied to this situation, with various chemotactic ligands eliciting different receptor activation profiles, then surely the direction of increasing receptor activation - and ultimately the chemoactic bias - can be modulated in complex and novel ways. This is, however, jumping a little bit in the story. Regardless of how discrepancies in receptor activation may relate to overall chemotactic response, there are a number of chemotaxis specific intracellular signalling pathways that must first be activated before the cell can even begin to move with any kind of bias [112].

1.3.1 Migration in D. discoideum

D. discoideum has long been used as a friendly tool to dissect the complex signalling pathways and internal machinery that underlie chemotaxis [113]. This is mainly due to the ease by which they can be cultured and genetically altered, as well as their innate motility [114]. Biased motility begins with the detection of a chemotactic ligand and, after a series of intracellular signalling pathways, follows with the dynamic polymerisation of actin filaments at the edge of the cell receiving the signal [115]. This forces the plasma membrane outwards in a protrusion, or a pseudopod in the case of *D. discoideum*, which instigates the physical motion of the cell in the response to the signal [116]. This protrusion, in the direction of the chemical stimulus, is known as the leading edge. In order for the cell to move in a directionally biased fashion, consecutive pseudopod extensions must be coupled with retractions of the cell rear, the contracile force of which is mediated by myosin localised in the cell uropod [117]. It is worth noting that *D. discoideum* will also create pseudopods in the absence of chemical stimuli, constitutively moving in search of a signal [118], however

directionaly persisent migration will only occur in the presence of a stimulus. This retraction and contraction is coupled with continual actin disassembly at the leading edge, resulting in a treadmill effect and a retrograde flow force that acts towards the center of the cell, likely aiding in cellular propulsion [119]. Effective chemotaxis also requires the cell to maintain polarity, a clear morphological distinction between the front and back of the cell, as it is the consistent coordination between the two functionally distinct ends of the cell that allows for persistent locomotion [120]. A properly polarised cell becomes stretched in the direction of the signal, essentially amplifying the sensitivity of the cell by furthering the difference in receptor activation between the cell extrema [121]. This amplified signal at the leading edge of a polarised cell encourages consecutive leading pseudopods to form very close to each other, allowing for more efficient migration [122]. This implies a sort of feedback loop between polarisation, directionally consistent pseudopod formation and chemotactic efficacy, which can be confirmed by the observation that polarisation becomes strengthened in bouts of extended chemotaxis [123]. Additionally, myosin has been observed to accumulate at the sides of the cell during chemotaxis [124], providing a means to suppress the emergence of lateral pseudopodia and reinforce cellular polarity.

The exact biological pathways that mediate these behaviours are a matter of some debate, but there are some key players of definite worth discussing. As mentioned previously, the first stage in biased migration is the binding of chemotaxis specific signalling molecules. For *D. discoideum*, perhaps the most crucial of these is cAMP. There are four GPCRs that bind cAMP, cAR1-4; cAR1 and cAR3 are expressed in early deveopment and have high cAMP affinities, overlapping in function to mediate cAMP chemotaxis; cAR2 and cAR4 are important in later developmental events, when cells have aggregated to form a multicellular slug and further differentiate to become a fruiting body [125]. All of these receptors use a single form of $G\beta\gamma$ subunit, which is essential in activating the downstream signalling events necessary for chemotaxis [126]. Eleven $G\alpha$ subunits have been identified, of which only $G\alpha_2$, linked to the cAR1 receptor, has any substantial impact on mediated migration, suggesting that cAR1 is the most important *D. discoideum* receptor for cAMP chemotaxis [127]. Of great importance in subsequent signalling pathways are Ras GTPases, activated via free $G\beta\gamma$ [128]. This is clear from the fact that elimination of rasG and rasC effectively terminates any sort of directional motion [129], insinuating that some combination of Ras target proteins is absolutely crucial for biased migration. One such family of target proteins are PI3Ks, which convert PIP_2 to PIP_3, a protein which is observed to be strongly enriched at the leading edge of migrating cells [130]. As this localisation coincides with new actin polymerisation, a popular hypothesis is that PIP_3 must play a pivotal role in biased migration [131]. This hypothesis is strongly reinforced by the link between PIP_3 and Rac, a similarly enriched protien at the leading edge, which has been proven beyond doubt to be crucial for actin polymerisation and chemotaxis, with Rac null cells expressing crippling chemotactic defects [132]. Rac is activated by guanine-nucleotide exchange factors (GEFs), target proteins of PIP_3 [133], and further stimulates members of the Wiskott-Aldrich syndrome

(WASP) family of proteins [134]. WASP proteins then mediate the formation of branched actin networks by activating the Arp2/3 complex [135], which effectively binds to and structurally organises actin filaments. Despite this strong argument for the importance of the PI3K pathway, however, cells lacking all PI3K genes are still capable of effective chemotaxis, albeit with with a reduction in both orientation and movement speed [136]. It has further been suggested that PIP_3 localisation aids in confining new pseudopod generation in the direction of a signal, implying that PIP_3s primary function may instead be the induction and stability of cell polarity, promoting quick responses and directionally consistent migration [137]. So, while the PI3K pathway may be an important contributor to effective chemotaxis, there are clearly alternative pathways that can either compensate in the absence of PI3K or are the primary mediators of chemotaxis. An example of one such potential pathway is Rac activation via Elmo/Dock complexes, which are targeted by $G\beta\gamma$ subunits upon receptor stimulation, providing an alternative signalling pathway linking receptor-ligand binding to the actin cytoskeleton, and chemotaxis [138].

1.3.2 Variations in Chemotactic Method

The style of migration illustrated thus far is not limited to *D. discoideum* alone, with some leukocytes adopting a very similar form of motion [139]. The characteristic mix of weak cell-substrate interactions, strong polarisation, dynamic pseudopod protrusion and myosin aided uropod retraction is typically very fast with neutrophils and *D. discoideum* being observed to travel at speeds of around 20 μm/min and 10 μm/min, respectively [140, 141]. The mechanisms that modulate migration between these two cell types are somewhat conserved, with commonalities appearing in both Ras and PI3K signalling, as well as actin polymerisation utilising Arp2/3 via Rac-activated WASP proteins [142]. Prominent differences include the range of chemotaxis specific signalling molecules and receptors available for each cell type. Leukocytes must be versatile, adaptive and capable of communicating with many other aspects of the body, which is reflected in the range of chemokine receptors they express and corresponding chemokines they can bind [143]. In comparison, the independent *D. discoideum* has relatively few functions, and, as such, only binds a small range of signalling molecules to a similarly small selection of chemotaxis receptors [144]. This discrepancy has a direct correlation with the structural variety that can be expected of GPCRs between these two types of organism. For instance, *D. discoideum* receptors express only one $G\beta\gamma$ [145], whereas leukocyte receptors utilise a multitude of $G\beta$ and $G\gamma$ combinations [142], allowing for a more diverse and refined range of responses.

Alternative modes of migration to that of *D. discoideum* are those of amoeboid or mesenchymal migration. Mesenchymal migration is most commonly observed in mammalian cells - such as cancer cells - and is characterised by large actin rich protrusions, such as lamellipodia or filopodia, coupled with strong extracellular matrix interactions and degradation [146]. Proteolysis of the extracellular matrix allows the cell to mould its immediate environment in a manner advantageous to migration [147]. Amoeboid migration - similarly

observed in cancer cells - most notably utilises a heavily myosin enriched posterior to essentially squeeze the back of the cell, inducing bleb formation and propelling the cell forewards [148]. This style of motion does not require strong adhesion to the extracellular matrix and so does not depend the formation of focal adhesions [149]. Tumour cells have been observed to switch from mesenchymal to amoeboid style migration in situations where degradation of the cellular environment becomes compromised through, for example, introduction of protease inhibitors - compensating for the lack of matrix remodelling by adopting a form of migration that instead allows the cell to squeeze through pre-existing gaps [150]. This transition often results in an increase in cellular velocity [151]. It should be noted that, in truly counter intuitive fashion, it is apparent that the form of motion most often adopted by the amoeba *D. discoideum* is not actually a true representation of the definition of amoeboid migration. In fact, common *D. discoideum* migration is actually closer to mesenchymal than amoeboid, albeit without the extracellular matrix interactions and degradation. Amoeboid migration is only adopted by *D. discoideum* in environments that that are non-planar, such as when migrating under a stiff layer of agarose [152]. This makes sense as this type of environment more closely recapitulates the tissues through which cancer cells - moving in an amoeboid style fashion - would migrate.

The mechanisms of cellular migration presented thus far rely on a spatial resolution of extracellular gradients across the cell length, driving the cell in the direction that binds the most signalling molecules. Is it clear, however, that this method of detection will become decreasingly efficient as cell size decreases. It has been shown that *D. discoideum* can resolve and respond to a chemical gradient as long as there is at least a 1% difference in receptor occupancy across their length [153], but the smaller a cell is the the less likely it is that this minimum difference in receptor binding across their extrema can be achieved. It has been shown, from a mathematical perspective, that a cell the size of a bacterium could feasibly navigate by comparing receptor occupancy between its front and back, however, a serious issue arises in that the motion of the cell largely alters the flux of molecules onto the cell surface - and subsequent receptor binding dynamics - in comparison to a stationary state [154]. This means that the gradient perceived by a moving cell - of size in the order of a bacterium - differs substantially from the true external gradient, implying that sensible decision making relative to that gradient will be similarly impaired. When one considers these smallest of cells, a spatial sensing mechanism is simply no longer viable; instead, a temporal method for sensing gradients is relied upon [155]. Fundamentally, this method is built upon a system of continuous autophosphorylation, the outcome of which is to randomise the direction of swimming [156]. When this occurs the cell is said to tumble. In favourable conditions, the rate of autophosphorylation decreases - meaning that tumbling occurs less frequently - and in unfavourable conditions the rate of autophosphorylation increases - increasing the frequency of tumbling [157]. The overall implication is that bacteria will travel for longer in the same direction when conditions are improving, and less when conditions are worsening, the net effect of which is that bacteria become biased in the directional of environmentally favourable

conditions [158]. Favourable conditions can mean either more attractant or less repellent, the definition of which varies among different bacterial species. These types of stimuli include: temperature, osmolarity, pH, oxygen levels and the intensity and wavelength of light [159]. Focusing on the very thoroughly researched *E. coli*, swimming occurs when all flagella are rotating anti-clockwise, and a tumble can occur when only one flagellum rotates clockwise instead [160]. A new swimming direction is chosen when all flagella once again rotate anticlockwise. Although the number and location of flagella can vary among different bacterial species, biased motion always relies chemosensory regulation of the motor action of the flagella [161]. The proteins which allow bacteria to sense their environment are transmembrane chemoreceptors called methyl-accpeting chemotaxis proteins (MCPs) and act in a similar manner to previously discussed receptors, binding extracellular signalling molecules and relaying the signal to modulate chemotaxis, albeit with a somewhat unique transduction pathway [162]. The number of MCPs encoded in the genomes of different bacterial species ranges drastically, with *Mezorhizobium loti* expressing 1, *E. coli* expressing 5 and *Magnetospirillum magnetotacticum* expressing 60 [163]. This essentially corresponds to the different stimuli that each bacterium has evolved to respond to, and gives insight into both the environmental niche that the bacterium occupies as well as individual functionality [164]. While MCPs have poorly conserved ligand binding domains - corresponding to the variation in types of signal molecule that can bind - the cytoplasmic domains are highly conserved, essentially consisting of an autophosphorylating kinase, chemotaxis protein A (CheA), which is linked to the MPC with an adapter protein, CheW [165]. Binding of signal molecules alters the rate of autophosphorylation - and activity - of CheA, which, in turn, acts to phosphorylate two further proteins, CheY and CheB [166]. Active CheY binds to the protein Flim - located on the flagellum motor - and reverses the direction of motion, likely inducing a tumble [167]. This means that high CheY activity translates directly into a high tumble frequency for the bacterium, and vice versa. CheB, a methylesterase, acts to demethylate MCPs, of which the methylation state affects the change in the rate of CheA autophosphorylation for a given stimulus concentration [168]. A lowering of MCP methylation states reduces CheA autophosphorylation, meaning that the bacterium will be less likely to tumble. Similarly, higher MCP methylation states increase CheA autophosphorylation, meaning that the bacterium is more likely to tumble [169]. In the absence of any other proteins MCPs would just become increasingly demethylated - and less likely to tumble - due to CheB activity, so a constitutively active methyltransferase, CheR, exists to balance this effect, causing a continuous increase in the methylation state of MCPs [170]. So, combining all this information, attractant binding to MCPs causes a decrease in CheA autophosphorylation, decreasing the rate of phosphorylation of CheY and CheB. This both reduces the tumbling frequency and decreases the rate of CheB demethylation - meaning CheR causes a bigger increase in methylation than the decrease from CheB - causing a net increase in MCP methylation [171]. This means that the bacterium will adopt a directional bias towards the source of the attractant - due to less tumbling - but this effect will reduce as MCP methylation states increase, and CheA autophosphorylation increases to pre-stimulus levels - at which point there will

be no longer be a directional bias [172]. Similarly, repellent binding will cause an increase in CheA autophosphorylation, increasing the rate of CheY and CheB phosphorylation. This both increases tumbling frequency and increases the rate of CheB demethylation - meaning CheR causes a smaller increase in methylation than the decrease from CheB - causing a net decrease in MCP methylation [173]. The overall effect is that the bacterium travels away from the repellent - due to more tumbling - but this effect reduces as MCP methylation states decrease, and the rate of CheA autophosphorylation drops back to pre-stimulus levels [174]. Essentially, the CheY signalling pathway corresponds to the stimulation induced response of the bacterium, and the CheB pathway represents the adaptation of the bacterium to new environments - allowing for continuous re-evaluation of what constitutes attractive and repellent signals, and overall more effective chemotaxis [175]. The phosphorylation of CheY occurs much faster than methylation by CheR or demethylation by CheB, ensuring that the bacterium has the chance to respond to a new stimulus before adapting [176].

1.4 Dictyostelium discoideum

Mentioned a few times already, *D. discoideum* are a useful tool for chemotaxis assays due to their resilience, highly chemotactic nature and ease of culture and genetic modification [177]. On top on this, different derivatives of cAMP have been synthesised with a wide range of properties, allowing for versatile chemotaxis assays [178]. As such, *D. discoideum* shall be the organism utilised in this thesis for testing the chemotactic dynamics of novel, complex environmental conditions. A common preconception is that any conclusions drawn from studies on *D. discoideum* do not translate into the medically significant field of mammalian cell biology. Relative to chemotaxis, however, the underlying biological machinery is highly conserved among eukaryotes, meaning that deductions drawn from *D. discoideum* have a high level of significance relative to other mammalian cell types of greater established import [179].

1.4.1 Dictyostelium Life Cycle

The soil dwelling amoeba *D. discoideum* is a social eukaryote that relies on chemotaxis in order to find nourishment and attract other *D. discoideum* [180]. Its life consists of three distinct cycles: vegetative, social and sexual. While food is plentiful *D. discoideum* will occupy the vegetative cycle and once they begin to starve they will enter either the social or sexual cycle [181]. In the vegetative cycle *D. discoideum* will prey upon bacteria in the soil, ingesting them and periodically dividing [182]. To be more specific, folic acid secreted by bacteria is deteced by the fAR1 receptor - acting as a chemoattractant and guiding the cell to the bacteria so it can be ingested by phagocytosis [183]. Once food becomes scarce the most common behavioural shift is to that of the social cycle, where neighbouring cells begin secreting cAMP - attracting each other and aggregating into a large, multicellular slug [184]. This slug then undergoes several stages of differentiation, ultimately forming a fruiting body [185]. This body then releases spores which lie dormant until food is once

again present, at which point the spores germinate and young cells emerge to begin the vegetative cycle anew [186]. A much rarer form of reproduction, the sexual cycle occurs when two *D. discoideum* of different mating types - of which there are three - fuse and begin cannibalising surrounding cells, upon aggregation via local cAMP secretion [187]. Some of the outer prey cells form a cellulose wall before being consumed, resulting in a diploid macrocyst [188]. The giant, enclosed cell then undergoes meiosis and further mitosis to produce many recombinant, haploid amoeba which hatch to feed as in the vegetative cycle [189]. As such, chemotaxis forms a basis for both nourishment and reproduction in *D. discoideum*. This means that a chemotaxis defect, say through lack of glycogen synthase kinase-3 [190], is catastrophic for both present and future generations of *D. discoideum*.

1.4.2 Investigating Chemotaxis

In order to perform a truly thorough study on chemotaxis, it will be necessary to utilise a mixture of chemotactic factors with different properties. If a model of biased migration can be used to comprehend increasingly complex environmental conditions, and predict the outcome of further intricacies, then it can be said with certainty that the mechanisms of the model are very good descriptors of chemotaxis. The main variations in chemoattractant function that shall be considered in this thesis are the level of response elicited upon receptor binding, the extremes being a full agonist or antagonist, and the level of cell induced ligand breakdown that occurs [191, 192]. Additionally, it is important to gauge the approximate level of receptor affinity for any considered chemicals, as this allows one to relate extracellular signal to the proportion of receptor binding on the cell surface, and avoid undesirable effects such as receptor saturation [193]. The primary cell-surface receptor that shall be focused on, as it has been shown to be the primary mediator of biased migration to cAMP, is the cAR1 receptor [194]. For *D. discoideum*, extracellular cAMP is a very strong chemoattractant that is broken down by secreted phosphodiesterases and has a dissociation constant - the concentration at which the number of receptors bound is half maximal - in the order of a few nM, relative to the cAR1 receptor [195, 196]. Two analogues of cAMP, Sp-cAMPS and Rp-cAMPS, have been synthesised to be phosphodiesterase resistant and have dissociation constants, relative again to the cAR1 receptor, approximately two orders greater than that of cAMP [197, 196]. Whereas Sp-cAMPS provides an agonistic role for cAR1, Rp-cAMPS has been shown to block the conformational change that relays external cAMP signals to various intracellular pathways [198]. It has, however, also been shown to elicit a chemotactic response at very high concentrations [197], perhaps instead suggesting a partially agonistic nature. Many other artificial derivatives of cAMP also exist with a diverse range of properties [199].

When performing chemotaxis assays with *D. discoideum* it is necessary to starve them for a few hours to forcibly induce the social cycle. The cells express more cAR1 receptors as they starve, making them increasingly sensitive to extracellular cAMP, peaking at around 3-4 hours into starvation [200]. Simultaneously, they begin secreting cAMP every 6-8 min-

utes, causing neighbouring *D. discoideum* to aggregate [201]. While the sensitivity to cAMP makes for very motile cells, perfect for chemotaxis assays, the periodic cAMP secretion has the potential to interfere hugely with any externally imposed gradients due to the very small cAR1 dissociation constant for cAMP [202]. In order to proceed it is necessary to eliminate the unwanted receptor binding and activation mediated by cAMP secretion; conveniently, however, this can be achieved simply by using caffeine, which blocks cAMP dependent activation of adenylyl cyclase [203]. The final element required in order to perform complex chemotaxis experiments is selection of a suitable assay. The study of chemotaxis has evolved over the years, and this is reflected in the wide assortment of experimental methods that have been developed with time [204]. One popular technique is the under-agarose assay, which involves cells crawling under a layer of agarose toward a source of chemoattractant [205]. As cells here are in contact with more than one surface, this particular method is useful for simulating migration in more 3D environments, such as amoeba moving through soil [206]. Additionally, the rigidity of the agarose can be varied, allowing investigation of cell migration relative to a range of restrictive environments [207]. Another prominent method is the micro-pipette assay, in which a small plate of cells is exposed to a chemical stimulus via continual injection from a micro-pipette tip [208]. This particular situation is useful for simulating a scenario where a distribution of cells responds to a continually secreting point source of chemoattractant [209]. Microfluidic chambers are capable of generating complex, stable and well defined gradients for a more precise study on chemotaxis [210]. This is achieved via an intricate network of microchannels each containing a flow of chemoattractant at variable concentration which, when oriented in parallel, create an easily modulated chemical gradient perpendicular to the flow of the microchannels [211]. Another type of device that allows for easy control over gradient properties are bridge chambers, where two wells - of variable attractant concentration - are separated by a bridge. As long as the concentration of one well is higher than the other, molecules of attractant will diffuse from the well of high concentration to low, tending to a controllable linear equilibrium across the bridge [212]. A cover slip with cells is inverted over the bridge, where the cellular response to the gradient can be imaged using a time-lapse microscope [213]. Various generations of bridge chamber have been developed over time, the first being the Zigmond chamber in 1977 [214]. This chamber provided great improvements for chemotactic investigation, with better optical properties allowing for easier imaging and the production of a stable linear gradient permitting intuitive correlation between chemical concentration, space and cell response. Unfortunately, however, the mechanism by which the cover slip was held in place was somewhat unpredictable, leading to a variable gap between the cover slip and bridge, and unforeseen variations in the chemical gradient [215]. Another design arose in 1991 with the Dunn chamber, which replaced parallel wells with concentric annuli [216]. This chamber provided a stable gradient for a much longer period of time, allowing for easier investigation of much slower cell types - like cancer cells - but lead to data that was much harder to quantify due to the curved viewing platform [217]. An improvement on the Dunn chamber design, the current epitome in bridge chemotaxis chambers, the Insall chamber, was published in 2010 [218]. This

chamber provides the stable, long lasting, gradients elicited by the Dunn chamber but uses a rectangular design instead. This not only permits much easier quantification but also allows for the incorporation of different bridge widths, meaning that gradients of varying steepness can be simultaneously imaged and analysed.

1.4.3 Self-Generated Gradients

A common assumption in studies on chemotaxis is that the chemical gradients to which cells respond are linear. This is quite reasonable as diffusion - the natural process by which molecules drift from areas of high concentration to low concentration - in 1D, such as in a chemotaxis chamber, tends to a linear equilibrium (see equation 12). However, in cases where a cell has the ability to enzymatically degrade a molecule, then this breakdown competes against diffusion and gives rise to steeper, non linear, localised chemical gradients that move with the cell [219]. Comparing this with a linear gradient, where receptor binding is dependent only on the cellular location in the gradient, a cell that can self-generate its own gradient has the potential to migrate faster and further [220]. This ability to essentially mould extracellular signals allows cells to chemotax skillfully in complex situations, such as a maze, that would prove impossible to navigate in the absence of enzymatic breakdown [221]. Self-generated gradients can allow cells to chemotax under other conditions that would also prove impossible without degradation, for instance a large distance containing a uniform concentration of chemoattractant [222]. Specifically, *D. discoideum* exposed to a $5mm$ uniform concentration of folate can self-generate localised gradients, allowing them to resolve a difference in receptor occupancy across their length and migrate effectively, via secreted and cell-surface folate deaminase which acts to degrade the folate [223]. The resultant chemotaxis is so robust that the cells can traverse the entire $5mm$ distance, a feat that would be impossible - even if the gradient were linear - without enzymatic degradation. Self-generated gradient mechanics have also been observed relative to melanoma cells and lysophosphatidic acid [224], an agonist present across malignant tumours. By degrading levels of lysophosphatidic acid in the tumour, melanoma cells could self-generate a chemotactic gradient that drives the cells into surrounding tissues, suggesting a mechanism by which cancer cells can spread and form metastases [225]. It is clear that enzymatic breakdown, and the ability of cells to essentially modulate their own migration, is of profound significance in the field of chemotaxis.

1.5 Mathematical Tools

Based on the information presented thus far, the crucial quantity to track if one wants to understand chemotactic response is receptor activation, as this is the medium through which a cell both senses and responds its environment. Understanding how a human interacts with the world and moves through space would be nonsensical without first comprehending the function of the eyes, nose and ears. As discussed previously, the cellular equivalent of this sensory apparatus are GPCRs. These bind extracellular signalling molecules, inducing a

conformational change and activating signalling pathways that dictate how the cell responds [226]. The implication here is that comprehension of the intricacies of chemotaxis primarily requires quantitative details on receptor activation, rather than chemical concentration. Concentration, however, is still a vital quantity to track as receptor activation requires the presence of signalling molecules, and it is the quantity that can be modulated directly in a chemotaxis assay [227]. Tracking the changing relationship between concentration and subsequent cellular receptor activation for multiple cells in a chemical gradient - in real time using wet lab techniques - however, comes with a fair share of complications [228]. If mathematics could instead be employed to supply the interface between these quantities, then this could provide a simpler and more intuitive system by which chemical concentration can be related to cellular response - perhaps allowing for relatively easy analysis of more complex chemical arrangements.

1.5.1 Relating Concentration to Receptor Activation

The first step to this interface is to be able to relate a number of chemical concentrations, allowing for arbitrary chemical environments to be considered, to a corresponding level of receptor binding [229]. To begin, consider unbound receptors, U, binding to specific ligands, C_i, to form bound receptors, G_i, where $i \in [1, n]$. Mathematically this can be represented as

$$U + C_i \underset{k_{-i}}{\overset{k_i}{\rightleftarrows}} G_i, \tag{1}$$

where k_i, k_{-i} represent the rates of association and dissociation for each ligand. Further insight can be deduced via the law of mass action, which states that the rate of change of a reaction is proportional to the product of the concentrations of the reactants [230]. This means that

$$\frac{\partial U}{\partial t} = -k_i U C_i + k_{-i} G_i, \tag{2}$$

where further equations can be similarly deduced for the rates of change of C_i and G_i. An equilibrium state shall now be assumed where receptors and ligands are binding as quickly as the corresponding complexes are dissociating. This means that $\frac{\partial U}{\partial t} = 0$, or the number of free receptors remains independent in time, as receptors are being bound as quickly as they are being freed. This is a very common type of assumption that, while rarely justified, tends to provide accurate models while simultaneously causing associated mathematics to simplify, increasing practicality [231]. In a non-equilibrium system it can be said that the rates of association and dissociation will cause a deviation from any steady state deductions [232]. This assumption shall not, however, be regarded as completely acceptable for this situation until such a time as the validity of the model can be experimentally verified. In the meantime, substituting this into equation (2) and rearranging gives

$$\frac{U C_i}{G_i} = \frac{k_{-i}}{k_i} = K_{di}, \tag{3}$$

where K_{di} is the dissociation constant for ligand i, the concentration at which half of the receptors are bound by ligand i. This can be seen by setting $C_i = K_{di}$, such that the concentration of free ligand is at the dissociation constant, which, upon substitution into equation (3), gives $U = G_i$. This means that the number of free receptors is equal to the number of bound receptors, or half of all receptors are bound, as expected.

It is now important to lay down a convention for characterising the level of receptor activation of a given ligand. This is to account for ligands of different agonistic properties, and the concept that some ligands vary in their probability of inducing a conformational change upon receptor binding [233]. For any given ligand, the fraction of receptors which become active upon binding is known as the intrinsic efficacy [234]. This quantity shall be represnted as α, where $\alpha \in [0, 1]$. A full agonist would have $\alpha = 1$, such that all - previously inactive - receptors bound become active and induce intracellular signalling events. A competitive antagonist would have $\alpha = 0$, such that no conformational change ever occurs upon receptor binding. The behavioural impact of a partial agonist can then be represented as any $\alpha \in (0, 1)$, where, for example, an intrinsic efficacy of $\alpha = 0.5$ would correspond to half of all - previously inactive - receptors bound becoming active. Note that an inverse agonist, upon binding to constitutively active receptors would instead occupy the range $\alpha \in [-1, 0)$, defining the proportion of previously active receptors which become inactive. However, as the re-association of the α and $\beta\gamma$ subunits occurs as a result of ligand independent GTP hydrolysis, it shall be assumed that ligand binding does not catalyse a backwards reaction [235]. In other words, deactivation of receptors - induced by inverse agonists - shall be disregarded for the purposes of this thesis. Furthermore, it is entirely unclear if it is realistic to even consider constitutively active receptors relative to *D. discoideum* [236]. For now, as it makes the mathematical framework simpler and more intuitive, it shall be assumed that all unbound receptors are in an inactive state - either remaining inactive or becoming active upon ligand binding. Constitutive receptor activity shall not, however, be entirely discounted until proof to the contrary is obtained.

It is now possible to derive a quantity which represents the fractional amount of active receptors, Ω, occurring relative to n concentrations of different ligand. This can be done simply by taking the number of bound receptors - including ligand intrinsic efficacy - as a fraction of the total number of receptors, both free and bound. This gives

$$\Omega = \frac{\sum_{i=1}^{n} \alpha_i G_i}{U + \sum_{i=1}^{n} G_i}, \tag{4}$$

where by substituting G_i from equation (3) it can be seen that

$$\Omega(C) = \frac{\sum_{i=1}^{n} \frac{\alpha_i C_i}{K_{di}}}{1 + \sum_{i=1}^{n} \frac{C_i}{K_{di}}}. \tag{5}$$

So, if $\Omega = 0.7$, then a combination of ligands - of any arbitrary concentration - are present which result in 70% of receptors being active.

1.5.2 Gradient Shapes

Translating a combination of chemical concentrations into an approximate, proportional number of active receptors essentially signifies understanding of receptor activation at a single point in space. In a more realistic chemical system, a cell will usually be immersed in a multitude of chemical gradients, for which chemical concentration will change with space. So, naturally, in order to expand our understanding of receptor activation to include spatial variation, it is crucial to derive functional forms expressing how chemical concentration evolves with space. The two primary processes that dictate this evolution are molecular diffusion and cellular enzymatic degradation [220]. In general, a chemical system will involve some combination of these processes, depending on the nature and concentration profiles of the ligands at play. The system will evolve in both space and time, but generally tend towards an equilibrium state, at which point the system's time dependency becomes immaterial, and only spatial variation is significant. From a mathematical perspective, a full analytical solution incorporating both spatial and temporal evolution is rather impractical to use and will likely hamper progress. Much more elegant and insightful is to consider only the steady state solution, meaning that temporal dependency at small times will not be considered. This must be taken into account when interfacing the math with the biology, such that measurements must be ignored until such a time that an equilibrium state has become apparent.

The first equilibrium gradient topology to be considered is that relative to diffusion - the natural shifting of molecules from a region of high concentration to that of low concentration - only. This process will occur in isolation for the case where the molecule in question is not enzymatically degradable. The governing mathematical relation for a system such as this is the diffusion - or heat - equation [237],

$$\frac{\partial C}{\partial t} = D\nabla^2 C, \tag{6}$$

where the rate of change in concentration, C, with respect to time, t, is equal to the product of the Laplacian, ∇^2, of the concentration and the diffusion coefficient, D. The Laplacian of the concentration can be interpreted as the rate of change of the concentration gradient, the steepness of which affects the rate at which molecules will pass a given area, according to Fick's Law [238]. The diffusion coefficient contains information about flow speed. It is thus intuitive that the combination of these two variables is informative of how the distribution of molecules, and so the concentration, changes with time. The Laplacian can be represented as

$$\nabla^2 = \frac{\partial^2}{\partial x^2} + \frac{\partial^2}{\partial y^2} + \frac{\partial^2}{\partial z^2}, \tag{7}$$

illustrating that it encompasses gradient flow in 3 dimensions. For many cases there is an immediate and substantial simplification that can be made, due to the fact that molecules are only flowing in one direction, from the source of highest concentration, in a straight line, to the region of low. If this direction is called x, then it can be said that there is no flow in the y and z directions. Hence the last two terms on the right hand side (RHS) of the Laplacian can be set to zero. This simplification keeps the maths concise and elegant, while still being very much biologically relevant, and gives the 1D diffusion equation,

$$\frac{\partial C}{\partial t} = D\frac{\partial^2 C}{\partial x^2}. \tag{8}$$

As early temporal changes are being disregarded in favour of focusing solely on the equilibrium state, the left hand side (LHS) of equation (8) can be set to zero, giving

$$\frac{\partial^2 C}{\partial x^2} = 0. \tag{9}$$

This can be solved simply by integrating twice with respect to x, giving

$$C(x) = Ax + B \tag{10}$$

for some constants of integration A and B. In order to deduce these constants the equation must be constrained to the problem at hand. This is achieved via the application of boundary conditions (BCs), which correspond to the concentrations of the source and sink. To keep things as general as possible, it shall be assumed that the concentration of the sink, C_0, located at $x = 0$, is non-zero. The concentration of the source, C_1, is located at $x = L$. These conditions can be summarised as

$$C(0,t) = C_0 \quad and \quad C(L,t) = C_1. \tag{11}$$

The inclusion of the t represents the fact that these concentrations hold for all times, as it is the steady state being being considered. Naturally, the chemical gradient encompasses the area $x \in [0, L]$. Applying the BCs gives a mathematical form for the equilibrium state,

$$C(x) = \left(\frac{C_1 - C_0}{L}\right) x + C_0, \tag{12}$$

which, as expected, is independent of time and allows concentration at any x to be calculated. This steady state form is, intuitively, linear.

Enzymatic breakdown, as has been discussed already, has huge implications for gradient shape. Cellular degradation creates steep, localised gradients, that lead to an overall sharper gradient profile. In the presence of cellular degradation, the diffusion equation is modified by the inclusion of a degradation term that illustrates the deduction of molecules via cellular enzymes. A commonly used mathematical model when considering enzymatic reactions is

that of Michaelis-Menten kinetics [239], which gives changes in mass, M_C, of a substance with concentration C, with time, such that

$$\frac{\partial M_C}{\partial t} = \frac{V_{max} C}{C + K_m}, \tag{13}$$

where V_{max} is the maximum rate of degradation, occurring at saturating concentrations, and K_m is the Michaelis-Menten constant, the concentration at which the rate of degradation is half its maximal value. The maximum rate of degradation, V_{max}, can be relative to any desired biological or mathematical feature - most intuitively that of an enzyme molecule or a cell. The rate of degradation, $\frac{\partial M_C}{\partial t}$, will then be relative to the specified feature. In order to combine the mathematics of diffusion and degradation, to attain how concentration changes with space and time due to these mechanisms, it is then required to translate rate of change of mass,$\frac{\partial M_C}{\partial t}$, into a rate of change of concentration. This can be easily found by multiplying equation (13), which is in terms of the rate per feature (enzyme or cell), by the number of features per unit volume. This will give the change in mass, per unit volume, with time, $\frac{\partial C}{\partial t}$. In doing this, V_{max} will also become relative to a volume rather than a feature. It is worth noting that all subsequent analysis will have V_{max} in terms of a volume, and that this is an unconventional representation. Similarly to the previous conversion, it is simple enough to convert V_{max} back into a feature specific quantity by dividing this by the number of features per unit volume. Changes in concentration over the bridge will now be governed by both diffusion and degradation in a reaction-diffusion equation of the form

$$\frac{\partial C}{\partial t} = D\frac{\partial^2 C}{\partial x^2} - \frac{V_{max} C}{C + K_m}, \tag{14}$$

where the simple case of a 1D flow, in the x direction, has once again been assumed. Note that the Michaelis-Menten term is negative, illustrating that molecules of ligand are being deducted due to degradation. It should be noted that the degradation term in equation (14) acts upon each and every infinitesimally spaced element in the 1D chemical gradient. An analogy to this could be that the cells are packed together as tightly as they could possibly get, resulting in a continuum degradation effect. In reality cells act in a discrete fashion, hence some kind of conversion between the continuum and discrete regimes must be found to in order to gain useful insight, using analytical math, from experimental data. In contrast, this would not be required for diffusion as it acts in a naturally continuous manner. Solving equation (14) in full, relative to some appropriate boundary conditions, is taxing. Instead, two limiting cases shall be considered. The first of these is a low concentration limit, $C << K_m$, causing equation (14) to reduce to

$$\frac{\partial C}{\partial t} = D\frac{\partial^2 C}{\partial x^2} - rC \tag{15}$$

where

$$r = \frac{V_{max}}{K_m}, \tag{16}$$

which implies that degradation will be proportional to concentration. It is clear that as $C \to 0$, degradation effects will similarly disappear. This prediction matches that of full Michaelis-Menten kinetics as illustrated in equation (13). Conversely, as $C \to \infty$, the rate of degradation also increases infinitely, which contradicts the saturation effects of equation (13). It is thus very important that concentration is kept in the stated limit, otherwise the system will no longer obey the laws of Michaelis-Menten and become unrealistic. Once again, only the equilibrium state is of interest, at which point $\frac{\partial C}{\partial t} = 0$ such that

$$D\frac{\partial^2 C}{\partial x^2} - rC = 0. \tag{17}$$

It is worth noting that this steady state represents the point at which degradation effects exactly balance diffusion, causing no further temporal change in the system. The general solution to equation (17) is

$$C(x) = Ae^{-Rx} + Be^{Rx} \tag{18}$$

for some constants A and B, where

$$R = \sqrt{\frac{r}{D}}. \tag{19}$$

Once again, these constants are specific to the spatial constraints of the problem at hand and can be found by imposing boundary conditions. The boundary conditions will be fixed, as in conditions (11), illustrating the assumption that the volumes of the source and sink are large enough that degradation effects give negligible changes in concentration, or that cells are not present in the source and sink. This is convenient from an analytical perspective, and will simplify the math without sacrificing insight. For simplicity, it shall be assumed that the sink, located at $x = 0$, is fixed at zero concentration, and the source, located at $x = L$, is fixed at concentration C_1. This gives the boundary conditions

$$C(0,t) = 0 \quad and \quad C(L,t) = C_1, \tag{20}$$

which, when applied to equation (18), gives the steady state function

$$C(x) = \frac{C_1(e^{Rx} - e^{-Rx})}{e^{RL} - e^{-RL}}. \tag{21}$$

Note that this equilibrium state is exponential. The second limiting case is a high concentration approximation, $C >> K_m$, causing equation (14) to reduce to

$$\frac{\partial C}{\partial t} = D\frac{\partial^2 C}{\partial x^2} - V_{max}, \tag{22}$$

which implies that cells are degrading at their maximal rate always. It is clear that as $C \to \infty$, there is no subsequent impact on degradation effects as they are now constant. This prediction matches the saturation effects of full Michaelis-Menten kinetics from equation (13). However, if $C \to 0$, the rate of degradation remains similarly invariant, which, at low enough concentrations, could cause concentration to become negative. This is in

clear violation of Michaelis-Menten kinetics and shows, once again, how important it is that concentration is kept within the aforementioned limit. In the equilibrium state the LHS of equation (22) will be set to zero, as usual, giving

$$D\frac{\partial^2 C}{\partial x^2} - V_{max} = 0, \tag{23}$$

which can be solved by integrating twice with respect to x. This gives rise to the relation

$$C(x) = Qx^2 + Ax + B, \tag{24}$$

where Q is defined as

$$Q = \frac{V_{max}}{2D}, \tag{25}$$

and constants A and B can be found by applying the same boundary conditions (20). This gives a final, steady state form of

$$C(x) = Qx^2 + \frac{x}{L}(C_1 - QL^2), \tag{26}$$

which is a quadratic.

2 Methods

In general, the methodology of this thesis follows a simple and consistent pattern. Mathematics, both analytical and numerical, is implemented to deduce chemical conditions that may lead to migration behaviours of interest. Bridge chamber assays are then used to test these conditions, both verifying the mathematical model and giving insight into system parameters. Once the mathematics accurately recapitulates experimental outputs for a given chemical configuration, further chemotactic complexities are then probed using mathematics and verified via the same bridge chamber assay. All coding is done in Java and all graphing in gnuplot.

2.1 Bridge Assays

The bridge chamber assays are always performed the same, using the 1mm bridge of an Insall chamber and wild-type NC4 *D. discoideum*. The same buffer is used for each aspect of this assay and contains a mixture of two potassium phosphates - KH_2PO_4 and K_2HPO_4 - at pH 6.2, with a working concentration of 5mM. If the cells are to be left in suspension for an elongated period of time, then a mixture of $MgCl_2$ and $CaCl_2$ is also added to the buffer, with working concentrations of 2mM and 1mM respectively. The phosphate buffer shall now be referred to as KK_2, and as KK_2MC with the addition of magnesium and calcium chloride. The bacteria used for the *D. discoideum* to feed upon and grow are *Klebsiella aerogenes*, which are passaged weekly by streaking an agar plate with the bacteria and - after being allowed to grow on an agar plate for two days at 22°C - are kept at 4°C. The *D. discoideum* are also passaged weekly by placing an inoculation loop onto an agar plate that has been spread with a mixture of KK_2 and *K. aerogenes*; they are then kept at 22°C to feed and proliferate. When passaging *D. discoideum* or preparing clearing plates for an experiment, inoculation loops are always taken from the feeding front - to guarantee that *D. discoideum* in the vegetative stage are harvested. The protocol for the experiment is now as follows:

1. Two days prior to the experiment, four 1.5ml tubes are prepared containing KK_2 mixed with an inoculation loop of *K. aerogenes*. An inoculation loop of *D. discoideum* is then taken and mixed into one tube, and a dilution series made with the three remaining tubes. Suspension is then pipetted from each tube onto four separate agar plates, spread, and left to dry before being placed into an incubator at 22°C.

2. On the day of the experiment, *D. discoideum* are harvested from the plate which shows the most clear patches - to guarantee many bacteria have been consumed, giving a high cell count - but with minimal signs of a shift into the social cycle. This usually manifests in distinct patterns on the agar plate as the *D. discoideum* begin to aggregate or, in cases of more extreme starvation, the formation of multicellular slugs or even fruiting bodies. It is important that as many harvested cells as possible are still in the vegetative stage so that they develop in a simultaneous and controlled manner, meaning that they become optimally sen-

sitive to cAMP - and perfect for chemotaxis assays - at the same time. Cells harvested from regions clearly of the social cycle have at least already began the transition to becoming more sensitive to cAMP, meaning that upon imaging the chamber these cells are at a later stage of development and will likely behave differently. Cells are harvested by adding 5ml KK_2 to the appropriate agar plate, scraping the bacteria and cells and then pipetting into a 50ml tube.

3. KK_2 is then added so the suspension contains 20ml fluid. The cells are then washed three times at 1300rpm for 3 minutes, re-suspending in 20ml KK_2. After the final wash the cells are suspended in 20ml KK_2MC. After well mixing the suspension, it is diluted by a factor 10 into 30ml KK_2MC and then well mixed once again (vortex and invert the tube a few times). Now do repeated cell counts, either diluting or adding more cells until the suspension has approximately 3x10^6 cells ml^{-1}.

4. Simultaneously with the previous step, mix KK_2 with 1% agar in a small beaker, keeping in mind that each repeat of the experiment requires 4ml of this mixture. So, if 4 repeats are desired, then 16ml KK2 with 1% agar is required, but, taking into account evaporation, 20ml should be made just to be safe. Microwave this mixture for about 20s and then in bursts of about 6s, until the agar has dissolved. While the mixture is hot and still liquid, add magnesium and calcium chloride to working concentration. Now distribute 4ml into however many 60mm diameter plates as constitutes the amount of repeats desired. Allow to set.

5. Once the agar has cooled and set, thoroughly mix the cell suspension and put the amount of fluid corresponding to 1.2x10^7 cells onto each plate. Gently distribute the suspension across the whole plate and allow to settle for about 30 minutes. Quickly tip each plate into a sink and then place them on their sides for 2 minutes before mopping up any excess fluid that has accumulated. Place the plates in an incubator at $22^{\circ}C$ for 2 hours.

6. Now place all plates apart from one into the fridge; the one plate left in the incubator will develop quickest and so will be the first set of cells to be tested in an Insall chamber. Take the plates of cells in the fridge out in increments so that the development of each plate is staggered, meaning that there will be cells at optimum levels of sensitivity to cAMP at different times - perfect for repeats. Taking the plates out in increments of 40 minutes approximately corresponds to development being staggered by about 20 minutes between each plate.

7. After 4 hours from the plates initially being placed in the incubator, start looking for signs of development in the very first plate. Also check the plate staggered next as sometimes development times can overlap. The cells are ready to be harvested when there are clearly visible centres of cell aggregation across the plate, but before the cells have started to stream. At this time the cells are harvested from a plate using 1ml KK_2, scraping and then pipetting into a 1.5ml tube. Now spin the cells at 1700rpm for 3 mins, aspirate the excess

fluid and re-suspend the cells in 1ml KK_2MC. Now, mix this thoroughly and then dilute the suspension by a factor 15 into another 1ml KK_2MC. Add caffeine to a working concentration of 2mM - to suppress further cAMP secretion. After mixing thoroughly once more, pipette 200μl suspension onto four 22mm^2 cover slips and allow the cells to settle for at least 20 minutes.

8. Prepare mixtures containing KK_2MC with caffeine at 2mM and the chemotactic factor(s) of interest at the highest and lowest desired concentrations in the gradient. Assuming gradients are to increase from the center well of the Insall chamber to the outer channels, first put the mixture containing the low concentration of chemotactic factor everywhere in the Insall chamber (if the gradients are to start from zero concentration then just put a combination of KK_2MC with caffeine everywhere). Make sure to fill all the channels and leave a little excess, such that you can see a little bump when viewing the chamber side on. Now tip the excess liquid from a slide into the sink and place it cell side down on the chamber, making sure to leave the tips of the outer channel exposed. Aspirate the fluid from the outer channel via the exposed tips and pipette in the mixture containing the high concentration of chemotactic factor(s). Briefly observe the bridge separating the inner well and the outer channel under a microscope, checking that the cells are healthy and at a good density. If the slide was shifted while assembling the chamber it is possible to kill the cells; if this has occurred then reattempt assembly of an Insall chamber using one of the spare slides.

9. In general, the chamber was then left for about 10 minutes for the gradients to equilibrate before filming the 1mm bridge using a Nikon timelapse microscope at 10 fold magnification; for around 20 minutes. This is sufficient time to obtain data on the directional bias at different point along the gradient at equilibrium. Frequently check the next plate to develop in the incubator to prepare cells for testing subsequent conditions, or repeating previous conditions.

2.2 Simulations and Data Analysis

Simulations were agent-based, with each cell moving according to differences in local chemical concentration. Chemical changes in space and time, due to diffusion, were calculated according to the heat equation, via the Dufort-Frankel finite difference method. Deductions in chemical concentration due to cellular enzymatic degradation, from grid points within each cellular circumference, were calculated according to the Michaelis-Menten kinetics via fourth order Runge-Kutta method. Receptor activation was calculated at each grid point as a function of the chemical concentrations located there, according to standard bimolecular equilibrium behaviour. A difference in receptor activation across each cell could then be calculated via the grid points encompassed by the circumference of the cell. The chemotactic bias for each cell was then determined as a circular average of the difference in receptor activation across the cell extrema. Each cell also performed a persistent biased random walk, with a consistent step distance between each iteration. As such, the overall bias of the cell

- at each step - was determined as a combination of the chemotactic bias and a persistent random step drawn from a wrapped normal distribution.

Data from live cell imaging was analysed using an ImageJ plugin written by L. Tweedy (illustrated in [222]), giving the positional data of cells at different time points. The plugin located cells as pixels that were above a threshold intensity relative to surrounding pixels, and mapped them between frames. This data was then processed and converted into an x-direction velocity and average position for each tracked cell, such that an average velocity and error on the velocity could be found for cells occupying a defined partition of the bridge. This is the data that was then plotted for every experimental velocity output.

3 The Active Receptor Gradient

Using the tools illustrated in section 1.5, it is now possible to derive a mathematical form expressing how the proportional number of active receptors evolves with space. Given that cellular directional bias follows the spatial increase of this proportion, this representation allows for a very intuitive and elegant way to predict chemotaxis. This is especially useful when dealing with a confusing array of chemical gradients with varying intrinsic efficacies, as it is now a relatively simple process to simplify the system into a single gradient that encapsulates the predicted cell response. This representation shall be referred to as the active receptor gradient, and will be used very frequently in subsequent investigation. As such, a full active receptor gradient analysis of a simple gradient will be provided as an example.

3.1 Active Receptor Analysis of a Linear Gradient

Consider first the most basic of 1D chemical gradients, with a linear profile (due to being enzymatically non-degradable). In order to derive a general form for the active receptor gradient it is necessary to insert the functional form of the chemical gradient into equation (5). This essentially converts from expressing the proportional number of active receptors in terms of concentration to in terms of space, which is exactly the definition of the active receptor gradient. For the case of a non-degradable chemical this means inserting equation (12) into equation (5), giving the general form

$$\Omega(x) = \frac{\frac{\alpha}{K_d}\left\{\left(\frac{C_1-C_0}{L}\right)x + C_0\right\}}{1+\frac{1}{K_d}\left\{\left(\frac{C_1-C_0}{L}\right)x + C_0\right\}}. \tag{27}$$

This expression can be simplified for ease of use by applying some scenario specific parameters. For this most simple of cases let the gradient start from concentration $C_0 = 0\mu M$ and have maximum intrinsic efficacy, such that $\alpha = 1$, giving

$$\Omega(x) = \frac{C_1 x}{K_d L + C_1 x}. \tag{28}$$

Now, by applying information on C_1, K_d and L, the active receptor gradient can be plotted. A comparison between a chemical gradient and its corresponding active receptor gradient has been provided in Figure 1.

As the active receptor gradient increases in the direction of increasing chemical concentration, the cell directional bias will be in this same direction. This is chemoattraction, as expected. A further - and very significant - insight can be gained from the active receptor gradient, which cannot from the standard chemical gradient. This insight is that of the strength of the directional bias and how it is expected to vary across the spatial domain being considered. The idea here is that the strength of the response is proportional to the absolute difference in the proportional number of active receptors across the cell length. It has been observed that a minimum of a 1% fractional difference is required to induce the weakest

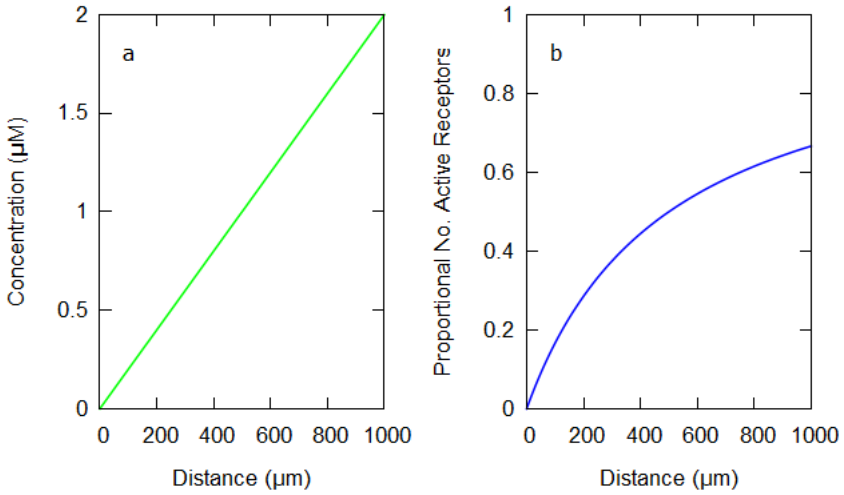

Figure 1: a) Linear concentration gradient and b) corresponding active receptor gradient for: $C_1 = 2\mu M$, $L = 1000\mu m$ and $K_d = 1\mu M$

chemotaxis [7], with the strength of the response increasing as this difference does. This behaviour will clearly saturate at some fractional difference for which the chemotactic response is maximal. Referring to Figure 1.b, it is obvious that changes in Ω are larger at the former part of the spatial domain than at the latter, meaning that directional cues should be stronger at the start of the gradient.

This concept can be be extended even further by accounting for the fact that cells have a finite width, W. This means there is a minimum rate of change in the active receptor gradient that must be required to induce chemotaxis, given that cells require a minimum difference in the fractional number of active receptors, $\Delta\Omega_{min} = 0.01$, across their length. This minimum change per unit length, δ_{min}, can be deduced trivially as

$$\delta_{min} = \frac{\Delta\Omega_{min}}{W}, \tag{29}$$

meaning, for cells which have a width $W = 10\mu m$, $\delta_{min} = 0.001\ \mu m^{-1}$. This implies there must be a change in the proportional number of active receptors of 0.1% per μm cell length. Given that the rate of change of the active receptor gradient with space is simply the derivative

$$\frac{\partial\Omega}{\partial x} = \delta, \tag{30}$$

it is possible to evaluate over what regions of the spatial domain a cell of width W would be expected to chemotax. Specifically, taking the ratio of δ and δ_{min} and plotting this for each spatial coordinate will give a kind of chemotactic map. On this plot, all values above one will imply that the cell is experiencing $\Delta\Omega > 0.01$ across it's length, and so chemotaxis can be expected. Conversely, values below one will imply that $\Delta\Omega < 0.01$ across the cell length and so no biased motion should occur. So, taking the derivative with respect to space

in equation (28) gives

$$\delta = \frac{K_d L C_1}{(K_d L + C_1 x)^2}. \tag{31}$$

It is now possible to plot the derivative of the active receptor gradient for some specific C_1, K_d and L. This quantity has been plotted for the same parameters given in Figure 1, alongside an evaluation of $\frac{\delta}{\delta_{min}}$, for a cell with specified W and $\Delta\Omega_{min}$, in Figure 2.

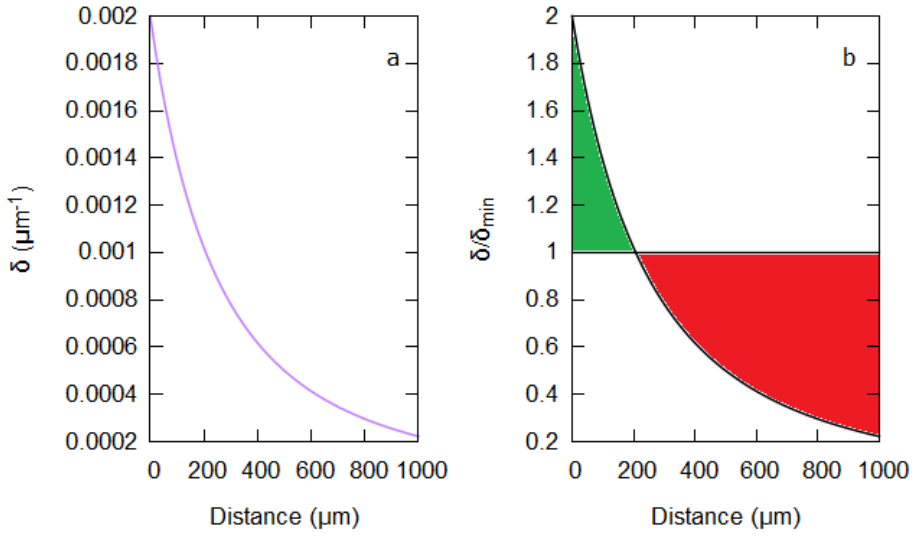

Figure 2: a) Derivative of active receptor gradient and b) $\frac{\delta}{\delta_{min}}$ with space when: $C_1 = 2\mu M$, $L = 1000\mu m$, $K_d = 1\mu M$, $W = 10\mu m$ and $\Delta\Omega_{min} = 0.01$.

The left hand graph in Figure 2 represents the rate of change of the active receptor fraction changes with space, and how this itself varies with space. It can be seen that there are larger changes in receptor binding - and activation - between the, relatively, smaller concentrations at the start of the gradient. If these same differences in concentration are considered further up the gradient, where overall concentrations are larger, it can be seen that changes in receptor binding are - relatively - reduced. This means that there will be larger differences in the number of active receptors across a cell length at the beginning of the gradient, and smaller differences at the end. This implies that directional cues will be stronger at the left hand side and tail off to the right, which confirms the same statement made via inspection of the active receptor gradient in Figure 1.b. Additionally, as all values of δ are positive, the directional bias will always be to the right. To re-iterate, this is because the fractional number of active receptors is increasing to the right. The green region in Figure 2.b represents areas where chemotaxis is predicted to occur, so $\Delta\Omega > \Delta\Omega_{min}$ across the cell, and the red region is where no biased cell motion is expected, so $\Delta\Omega < \Delta\Omega_{min}$ across the cell. Furthermore, the amount of deviation of $\frac{\delta}{\delta_{min}}$ from one corresponds to exactly how much more or less than $\Delta\Omega_{min}$ the cell is experiencing across it's length. In other words, stronger cell directional cues can be expected as $\frac{\delta}{\delta_{min}} \to \infty$.

3.2 The Strongest Directional Cues

A common preconception is that the strongest directional cues occur at K_d concentrations. However, given that K_d is located at $x = \frac{L}{2}$ for the chemical gradient considered in Figures 1 and 2, it is clear that the strongest cell directional cues do not occur at the dissociation constant. This is due to the fact that strongest directional cues will occur when $\frac{\partial \Omega}{\partial x}$ is at a maximum, such that differences in the proportional number of active receptors across a cell length are maximised. The largest value of $\frac{\partial \Omega}{\partial x}$ is clearly at $x = 0$, giving the strongest directional cues, and steadily decreases as $x \to L$. To further prove this, it is instructive to consider the second derivative of the active receptor fraction with respect to space. This can be obtained simply by taking the spatial derivative of equation (31), giving

$$\frac{\partial^2 \Omega}{\partial x^2} = \frac{-2K_d L {C_1}^2}{(K_d L + C_1 x)^3}. \tag{32}$$

If directional cues were strongest at K_d concentrations then $\frac{\partial \Omega}{\partial x}$ would increase with x until K_d was reached, and then begin to decrease. Interpreting this from the perspective of the next derivative, for x below K_d, the rate of change of $\frac{\partial \Omega}{\partial x}$ would decrease, until K_d, at which point it would begin to increase again. In other words there would be a turning point in $\frac{\partial \Omega}{\partial x}$, located at the point in x for which $\frac{\partial^2 \Omega}{\partial x^2} = 0$. Putting equation (32) to zero in this way gives

$$-2K_d L {C_1}^2 = 0, \tag{33}$$

meaning that that there is no turning point in $\frac{\partial \Omega}{\partial x}$ and it will either monotonically increase or decrease. Once again, this is obvious when one considers Figure 2.a, but is yet more proof that cell directional cues are not strongest at K_d concentrations. So, what role does K_d play? Instead, try maximising $\frac{\partial \Omega}{\partial x}$ with respect to controllable parameters, in this case the only one being the imposed end concentration of the attractant gradient, C_1. So, taking the derivative of equation (31) with respect to C_1 gives

$$\frac{\partial \delta}{\partial C_1} = \frac{K_d L(K_d L - C_1 x)}{(K_d L + C_1 x)^2}, \tag{34}$$

where a maximum in $\frac{\partial \Omega}{\partial x}$, relative to C_1, will occur when equation (34) is equal to zero, giving

$$\frac{\partial \delta}{\partial C_1} = 0 \quad \iff \quad C_1 = \frac{K_d L}{x}. \tag{35}$$

Using relation (35), it is now possible to deduce what final gradient concentrations, C_1, will give maximal directional cues for a given x-coordinate. It is important to realise that this is simply maximising directional cues at a given point, and not stating where overall directional cues are maximal. For example, if the dissociation constant is $K_d = 1\mu M$ then directional cues at $x = \frac{L}{2}$ are maximised when $C_1 = 2\mu M$. Given that the concentration at $x = \frac{L}{2}$ is K_d, it is clear that maximal directional cues for a given spatial coordinate are achieved when K_d concentration is located there, but, again, this does not means that the overall strongest

response in the spatial domain is similarly located there. The reason why this maximisation works is because final concentrations above and below the critical value value will give a reduced $\frac{\partial \Omega}{\partial x}$ for the given x-coordinate, meaning that it is a true turning point.

An additional point of interest is that of the trade off in the strength of the cellular response in different regions, relative to different chemical gradients. To illustrate this, Figure 3 shows two chemical gradients portrayed in terms of concentration and the rate of change of the active receptor fractions with space, giving, as usual, the strength of the directional bias. This allows easy identification of which gradient gives the best directional cues at different points in space.

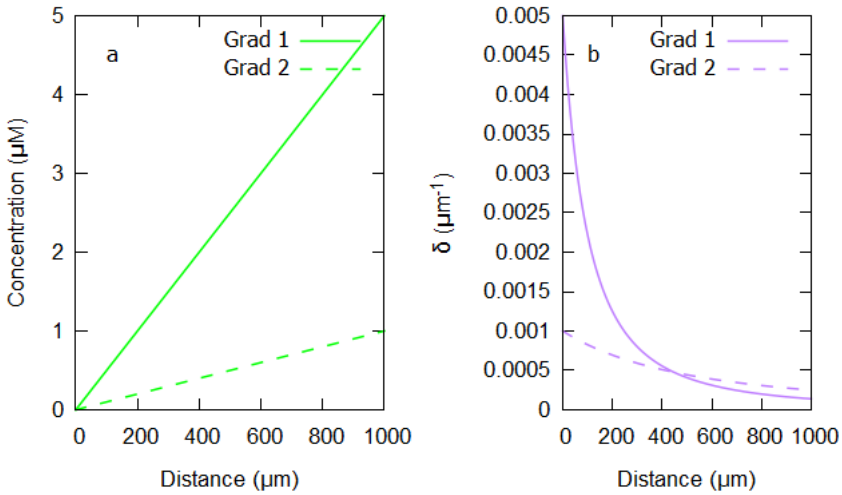

Figure 3: a) Comparison of two linear chemical gradients and b) the corresponding rates of change of the active receptor gradient with space when: $K_d = 1\mu M$, $L = 1000\mu m$

By inspecting Figure 3.b, it can be seen that directional cues are actually stronger in the latter part of the spatial domain for the shallow gradient ($C_1 = 1\mu M$), whereas they are stronger in the former part of the domain for the steep gradient ($C_1 = 5\mu M$). This shows that optimising chemotaxis over an entire gradient is not just a simple case of applying higher concentrations. In many cases it's likely true that a shallower gradient could actually provide superior directional cues over a larger spatial range. It is also apparent from Figure 3.b that there is a value of x for which $\frac{\partial \Omega}{\partial x}$ is the same for both gradients, and it is this coordinate that separates the regions for which each gradient gives superior directional cues. This critical coordinate, x_c, can be derived by equating the respective forms of equation (31) for each gradient, and solving for x. To avoid confusion, the end point concentration of the first gradient shall be named C_{11} and the second C_{12}. Equating these expressions gives

$$\frac{K_d L C_{11}}{(K_d L + C_{11} x_c)^2} = \frac{K_d L C_{12}}{(K_d L + C_{12} x_c)^2}, \tag{36}$$

such that solving for x_c results in the expression

$$x_c = K_d L \left(\frac{\sqrt{C_{12}} - \sqrt{C_{11}}}{\sqrt{C_{11}} C_{12} - \sqrt{C_{12}} C_{11}} \right). \tag{37}$$

In the case of the gradients illustrated in Figure 3, this critical value is $x_c = 447.2\mu m$. So, any $x > x_c$ has increased directional cues for the shallow gradient, and any $x < x_c$ has increased directional cues for the steep gradient. Finally, it could be useful to understand what conditions are required that force $x_c \in [0, L]$, such that there is a guaranteed spatial intersection between the strength of the responses. It can be shown trivially that $x_c > 0$ always, but for $x_c < L$ it is required that

$$K_d L \left(\frac{\sqrt{C_{12}} - \sqrt{C_{11}}}{\sqrt{C_{11}} C_{12} - \sqrt{C_{12}} C_{11}} \right) < L, \tag{38}$$

which, rearranged, gives

$$K_d < \frac{\sqrt{C_{11}} C_{12} - \sqrt{C_{12}} C_{11}}{\sqrt{C_{12}} - \sqrt{C_{11}}} \tag{39}$$

In the case of the two linear gradients shown in Figure 3, it can be shown that $K_d < 2.24\mu M$ is required. Given that $K_d = 1\mu M$, this condition is satisfied and so there will be a value of x_c in the range $x \in [0, L]$, as expected. In order for one gradient to dominate in terms of chemotactic bias, over the whole domain, it must be required that $x_c > L$ (intersection is beyond the considered spatial domain). This means that conditions must be such that the inequality (39) is reversed.

4 Reverse Migration

Some critical information regarding concentration and active receptor gradients should be made very clear at this point. All chemical concentration gradients considered in this thesis shall be positive and increase with x - such that $\frac{\partial C}{\partial x} > 0$ - meaning gradients increase from the beginning of the gradient at $x = 0$ (far LHS) to the end of the gradient at $x = L$ (far RHS). This means that any motion in this same direction implies chemoattraction. Furthermore, if it can be shown that cells travel in the opposite direction, from the end of the gradient at $x = L$ to the beginning of the gradient at $x = 0$, then this explicitly implies chemorepulsion. To understand what direction a cell will be expected to chemotax in, it will be necessary to deduce the derivative of the active receptor gradient with respect to space. This is because cells travel in the direction in which the number of active receptors increases, which is exactly encapsulated in the rate of change of the active receptor gradient, or the derivative. In other words, if the derivative is positive then the number of active receptors increases as the gradient does - and cells chemoattract up the gradient. Conversely, if the derivative is negative then the number of active receptors decreases as the gradient increases - and cells will chemorepulse down the gradient. So, $\frac{\partial \Omega}{\partial x} > 0$ implies chemoattraction, and $\frac{\partial \Omega}{\partial x} < 0$ implies chemorepulsion. Additionally, the magnitude of $\frac{\partial \Omega}{\partial x}$ dictates the strength of the cell response, due to the fact that larger derivatives will give larger changes in the number of active receptors across a cell length. Furthermore, setting $\frac{\partial \Omega}{\partial x} = 0$ gives insight into conditions around which the sign of the derivative changes, meaning that conditions leading to turning points in cell directional cues can be probed. In the interest of simplicity, only linear gradients - resulting from non degradable chemicals - shall be considered in this section.

So, the first question of interest is how exactly might the currently illustrated principles be implemented to induce $\frac{\partial \Omega}{\partial x} < 0$, giving rise to elusive chemorepulsion? From a qualitative perspective, this will never be possible with a single gradient alone. If a single gradient of full antagonist was present then it would not be possible for a gradient of receptor activation to arise, meaning no biased cell motion could ever occur. If a single gradient consisted of molecules of any intrinsic efficacy, then receptor activation would follow increasing chemical concentration - as in Figure 1 - and chemoattraction would occur. If, instead, the gradient was flat, then receptor activation would be uniform, meaning no difference in receptor activation could be resolved across a cell length. Now consider the case of a background of attractant, giving uniform receptor activation, combined with a gradient of competitive inhibitor, which binds to the same receptors but blocks any conformational change. Now, at low inhibitor concentrations, receptor activation from the background of attractant remains largely unchanged. At high concentrations, however, receptor activation from the background of attractant will be significantly decreased. This is because receptors that would would previously have been bound by agonist, and activated, are now being largely occupied by antagonist, and kept in an inactive state. The overall effect of this should be for the active receptor gradient to now decrease such that $\frac{\partial \Omega}{\partial x} < 0$, giving chemorepulsive directional cues.

The key point here is that a competitive inhibitor may theoretically be used to modify the receptor activation induced by an attractant, essentially changing how the cell perceives its environment and causing a cell directional bias different from what would be expected from the attractant alone.

4.1 Chemorepulsion

For this case there is a flat background of attractant, which shall be assumed to be a non-degradable full agonist ($\alpha = 1$), and a linear gradient of inhibitor, which shall be assumed to be a non-degradable full antagonist ($\alpha = 0$). Denoting the attractant background with subscript b and the inhibitor gradient with subscript i, and assuming the inhibitor gradient starts from zero concentration ($C_{0i} = 0\mu M$), the forms of the chemical profiles can be deduced from equation (12) as

$$C_b(x) = C_{1b} \tag{40}$$

and

$$C_i(x) = \frac{C_{1i}x}{L}. \tag{41}$$

The functional form of the active receptor gradient can then be found, as before, by plugging these gradients into equation (5), giving

$$\Omega(x) = \frac{\frac{C_{1b}}{K_b}}{1 + \frac{C_{1b}}{K_b} + \frac{C_{1i}x}{K_i L}}. \tag{42}$$

It should be noted that, in all subsequent representations of the dissociation constant, K_d, the lower case d shall be replaced by a letter denoting the nature of the corresponding chemical (b for background, i for inhibitor or a for attractant). This is to avoid unnecessarily messy and confusing equations when further complexities are incorporated into the model. Now, as described previously, the direction of motion induced by this active receptor gradient can be probed by taking the derivative with respect to space, giving

$$\frac{\partial \Omega}{\partial x} = -\frac{\frac{C_{1b}C_{1i}}{K_b K_i L}}{\left[1 + \frac{C_{1b}}{K_b} + \frac{C_{1i}x}{K_i L}\right]^2}. \tag{43}$$

As concentrations and dissociation constants can only physically occupy positive values - and distances here are defined in such a way that only positive values exist - this expression is guaranteed to be negative, such that $\frac{\partial \Omega}{\partial x} < 0$ always. This means that this system shall always result in a chemorepulsive directional bias, as long as the magnitude of $\frac{\partial \Omega}{\partial x}$ is large enough for cells to be able to resolve a difference in the number of active receptors across their length.

4.1.1 Heat Map Representation

Insightful heat maps can be attained from expressions like equation (43). This is because, as explained previously, the magnitude of $\frac{\partial \Omega}{\partial x}$ gives the strength of the expected chemotaxis, and its sign gives the direction of motion. So, if $\frac{\partial \Omega}{\partial x}$ is plotted on the z-axis of a heat map, hot colors can correspond to positive values, and chemoattraction, and cold colors can correspond to negative values, and chemorepulsion. Furthermore, larger magnitudes of $\frac{\partial \Omega}{\partial x}$ can be illustrated by increasing levels of brightness, allowing for easy identification of regions of strong and weak chemotaxis. Now, if the space over which chemotaxis is being observed, $x \in [0, L]$, is plotted on the x-axis, then it is a simple process to evaluate the chemotactic impact of changing a key parameter in equation (43). Say, for example, the concentration of the attractant background, C_b, is allocated to the y-axis, then each value of C_b in the considered range will correspond to a horizontal strip that will show how chemotaxis is expected to vary over the spatial range for that specific value. This gives a chemotactic map that allows the effect of key parameters on the system to be deduced. An example of this type of representation is illustrated in Figure 4.

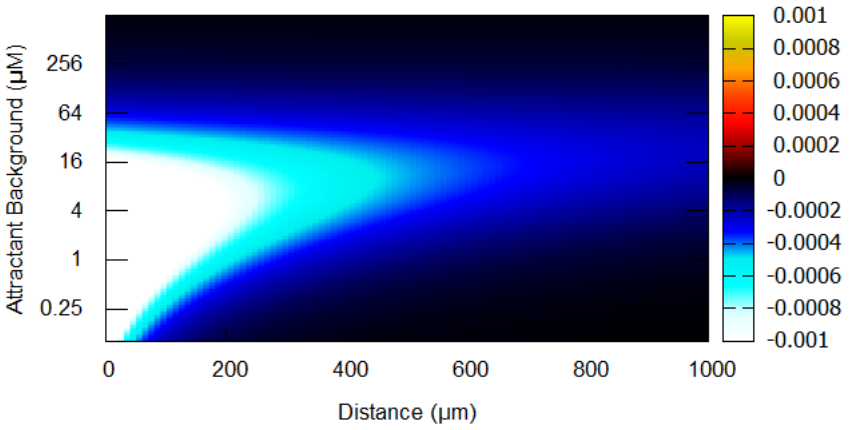

Figure 4: Analytical heat map illustrating the rate of change in the proportion of receptors activated per unit length on the z-axis. Positive values are rendered in warm colours and correspond to a bias to the RHS, and chemoattraction. Negative values are rendered in cold colours and corresponding to a bias to the LHS, and chemorepulsion. The magnitude of this value gives the strength of the response, indicated by brightness. Plotted on the y-axis is the concentration of the agonist background ($K_b = 1\mu M$, $\alpha_b = 1$) and the x-axis shows variation with space. A $0 - 200\mu M$ linear gradient of antagonist ($K_i = 10\mu M$, $\alpha_i = 0$) has been assumed. The overall output indicates expected response strength and direction at different points in space, as the agonist background is varied.

From Figure 4, it can be seen that only chemorepulsion, denoted with cold colors, shall be observed in this system, as expected from equation (43). The strength of the response, however, varies significantly with both space and the attractant background. The strongest chemorepulsion, denoted in white, is always seen at the LHS. This makes sense as, according to Figure 2.a, there are larger changes in receptor binding between the - relatively -

smaller concentrations at the beginning of a gradient, and this tails off as concentration increases. This same principle can be applied to the inhibitor gradient in this system, except that inhibitor binding ultimately detracts from receptor activation. This means that larger reductions in receptor activation will be seen between the smaller concentrations at the start of the gradient, and that smaller reductions in receptor activation will occur over these same differences in concentration located at the - relatively - larger concentrations at the end of the gradient. There is clearly a sweet spot, relative to the attractant background, where chemorepulsion occurs optimally over the whole region. This point, upon observation, is around $15\mu M$. For background concentrations below this value, there is an increasingly small range of receptor activation that can be interfered with over the given space. This means that there is less space for the large reductions in receptor activation that lead to strong chemorepulsion, meaning that stronger chemorepulsion occurs over an increasingly reduced domain. For background concentrations above $15\mu M$ the ratio $\frac{C_{1i}}{C_{1b}}$ gets increasingly small, meaning that reductions in receptor activation due to the inhibitor become increasingly obsolete. This is simply because there is - relatively - much more attractant than inhibitor, so attractant starts binding overwhelmingly more than the inhibitor. This effectively nullifies the reduction in receptor activation seen from the inhibitor, leaving only the uniform receptor activation of the attractant background.

4.1.2 Simulations

So far, all insight has been extracted from analytical math based on the equilibrium state. This is because the maths of the time independent system is simple enough to be effectively manipulated and interpreted, allowing for easy insight. This means, however, that behaviour at early times, where the analytical maths is too complicated to be of easy use, has not been investigated. Simulations can provide a quick way to investigate effects at early times and avoid some of the assumptions made in the analytical math, like that the concentrations of the source and sink are unchanging, or that the cells provide a continuum degradation effect at all points in space. This generally makes simulations more versatile, however, calculations must be made incrementally in space and time, and for only one parameter regime at a time, meaning that it is a slower process to ascertain what is happening. Equations can be troublesome to derive, but can encompass all parameter permutations in space and time, allowing for a quick and easy way to probe for information that could be otherwise computationally heavy. For instance, equation (43) immediately informs one that only a repulsive regime is ever possible, for all parameters. Coming to the same conclusion via simulation could take much longer, as different parameter combinations must be tested for an appropriate length of time that it is clear an approximately unchanging equilibrium has been reached. As mentioned previously though, simulations can account for many of the approximations made in analytical mathematics, and provide insight into additional biological mechanisms that could be too troublesome to incorporate into an analytical model. Ultimately, employing a blend of analytical and computational mathematics, depending on the nature of the problem at hand, can provide a very powerful approach that can allow for all bases to be covered in the most

efficient and elegant way possible.

So, in the interest of probing dynamics at early times, and further confirming the results of the analytical mathematics presented, simulations were run using parameters estimated to be physically accurate. Changes in concentration, according to the diffusion equation, were calculated using the Du Fort-Frankel Method, and translation from this to an active receptor receptor representation was mediated using equation (5). Records of both concentration and proportional numbers of active receptors are kept at regulated intervals in time, allowing for evolutions in time to be easily plotted. The gradient profiles of one such simulation, until approximate equilibrium, are shown in Figure 5.

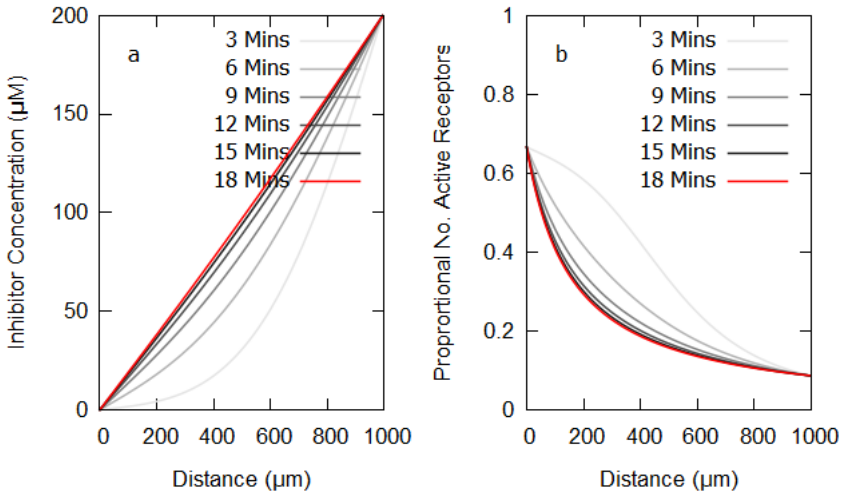

Figure 5: a) Simulated non-degradable inhibitor diffusing to linear equilibrium and b) corresponding temporal effect on the active receptor gradient when: $C_{1b} = 2\mu M$, $K_b = 1\mu M$, $C_{1i} = 200\mu M$, $K_i = 10\mu M$, $D = 20000\mu m^2 min^{-1}$ and $L = 1000\mu m$

It should be noted that only the gradient of non-degradable inhibitor has been plotted in Figure 5.a, as the background of attractant remains constant at $2\mu M$. As expected, the gradient of non-degradable inhibitor becomes increasingly less steep until linear equilibrium is achieved, about 18 minutes into the simulation. This evolving inhibitor gradient interacts differently with the background of attractant at each point in time, which results in a temporally evolving active receptor gradient, until the steady state has been reached. It is clear that all active receptor gradient configurations have $\frac{\partial \Omega}{\partial x} < 0$, meaning repulsive directional cues are expected at all points in time and space, just with varying spatial magnitudes. This supports the analysis of equation (43). When equilibrium has been achieved it can be seen that stronger directional cues will occur at the start of the gradient, as this is where the active receptor gradient is steepest - and cells will see the largest difference in the number of active receptors across their length. Put mathematically, this is where $|\frac{\partial \Omega}{\partial x}|$ is largest. Conversely, weaker responses will be expected at the end of the gradient distances due to a shallower active receptor gradient.

A further advantage of using a simulation, with discrete cell dynamics, is that the cellular response to the environment can be visualised, especially using a 2D render in terms of receptor activation. Figure 4 introduced a very convenient receptor activation rendering scheme, plotting the rate of change of the proportion of receptors activated per unit length $\left(\frac{\partial\Omega}{\partial x}\right)$, which shall be implemented in all subsequent simulations to allow easy correlation between analytical and numerical analysis. This scheme is powerful as positive values, rendered in warm colors, correspond to positive migration, and negative values, rendered in cold colors, correspond to negative migration, allowing for easy identification of regions of attraction and repulsion. On top of this, the magnitude of this value, indicated by brightness, directly relates to the strength of the expected chemotaxis. On this note it is easy to translate any considered magnitude of $\frac{\partial\Omega}{\partial x}$ into an approximate difference in the proportion of active receptors across a cell ($\Delta\Omega$), of length W, that is located at that point in the gradient. This is achieved trivially via the relation

$$\Delta\Omega = \left\| \frac{\partial\Omega}{\partial x} \right\| W, \tag{44}$$

meaning that a cell of length $10\mu m$, immersed at a point in the gradient for which $|\ \frac{\partial\Omega}{\partial x}\ | = 0.001$, is experiencing $\Delta\Omega = 1\%$ across its length. As $|\ \frac{\partial\Omega}{\partial x}\ | = 0.001$ is the largest value considered in the scheme, it is thus assumed, for a cell of length $10\mu m$, that any $\Delta\Omega > 1\%$ will not give any increase in the expected chemotactic response. A snapshot of the simulation illustrated in Figure 5, at equilibrium and rendered as above, has been provided in Figure 6.

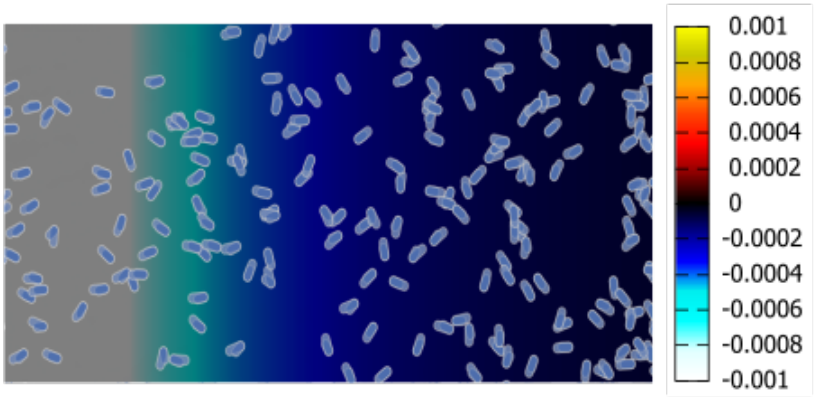

Figure 6: Simulation snapshot after 18 minutes, when the steady state has approximately been reached, for: $C_{1b} = 2\mu M$, $K_b = 1\mu M$, $C_{1i} = 200\mu M$, $K_i = 10\mu M$, $D = 20000\mu m^2 min^{-1}$ and $L = 1000\mu m$

It is clear that this snapshot further confirms the repulsive nature of the system under consideration. Reverse migration is strongest at the left, where the active receptor gradient is steepest, and tails off to the right, as expected from Figure 5.b. This snapshot also correlates very easily with the analytical heat map shown in Figure 4. Specifically, the simulation snapshot corresponds to the horizontal strip of data when the attractant background is at $2\mu M$,

when the parameters of both mathematical systems match. A final advantage of using a discrete simulation is that the individual cells can be tracked, allowing for average cell velocities to be evaluated over a range of time and space. This means that the velocity of the cells in the simulation can be tracked explicitly in the steady state. This is illustrated in Figure 7, where it can be seen that cell velocities are negative - implying repulsion - and strongest at the left, as expected.

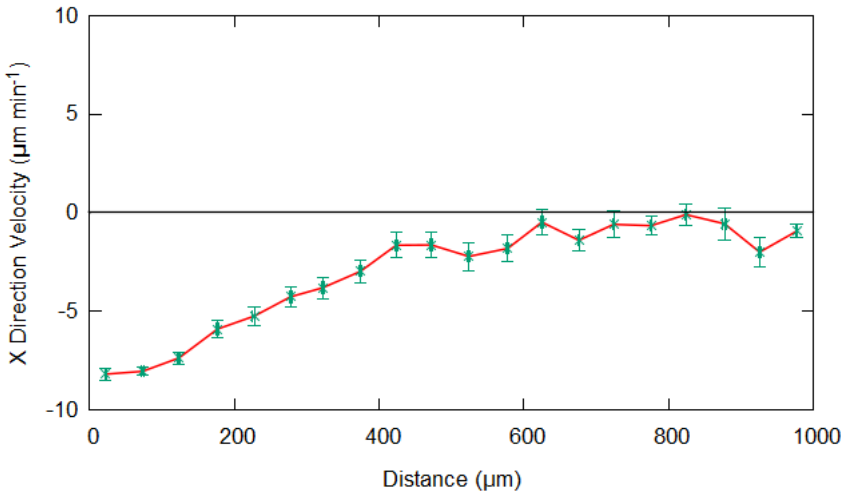

Figure 7: Average simulated velocity output for times after 18 minutes, when the steady state has approximately been reached, for: $C_{1b} = 2\mu M$, $K_b = 1\mu M$, $C_{1i} = 200\mu M$, $K_i = 10\mu M$, $D = 20000\mu m^2 min^{-1}$ and $L = 1000\mu m$.

4.1.3 Experiments

The next natural step is to test the validity of the model, so far developed purely using mathematics, via wet lab work. The cells that shall be used in all further experimental work in this thesis are wild-type NC4 *D. discoideum*. While the commonly used axenic strains are very easy to genetically manipulate - and so are of great use when it is desirable to compare the effects of various gene mutations - they have defects in motility dynamics when compared to wild-type *D. discoideum* [240]. As it is only cellular motility that is of interest to the experiments in this thesis, it makes sense to use the wild-type strain. Additionally, and as discussed previously, there are many analogues of cAMP - a very strong chemoattractant for *D. discoideum* - available, with variations in resistance to enzymatic degradation as well as potential intrinsic efficacy. This will be key in testing out the effects of combinations of chemotactic factors of different properties, as illustrated in the mathematics.

All parameters, up to this point, have been chosen with the intention of testing the given conditions on *D. discoideum*, in an Insall chamber. As such, all dissociation constants have been selected in an attempt to match *D. discoideum* mechanics as closely as possible. Additionally, the $1mm$ distance illustrated in all previous figures corresponds to the length of the bridge, on which both gradients are imposed and cells are imaged, in an Insall chamber. Deducing the validity of the model is now simply a case of imposing the same conditions

demonstrated in the mathematics sections, and testing if the cells replicate the predicted behaviour. The only issue that remains is selecting an attractant and an inhibitor that have the same properties as those used in the maths.

A reported non-degradable attractant for *D. discoideum*, with a dissociation constant of about $1\mu M$ - for the cAR1 receptor - is the non-degradable analogue of cAMP, Sp-cAMPS [196]. To test if this chemical has the desired properties one can compare predicted behaviour, using maths, to experimental output. The most insightful mathematics that can be implemented here would be a heat map, similar to Figure 4, that illustrates how directional cues are expected to change with space as the steepness of a perfect, non-degradable, agonist gradient is varied. Denoting the attractant gradient with subscript a, it is once again required to have a functional form for the non-degradable attractant gradient, which can be deduced from equation (12) as

$$C_a(x) = \frac{C_{1a}x}{L}, \tag{45}$$

assuming the gradient starts from zero concentration. Plugging this into equation (5) to attain the form of the active receptor gradient gives

$$\Omega(x) = \frac{\frac{C_{1a}x}{K_aL}}{1+\frac{C_{1a}x}{K_aL}}, \tag{46}$$

meaning that the all important derivative can be deduced as

$$\frac{\partial\Omega}{\partial x} = \frac{C_{1a}}{K_aL\left[1+\frac{C_{1a}x}{K_aL}\right]^2}. \tag{47}$$

It can be seen that this expression is positive always, meaning that only positive migration is possible, as expected. Figure 8 shows how $\frac{\partial\Omega}{\partial x}$ changes with both space and final gradient concentration, C_{1a}.

It is clear from Figure 8 that the strongest positive migration, from a linear gradient of non-degradable attractant, always occurs at the start of the gradient. As mentioned previously, this makes sense due to the fact that there are larger changes in receptor binding - and activation - between the smaller concentrations in a gradient. This means that the difference in the proportion of active receptors across a cell length will be larger, resulting in stronger chemotaxis. As with Figure 4, there is a critical final concentration (about $2\mu M$) at which chemoattraction will occur optimally across the entire space. As final gradient concentrations tend from this value to zero, the active receptor gradient will become similarly less steep - resulting in increasingly small values of $\frac{\partial\Omega}{\partial x}$ and reduced migration. For concentrations above this critical value, the smaller concentrations - between which there are larger changes in receptor binding, and activation - occur over an increasingly reduced spatial range. This means that there will be increasingly good positive migration over an increasingly small range right at the start of the gradient. This also means that the larger concentrations - between which

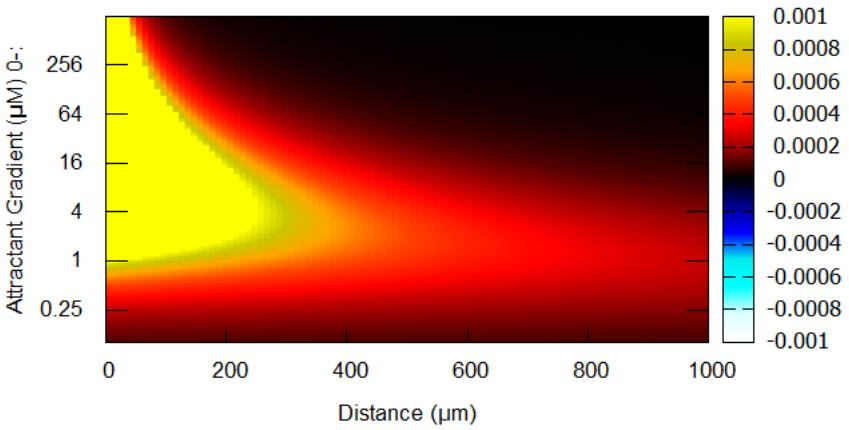

Figure 8: An analytical, chemotactic heat map. Plotted on the y-axis is the final gradient concentration of a non-degradable attractant starting from zero concentration ($K_a = 1\mu M$, $\alpha_a = 1$) and the x-axis shows variation with space. The overall output indicates expected response strength and direction at different points in space, as the final gradient concentration is varied. For additional details on heat map interpretation refer to Figure 4.

there are smaller changes in receptor binding - come about increasing quick in the gradient, meaning reduced chemotaxis occurs over more of the spatial domain. From a qualitative perspective, if a cell were to be immersed in a flat background of non-degradable attractant, then receptor activation would be at a constant value over the entire space. This would imply $\frac{\partial \Omega}{\partial x} = 0$ always, meaning there are no changes in receptor activation at any point and no resultant directional bias of any kind. Figure 9 gives the experimental output of both a gradient and background of Sp-cAMPS, to be compared with this insight.

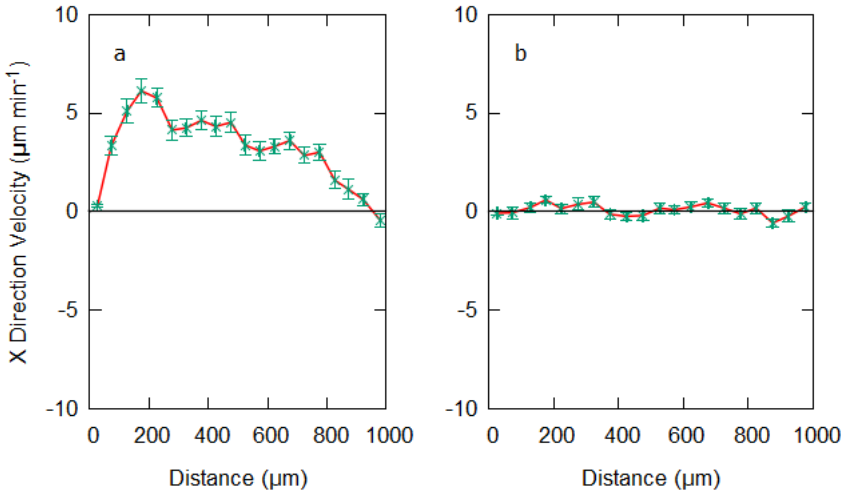

Figure 9: Measured average *D. discoideum* velocities, at equilibrium, for a) $0-2\mu M$ gradient and b) $2\mu M$ background of Sp-cAMPS.

It is clear from Figure 9.a that a $2\mu M$ gradient of Sp-cAMPS gives a peak in response at the start of the gradient, with the strength of the response tailing off with distance, and a flat

background gives no directional bias, as expected. It should be noted that although Figure 8 implies that the velocity at $x = 0$ should be in fact the greatest velocity over the area, in the wet lab experiments this is actually the boundary between the bridge and central well of the Insall chamber. This means that this the point at which cells go from no directional bias, in the central well where there is no Sp-cAMPS, to the large directional bias predicted at the start of the gradient of SP-cAMPS. This accounts for the sudden jump in behaviour, seen in the experiment, that was not predicted using the presented mathematical framework. It can further be seen that the response is still strong quite far up the gradient, insinuating that $2\mu M$ is in fact close to the sweet spot concentration seen in Figure 8, further implying that the parameter configuration used in Figure 8 is close to reality. It shall thus be assumed that Sp-cAMPS is indeed a non-degradable agonist of intrinsic efficacy $\alpha = 1$ and $K_d = 1\mu M$.

It is hard to judge whether a chemical is a competitive inhibitor or not, as an inhibitors effect is to keep receptors in a state of inactivation. This means that a gradient of inhibitor in isolation would result in no receptor activation, and no chemotaxis, despite abundant receptor binding. Its nature can only truly be deduced when competed against something which activates, such that behaviour apparent from a reduction in receptor activation can be made clear. It is therefore quite hard to suggest a candidate for a non-degradable competitive inhibitor for cAR1 receptors in *D. discoideum*. A starting point, however, could potentially be the "chemorepellent" 8-CPT-cAMP [50]. Upon inspection of this paper, it is apparent that *D. discoideum* cAMP secretion has not been accounted for - and therefore has not been suppressed - meaning that an unintended background of cAMP, an agonist, could be present during the subsequent experiments. If this is the case - and the theories presented thus far in this thesis are to be believed - then the reverse migration observed could, in fact, be a result of 8-CPT-cAMP occupying an antagonistic role and reducing levels of receptor activation, from the cAMP background, close to the micro-pipette tip. This would give an active receptor gradient that increases outwards from the pipette tip and would cause the cells to act in the manner observed. If this theory is to be believed, it is necessary to show that a gradient of 8-CPT-cAMP - with caffeine present to block cAMP secretion - gives no resultant directional cues. As 8-CPT-cAMP is not actually going to be used in this section, this experiment is presented later on in section 4.1 and is illustrated in Figure 35 - where it is clear that there is no biased response. This means that 8-CPT-cAMP potentially serves the function of an antagonist, but it is unclear whether or not it is phosphodiesterase resistant. However, another cAMP analogue - Sp-8-CPT-cAMPS - also exists and is, structurally, a combination of 8-CPT-cAMP and Sp-cAMPS [241]. As Sp-cAMPS has already been shown to be non-degradable, this means that Sp-8-CPT-cAMPS could be exactly what is required. A final test that is necessary before testing Sp-8-CPT-cAMPS in combination with other ligands is the behavioural output of a simple gradient, as presented in Figure 10.

Due to lack of motion of any kind in a $200\mu M$ gradient of Sp-8-CPT-cAMPS, it shall be assumed currently that this chemical a non-degradable inhibitor of unknown K_d. For the

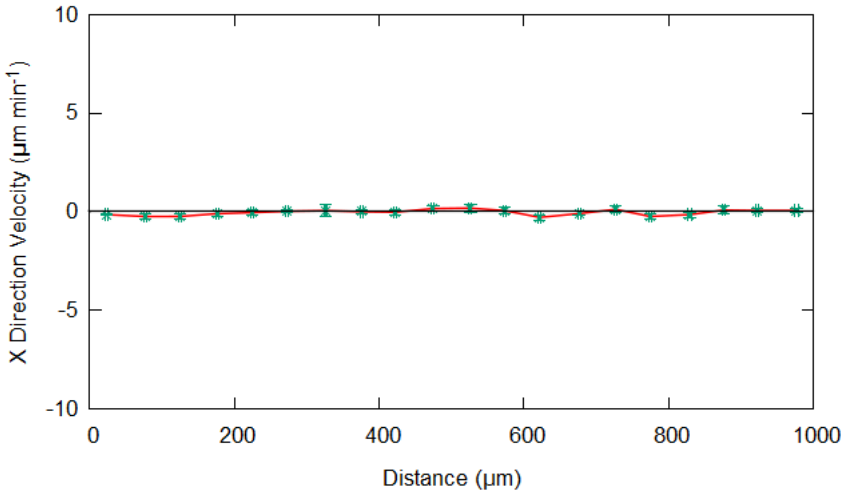

Figure 10: Measured average *D. discoideum* velocities, at equilibrium, for $0 - 200\mu M$ gradient Sp-8-CPT-cAMPS.

purposes of further simulations and analytical work it shall be assumed that the dissociation constant of Sp-8-CPT-cAMPS is $K_d = 10\mu M$. Although this may be entirely inaccurate, these predictions allow insight into what the dynamics of a $K_d = 10\mu M$ non-degradable perfect inhibitor would look like. Upon comparison with experimental output, an educated guess as to the true K_d of Sp-8-CPT-cAMPS can be made. Now that candidates for a non-degradable agonist and antagonist have been intelligently selected, it is possible to test the validity of the model - and the assumptions made on the selected chemicals - by imposing the same conditions illustrated in the above simulations and comparing the behavioural output to that of the mathematics. Figures 11 and 12 show an experiment snapshot and a velocity output, once chemical equilibrium is estimated to have been reached.

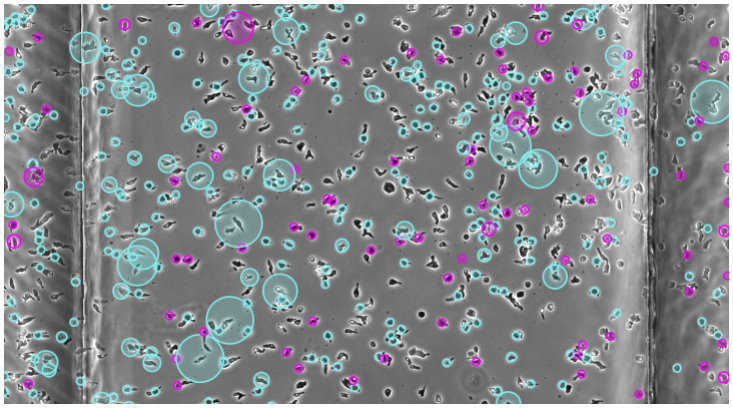

Figure 11: Experiment snapshot, at equilibrium, of NC4 strain of *D. discoideum* subject to a $2\mu M$ background Sp-cAMPS and a $0 - 200\mu M$ gradient of Sp-8-CPT-cAMPS. Cyan circles correspond to motion to the LHS (chemorepulsion) and magenta circles correspond to motion to the RHS (chemoattraction), with the size of the circle giving the magnitude of the x direction velocity.

Figure 11 displays cells velocities at different points in space as calculated via a cell tracker developed by L. Tweedy (paper in preparation). Circles rendered in cyan correspond to mo-

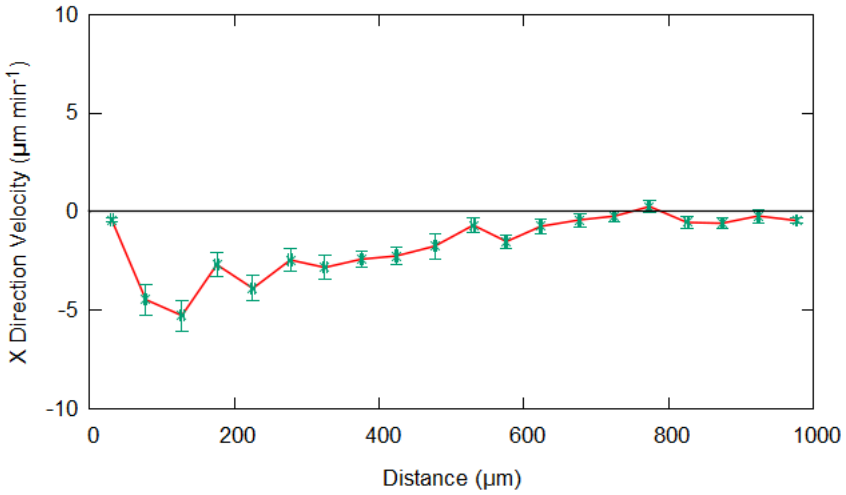

Figure 12: Measured average cell velocities, at equilibrium, of NC4 strain of *D. discoideum* subject to a $2\mu M$ background Sp-cAMPS and a $0 - 200\mu M$ gradient Sp-8-CPT-cAMPS.

tion to the left, indicating reverse migration, and circles rendered in magenta correspond to motion to the right, indicating positive migration. The size of the circle illustrates the magnitude of the relative x-direction velocity. This same rendering system shall be implemented in all subsequent experimental analysis. The output clearly shows that negative migration is occurring over the spatial domain, with stronger responses being observed at the LHS. This is further reinforced by the equilibrium velocity profile in Figure 12, which shows the expected tailing off in the strength of the repulsion, as predicted from both simulations and heat maps. The only difference in the experimental output once again derives from the fact that the maths does not account for the boundary separating the region of strongest repulsion, at the very start of the gradient, and the well of cells with no directional bias, just beyond this. This means that whereas simulated cells - in Figure 7 - have increasing repulsive velocity as they tend toward $x = 0$, real life cells - in Figure 12 - experience the same increase in repulsive velocity as they approach $x = 0$ but eventually encounter the boundary to the well, forcing their x-direction velocities from high values down to zero. The overall conclusion is that the cell behaviour matches the output predicted from the mathematics, down to expected response strengths in different regions. This implies that the model is in fact valid, and that the assumptions made on the cAMP analogues are close to reality. It shall thus be assumed in subsequent mathematical analysis that Sp-8-CPT-cAMPS is a non-degradable competitive antagonist ($\alpha = 0$) with a dissociation constant, relative to the cAR1 receptor, of $K_d = 10\mu M$. Furthermore, the strong experimental recapitulation verifies that the equilibrium state assumption made in section 1.5.1 - that receptors become bound as quickly as the corresponding complexes dissociate - was valid.

A corollary also becomes apparent at this point; constitutively active cAR1 receptors either do not exist in this system or are present in such small amounts that they can be considered negligible. This can be deduced due to the fact that any proportion of unbound receptors being active essentially equates to an attractant background. So, if constitutively active re-

ceptors were present in quantities that could interfere with the currently presented model, then an externally imposed gradient of competitive antagonist would - in the absence of any other signals - induce reverse migration to some degree, similar to the behaviour observed in Figure 12. It can be seen clearly that one such gradient - illustrated in Figure 10 - gives a negligible response, hence there is either an insignificant amount of constitutive receptor activity or none at all.

It should be further noted that although the terms repulsion and reverse migration have been used in this section quite abundantly, they refer simply to the fact that cells have been migrating to the left, or from $x = L$ to $x = 0$, which, due to the fact that almost exclusively all gradients will increase with x in this thesis, was specified at the start of Section 3 to be the direction of chemorepulsion. For this first and most simple of cases, however, the attractant gradient was chosen not to increase with x, but to remain a constant. This technically means that travel in the direction of decreasing x does not imply reverse migration in the sense that cells are migrating away from a high concentration of agonist, but it does imply migration in contrast to that expected from the background of attractant alone, which was the whole point. As all gradients from this point onwards truly will truly obey $\frac{\partial C}{\partial x} > 0$, and increase with x, it made sense to set up the standard that migration with increasing x explicitly implies chemoattraction, and migration with decreasing x explicitly implies chemorepulsion.

4.1.4 Imperfect Attractant and Inhibitor

One of the advantages of a mathematical model is that it allows one to easily explore the impact of certain ideas and parameter variations. Obviously a model is only as good as the mechanics incorporated into it, and biology is too big to be encapsulated fully into a math model, but as long as the primary influencing factors are accounted for then an approximation as to behavioural outputs under certain parameter configurations - or certain combinations of biological mechanisms - can be made. A particularly intriguing variation in the model to consider is the possibility of partial agonism. This could mean that molecules of the attractant background do not activate every receptor bound ($\alpha < 1$), or that molecules of inhibitor activate a small fraction of bound receptors ($\alpha > 0$). Analytical mathematics can now be implemented in a very similar manner as previously to probe the possibilities of this variation in the model. If the background of attractant and gradient of inhibitor have intrinsic efficacies α_b and α_i, respectively, where $\alpha_b > \alpha_i$, then the active receptor gradient can again be found, according to equation (5), as

$$\Omega(x) = \frac{\frac{\alpha_b C_{1b}}{K_b} + \frac{\alpha_i C_{1i} x}{K_i L}}{1 + \frac{C_{1b}}{K_b} + \frac{C_{1i} x}{K_i L}}, \tag{48}$$

giving the derivative with respect to space as

$$\frac{\partial \Omega}{\partial x} = \frac{\frac{\alpha_i C_{1i}}{K_i L} + \frac{C_{1b} C_{1i}(\alpha_i - \alpha_b)}{K_b K_i L}}{\left[1 + \frac{C_{1b}}{K_b} + \frac{C_{1i} x}{K_i L}\right]^2}. \tag{49}$$

Once again, a heat map representation of equation (49) is a most insightful way to ascertain expected cell responses in different regions, as specific parameters are varied. All parameters shall be kept consistent with Figure 4, allowing for a comparison of expected behaviour between the two models. Figure 13 gives one such heat map.

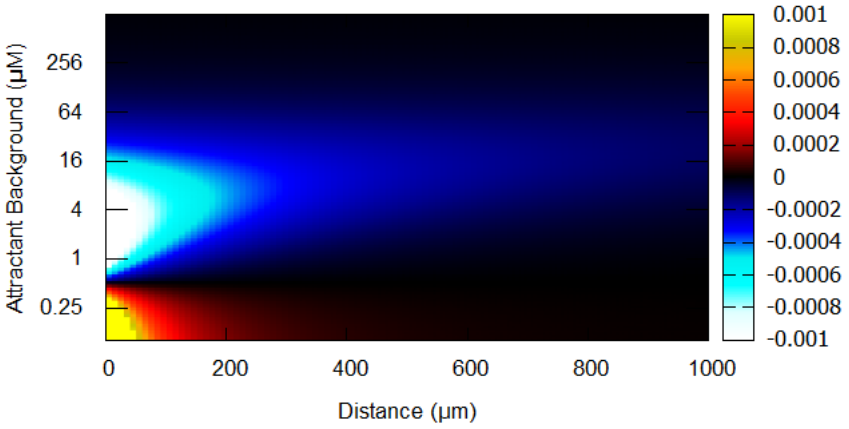

Figure 13: An analytical, chemotactic heat map. Plotted on the y-axis is the concentration of the imperfect agonist background ($K_b = 1\mu M$, $\alpha_b = 0.75$) and the x-axis shows variation with space. A $0 - 200\mu M$ linear gradient of imperfect antagonist ($K_i = 10\mu M$, $\alpha_i = 0.25$) has been assumed. The overall output indicates expected response strength and direction at different points in space, as the imperfect agonist background is varied. For additional details on heat map interpretation refer to Figure 4.

Some very interesting distinctions arise when partial agonism is accounted for. The first is that the resultant repulsion becomes less effective than the perfect attractant and inhibitor case, as is apparent from the decrease in light colors, representing smaller differences in receptor activation across the cell length - and reduced directional cues. The second is that the repulsion only occurs over a certain range of attractant background concentrations, specifically at higher concentrations, below which a chemoattractive regime becomes possible. Mathematically this is very intriguing as the region separating these two regimes is technically a turning point in the direction of the cell response. As repulsion implies $\frac{\partial \Omega}{\partial x} < 0$, and motion to the left, and attraction implies $\frac{\partial \Omega}{\partial x} > 0$, and motion to the right, the critical background concentration that separates these two behaviours is where $\frac{\partial \Omega}{\partial x} = 0$. This means that one should be able to set the LHS of equation (49) to zero and solve this for the critical attractant background, $C_{1b}*$, as well as deduce further key information regarding the nature

of this turning point. Put mathematically,

$$\frac{\partial \Omega}{\partial x} = 0 \quad \Leftrightarrow \quad C_{1b}* = \frac{\alpha_i K_b}{\alpha_b - \alpha_i}. \tag{50}$$

As long as the RHS of this relation is positive then a real value of attractant background, that separates the cell response direction, exists. Due to the fact that $\alpha_b > \alpha_i$, giving a positive denominator, and $K_b > 0$ always, the only requirement that the direction of motion can be modulated via the attractant background is that $\alpha_i > 0$, meaning the inhibitor must activate receptors to some degree.

Intriguingly, the dissociation constant of the inhibitor, K_i, has no influence on the turning point. Figure 14 shows how the value of $C_{1b}*$ varies with α_i, for some different values of α_b and K_b.

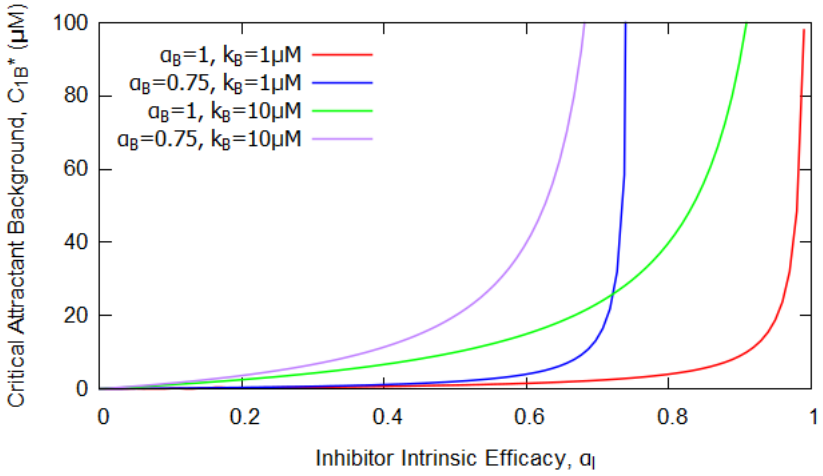

Figure 14: Some curves showing how values of $C_{1b}*$, the attractant background concentration separating positive and reverse migration regimes, vary with α_i, the intrinsic efficacy of the inhibitor, for some values of α_b and K_b.

From this Figure it can be seen, from a graphical perspective, that both of the conditions $\alpha_b > \alpha_i$ and $\alpha_i > 0$ are required to give a physical critical attractant background concentration that separates directional regimes. It is also clear that the value of $C_{1b}*$ increases with K_b, and that the value of $C_{1b}*$ increases as $\{\alpha_b - \alpha_i\} \to 0$, or as the levels of bound receptor activation of the attractant and inhibitor become increasingly similar - as can also be seen trivially from equation (50).

4.2 Competing Linear Gradients

Now that predicted novel migration behaviours, via competitive inhibitor induced interference with levels of receptor activation, have been validated using real cells, the mathematical model can be extended to predict further complexities in migration. If these, in turn, can be similarly validated via wet lab work then the strength of the model can be reinforced even

further. The more unexpected the prediction, the stronger the argument becomes upon experimental verification. The next logical step would be to compete a linear gradient of competitive inhibitor against a linear gradient of attractant, rather than a background. Reverse migration seen in this case could be perceived as true chemorepulsion, in the sense that cells would be migrating away a high concentration of attractant, rather than simply migrating in a fashion contrary to that expected from a background of attractant. Initially, this situation shall be probed with arbitrary, perfect attractant and inhibitor gradients - denoted with subscripts a and i respectively - such that $\alpha_a = 1$, $\alpha_i = 0$ and the chemical gradients have forms as illustrated in equation (12). The active receptor gradient can then be found, as usual, by plugging these expressions into equation (5), giving

$$\Omega(x) = \frac{\frac{1}{K_a}\left\{\left(\frac{C_{1a}-C_{0a}}{L}\right)x + C_{0a}\right\}}{1 + \frac{1}{K_a}\left\{\left(\frac{C_{1a}-C_{0a}}{L}\right)x + C_{0a}\right\} + \frac{1}{K_i}\left\{\left(\frac{C_{1i}-C_{0i}}{L}\right)x + C_{0i}\right\}}. \tag{51}$$

The derivative with respect to space, dictating both the response strength and direction, can then be deduced as

$$\frac{\partial\Omega}{\partial x} = \frac{\frac{C_{1a}-C_{0a}}{K_a L} + \frac{C_{0i}C_{1a}-C_{0a}C_{1i}}{K_a K_i L}}{\left[1 + \frac{1}{K_a}\left\{\left(\frac{C_{1a}-C_{0a}}{L}\right)x + C_{0a}\right\} + \frac{1}{K_i}\left\{\left(\frac{C_{1i}-C_{0i}}{L}\right)x + C_{0i}\right\}\right]^2}. \tag{52}$$

Repulsion can be achieved if the RHS of equation (52) is negative. As the denominator will always be positive when one considers physically relevant parameters, reverse migration will be seen for any parameter regime that results in the numerator being negative. Put mathematically,

$$\frac{\partial\Omega}{\partial x} < 0 \quad \Leftrightarrow \quad \frac{C_{1a} - C_{0a}}{K_a L} + \frac{C_{0i}C_{1a} - C_{0a}C_{1i}}{K_a K_i L} < 0, \tag{53}$$

which can be rearranged in the form

$$C_{1i} > \frac{1}{C_{0a}}\left\{K_i(C_{1a} - C_{0a}) + C_{0i}C_{1a}\right\}. \tag{54}$$

This expression allows for insight into the requirements for repulsion in a competing gradient system. First of all, it can be seen that $C_{0a} = 0\mu M$ means that it is necessary for $C_{1i} > \infty$ to induce reverse migration. This is, of course, impossible, which proves that the attractant gradient must start from a non-zero value in order for repulsion to be possible. This also makes sense from an intuitive perspective because if $\frac{\partial\Omega}{\partial x} < 0$ then the active receptor gradient is increasing as $x \to 0$. This means that $\Omega(x = 0) \neq 0$ in order for repulsion to occur, and as receptor activation can only occur as a result of attractant binding, this implies that the attractant gradient must start from a non-zero value, such that $C_{0a} \neq 0\mu M$. If the inhibitor gradient is chosen to start from zero concentration, such that $C_{0i} = 0\mu M$, it can be seen that

repulsion can still be induced as long as the condition

$$C_{1i} > \frac{K_i(C_{1a} - C_{0a})}{C_{0a}} \tag{55}$$

is satisfied. So, as $C_{0i} \neq 0\mu M$ is not a requirement for reverse migration, the system shall be permanently simplified by assuming that the linear inhibitor gradient starts from zero concentration. It can be further deduced that there is a critical final inhibitor concentration, $C_{1i}*$, that separates the positive and reverse migration regimes. This is the point at which

$$\frac{\partial \Omega}{\partial x} = 0 \quad \Leftrightarrow \quad C_{1i} = C_{1i}* = \frac{K_i(C_{1a} - C_{0a})}{C_{0a}}. \tag{56}$$

So, if there are two competing gradients of attractant and inhibitor, with $C_{0a} \neq 0\mu M$ and $C_{0i} = 0\mu M$, then the directional response of the system can be modulated via the final inhibitor concentration, C_{1i}, where any $C_{1i} > C_{1i}*$ will result in repulsion away from the high concentration of attractant, and any $C_{1i} < C_{1i}*$ will result in positive migration towards the high concentration of attractant.

This can be interpreted qualitatively by considering that a gradient of attractant supplies a rate of increase in receptor activation across the given spatial domain. A superimposed gradient of inhibitor will then supply a dampening effect on this rate of receptor activation. In cases where $C_{1i} < C_{1i}*$, this dampening effect is sufficient only to reduce to effectiveness of the chemoattraction, but not change the direction of motion. When $C_{1i} > C_{1i}*$ the dampening effect is intense enough to cause the the rate of increase in receptor activation - from the attractant - to become a rate of decrease in receptor activation, with x, resulting in chemorepulsion. The point at which $C_{1i} = C_{1i}*$ defines the moment when the dampening effect from the inhibitor exactly balances the positive rate of receptor activation from the attractant - effectively resulting in uniform receptor activation, and no directional bias.

4.2.1 Heat Map Representation

As before, an insightful way to illustrate these concepts is with a heat map. Similar to before, equation (52) will be plotted in 3D, with $\frac{\partial \Omega}{\partial x}$ on the z-axis, distance on the x-axis, and a parameter of interest on the y-axis. To reiterate, hot colors correspond to $\frac{\partial \Omega}{\partial x} > 0$, and chemoattraction, and cold colors correspond to $\frac{\partial \Omega}{\partial x} < 0$, and chemorepulsion. The brightness corresponds to the magnitude of $\frac{\partial \Omega}{\partial x}$, and the strength of the chemotaxis - due to larger changes in receptor activation across a cell length. It makes sense to vary the final inhibitor concentration, C_{1i}, on the y-axis, as the turning point in cell directional cues - located at $C_{1i} = C_{1i}*$ - should be apparent. Figure 15 gives one such heat map.

Given the parameters used in Figure 15, the value of $C_{1i}*$ can be calculated explicitly - using equation (56) - as $C_{1i}* = 40\mu M$. Upon inspection of the heat map, this final inhibitor concentration is clearly the point at which the direction of motion changes, as expected.

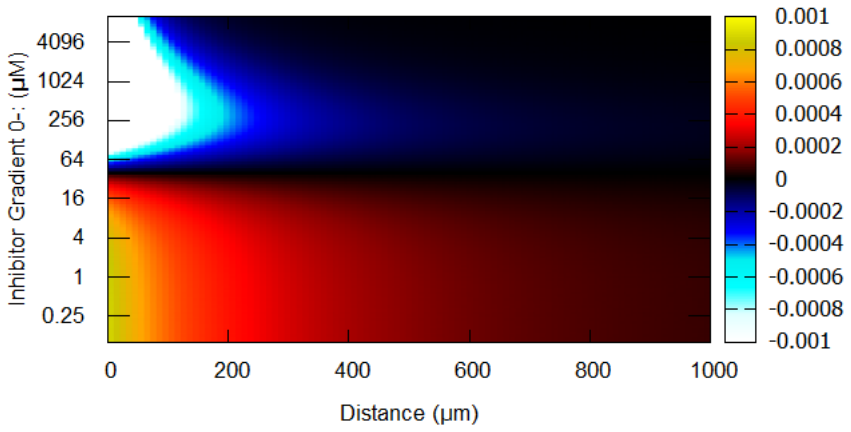

Figure 15: An analytical, chemotactic heat map. Plotted on the y-axis is the final concentration of the antagonist gradient ($K_i = 10\mu M$, $\alpha_i = 0$), which starts from zero concentration, and the x-axis shows variation with space. A $2 - 10\mu M$ linear gradient of agonist ($K_a = 1\mu M$, $\alpha_a = 1$) has been assumed. The overall output indicates expected response strength and direction at different points in space, as the antagonist gradient steepness is varied. For additional details on heat map interpretation refer to Figure 4.

Furthermore, for concentrations $C_{1i} < C_{1i}*$, the dampening effect of the inhibitor on the strength of the positive migration - due to the gradient of attractant - can be seen, with an increase in intensity as $C_{1i} \rightarrow C_{1i}*$. For concentrations $C_{1i} > C_{1i}*$, the rate of decrease in receptor activation, from the inhibitor, outweighs the rate of increase from the attractant, resulting in the expected repulsion. As $C_{1i} \rightarrow \infty$ the small concentrations in the inhibitor gradient - between which there are larger decreases in receptor activation - occur over an increasingly reduced spatial range, meaning that the window of strongest chemorepulsion gets closer and closer to the beginning of the gradient. This also implies that the, relatively, larger concentrations in the inhibitor gradient - between which there are increasingly small reductions in receptor activation - occur sooner in the chemical gradient, meaning that the repulsion tails off at increasingly reduced distances.

4.2.2 Simulations

Once again, it is comforting to employ a discrete cell simulation that accounts for the system elements that have been skipped or approximated in the analytical maths, to further validate the predictions that have made. For this particular case this only includes the diffusion of the attractant and inhibitor to their equilibrium states, at early times. As this section is investigating the effect of a superimposed inhibitor gradient, on top of an attractant gradient, in modifying the chemotactic dynamics that would be observed from a gradient of attractant alone, it is informative to simulate both the gradient of attractant in isolation as well as the combined attractant and inhibitor case, to see how the behaviour changes. According to Figure 15 - by inspecting the base of the heat map - a linear gradient of perfect attractant that starts at $C_{0a} = 2\mu M$ and increases to $C_{1a} = 10\mu M$ over length $L = 1000\mu m$, with

$K_a = 1\mu M$, should give relatively good positive migration in isolation. An additionally imposed linear gradient of perfect inhibitor that starts from zero concentration and increases to $C_{1i} = 1000\mu M$ over the same distance, with $K_i = 10\mu M$, should also give relatively strong reverse migration. As such this shall be the parameter configuration utilised in the subsequent simulations. Figure 16 gives the temporal evolution of the concentration profiles of both the non-degradable attractant and inhibitor, and Figure 17 gives the temporal evolution of the active receptor gradient for the attractant both alone and with the inhibitor.

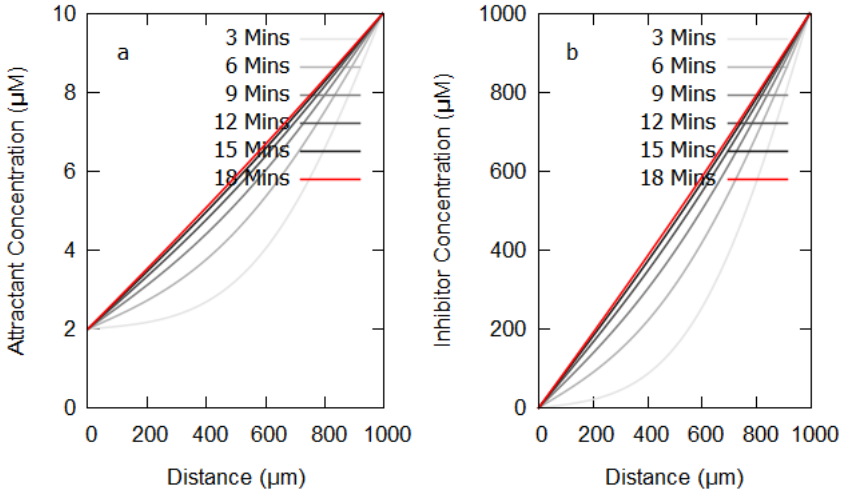

Figure 16: Simulated non-degradable a) attractant and b) inhibitor diffusing to linear equilibrium in a simulation where: $K_a = 1\mu M$, $K_i = 10\mu M$, $D = 20000\mu m^2 min^{-1}$ and $L = 1000\mu m$.

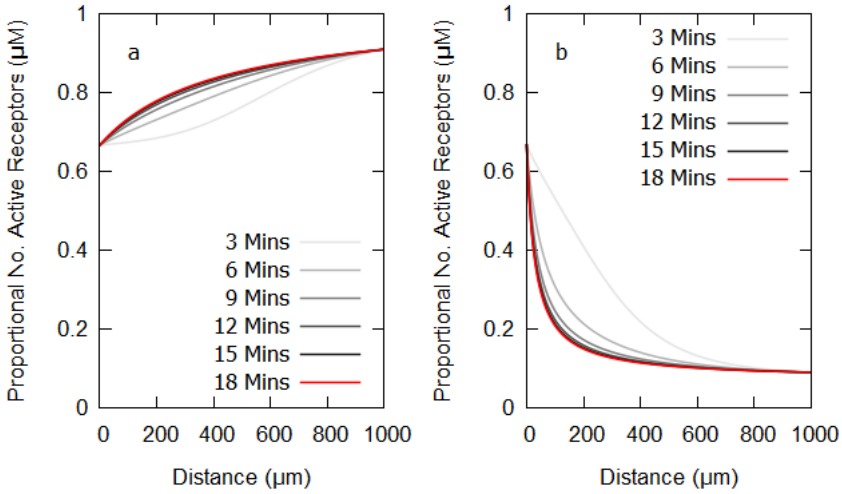

Figure 17: Simulated active receptor gradients for a) gradient of attractant alone and b) gradients of attractant and inhibitor combined, where: $K_a = 1\mu M$, $K_i = 10\mu M$, $D = 20000\mu m^2 min^{-1}$ and $L = 1000\mu m$.

As expected, the non-degradable chemicals in Figure 16 diffuse to linear equilibria, about 18 minutes into the simulations, with the gradients becoming less steep at each time point. This makes sense as molecules diffuse proportionally with the steepness of the gradient, so the

most drastic changes in concentration will occur at early times. Furthermore, the active receptor gradients illustrated in Figure 17 show the expected chemoattraction from the gradient of agonist alone, and the predicted repulsion when the gradient of inhibitor is superimposed. These directional regimes remain constant, although the gradient profiles change - along with expected response strength at different positions - as binding dynamics change according to evolutions in concentration, until chemical equilibrium is reached. Once chemical equilibrium is reached, the peaks in response strength are, as usual, located at the beginning of the gradient. Simulation snapshots - rendered in terms of the rate of change of the fractional proportion of active receptors with space - can be taken to compare the simulation response profile to that of the analytical maths (in Figure 15). This is demonstrated in Figure 18. On top of this, individual cells can be tracked to give an educated guess as to an expected equilibrium velocity distribution, assuming a maximum cell speed of $10\mu m\ min^{-1}$, as shown in Figure 19.

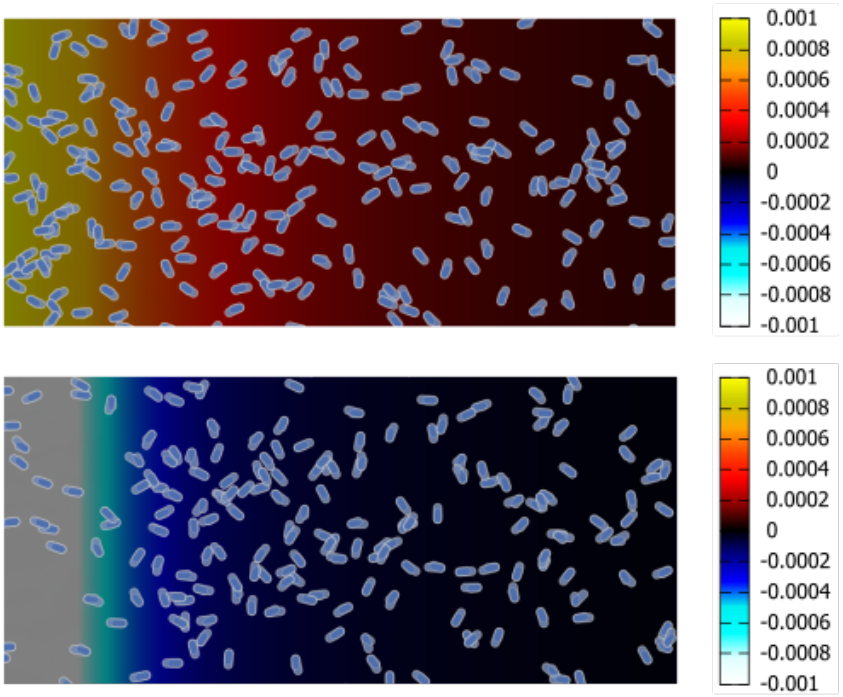

Figure 18: Simulation snapshots after 18 minutes, when the steady state has approximately been reached for a) the attractant alone and b) the attractant in combination with the inhibitor, where: $C_{0a} = 2\mu M$, $C_{1a} = 10\mu M$, $K_a = 1\mu M$, $C_{0i} = 0\mu M$, $C_{1i} = 1000\mu M$, $K_i = 10\mu M$, $D = 20000\mu m^2 min^{-1}$ and $L = 1000\mu m$.

It can be seen from Figure 18 that in the steady state, once diffusion dynamics have become time independent, simulation snapshots with active receptor rendering recapitulate the response profiles predicted from Figure 15 perfectly. The y-axis values in Figure 15 that correspond to the attractant alone and the attractant and inhibitor combined are $C_{1i} = 0\mu M$ and $C_{1i} = 1000\mu M$, respectively. The velocity distributions demonstrated in Figure 19 show the expected positive and reverse migration. Furthermore, the strongest responses occur at the

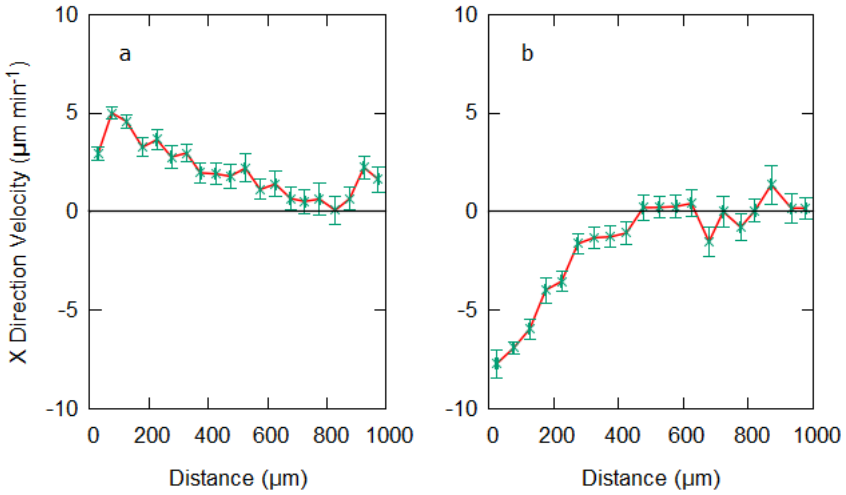

Figure 19: Average simulated cell velocities for times after 18 minutes, when the steady state has approximately been reached, for a) the attractant alone and b) the attractant in combination with the inhibitor, where: $C_{0a} = 2\mu M$, $C_{1a} = 10\mu M$, $K_a = 1\mu M$, $C_{0i} = 0\mu M$, $C_{1i} = 1000\mu M$, $K_i = 10\mu M$, $D = 20000\mu m^2 min^{-1}$ and $L = 1000\mu m$.

LHS, with the strength of the bias tailing off to the RHS, as expected from the steady state active receptor gradients illustrated in Figure 17. The simulations have further proven that repulsion relative to an increasing gradient of attractant is possible from a mathematical perspective. The numerical maths has given additional insight into the concentration dynamics at early times, the relative evolution in the active receptor gradient until the steady state is reached, an estimated equilibrium velocity profile and the time frame over which equilibrium might occur for the given diffusion constant.

4.2.3 Experiments

At this point it is once again vital to validate the model by comparing the mathematical predictions of this slightly more complex argument to experimental output. It has been shown in section 3.1 that the chemicals Sp-cAMPS and Sp-8-CPT-cAMPS approximately serve the purposes of a perfect, non-degradable, attractant and inhibitor with dissociation constants of $K_d = 1\mu M$ and $K_d = 10\mu M$ for the cAR1 receptor of *D. discoideum*, respectively. This means that, theoretically, the behaviour predicted in the simulations section should be closely emulated if the same concentration conditions are imposed over the $1mm$ bridge in an Insall chamber, once the steady state has been reached.

It should be noted that choosing an optimal attractant gradient, that gives strong positive migration in isolation, and optimal inhibitor gradient, that gives strong negative migration upon being superimposed, is actually quite challenging. This is because stronger repulsion will be seen at shallower attractant gradients, where inhibitor binding will cause larger drops in receptor activation across a cell length. This implies that the best repulsion will be seen when the attractant is uniform, but at this point no positive migration can ever be observed. So, the better you make the attraction, the worse the repulsion will become upon imposing

the same inhibitor gradient. Its also true that a steeper inhibitor gradient can be implemented to counter a steeper attractant gradient, but it must also be taken into consideration that $\Omega \in [0, 1]$ only. This means that an inhibitor gradient which is being imposed to cause repulsion relative to a very steep attractant gradient, which gives, for example, $\Delta\Omega = 0.8$ ($\Omega \in [0.2, 1]$) across the spatial domain by itself, can only ever result in a maximum of $\Delta\Omega = -0.2$ across the same length, causing discrepancies in the quality of the chemotaxis. There will always be a trade off. A theoretically perfect situation could be for the attractant gradient to be such that $\Omega \in [0.5, 1]$, and for the additionally imposed inhibitor gradient to cause receptor activation to drop such that $\Omega \in [0.5, 0]$, across $x \in [0, L]$. In this situation, however, very steep gradients would have to be used to reach the $\Omega = 1, 0$ extrema, such that the larger changes in receptor activation, seen between smaller concentrations, occur only at the beginning of the gradient, giving strong chemotaxis only at the far LHS and little to no chemotaxis over most spatial domain. The "sweet spot" concentration configuration which gives substantial chemotaxis over a good length of the gradient would be missed entirely. In summation there is a large amount of information to consider when selecting these gradients. Simulations, however, imply that the current parameter regime should give a satisfactory balance of chemotactic strength and range, if the tested dissociation constants are at least correct to within about an order of magnitude, so this is what shall be tested experimentally. Figures 20 and 21 show experiment snapshots and velocity outputs, in the steady state.

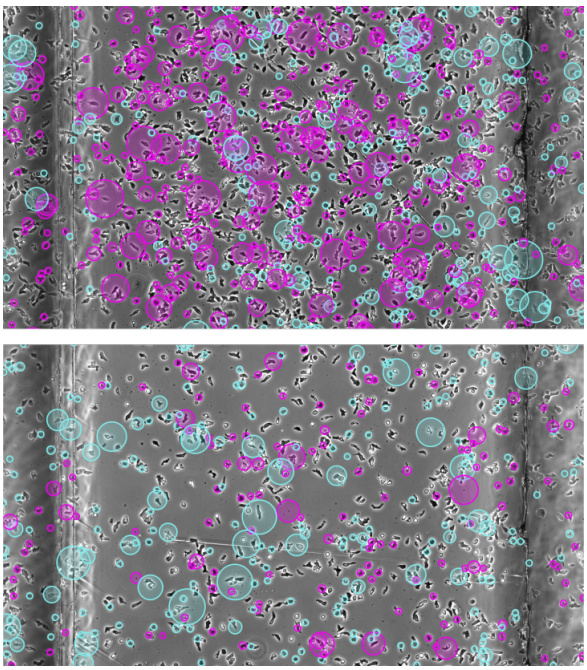

Figure 20: Experiment snapshots, at equilibrium, of NC4 strain of *D. discoideum* subject to a) $2-10\mu M$ gradient Sp-cAMPS alone and b) $2-10\mu M$ gradient Sp-cAMPS in combination with $0-1000\mu M$ gradient Sp-8-CPT-cAMPS, where $L = 1000\mu m$. Cyan circles correspond to motion to the LHS (chemorepulsion) and magenta circles correspond to motion to the RHS (chemoattraction), with the size of the circle giving the magnitude of the x direction velocity.

Figure 20 clearly shows positive migration being prevalent for the gradient of Sp-cAMPS

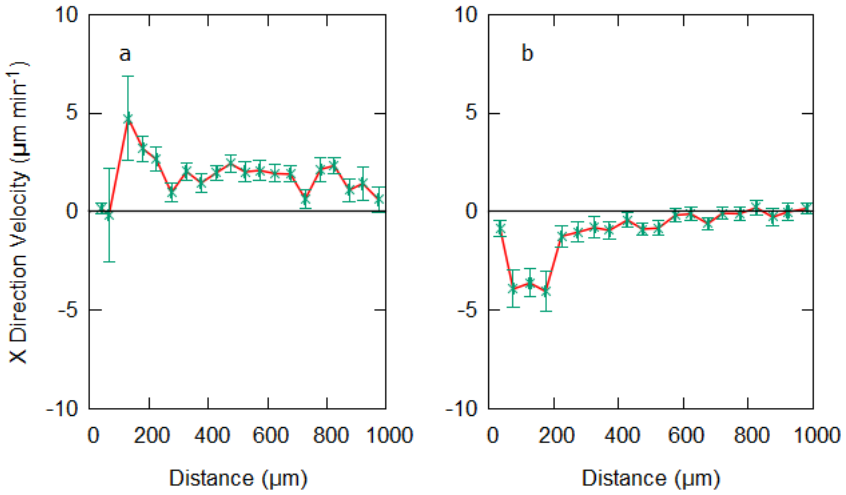

Figure 21: Average experimental cell velocities for times after 18 minutes, when the steady state has approximately been reached, for a) $2-10\mu M$ gradient Sp-cAMPS alone and b) $2-10\mu M$ gradient Sp-cAMPS in combination with $0-1000\mu M$ gradient Sp-8-CPT-cAMPS, where $L = 1000\mu m$.

in isolation, indicated via magenta circles, with reverse migration behaviour emerging when the gradient of Sp-8-CPT-cAMPS is additionally imposed, indicated with cyan circles. The peaks in response, where the largest number of bigger circles reside, undiluted by circles of the opposite response color, clearly occur at the LHS in both cases. This is consistent with the active receptor gradients and steady state simulation renderings demonstrated in Figures 17 and 18. The velocity outputs in Figure 21 are also consistent with the simulated outputs illustrated in Figure 19. Once again, the only difference arises in the repulsion scenario, where in Figure 21.b - and reality - cell velocity drops when they meet the well of cells with no directional bias, containing the far left concentration conditions. When simulating, in Figure 19.b, there is no such boundary as the concentration conditions are provided by fixing the concentration of the edge of the simulated area. This means that cells only see the increase in $\frac{\partial \Omega}{\partial x}$ as $x \to 0$, so no drop in velocity is seen. The accurate recapitulation of the mathematical predictions provides further evidence that the model, up to this point, is a valid explanation of some of the subtleties of cellular migration dynamics.

4.3 Competing Linear Gradients with Partial Agonism

In the process of searching for a chemical that satisfied the properties of a perfectly antagonistsic, non-degradable, competitive inhibitor, the non-degradable analogue of cAMP, Rp-cAMPS, was tested [197]. Rp-cAMPS binds to the cAR1 receptor in *D. discoideum* and is reported to have a K_d approximately two orders of magnitude greater than that of cAMP [196], same as SP-cAMPS. If it were to serve the purpose of a perfect inhibitor, a gradient should be capable of inducing repulsion - relative to a gradient of Sp-cAMPS - while giving no biased directional in isolation. As such, a very important check in order to test that Rp-cAMPS has the desired inhibitor properties is to evaluate the effects of a gradient of Rp-cAMPS by itself. Figure 22 shows the results of one such experiment.

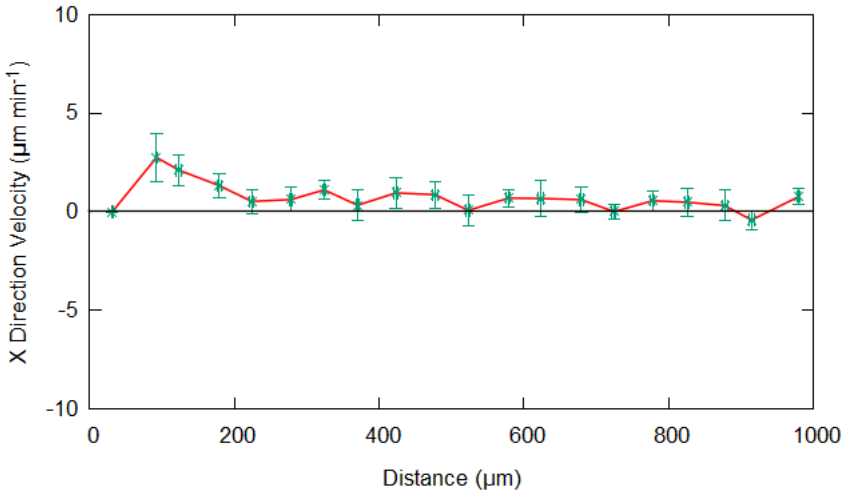

Figure 22: Average experimental cell velocities for times after 18 minutes, when the steady state has approximately been reached, for a $0 - 100\mu M$ gradient Rp-cAMPS, where $L = 1000\mu m$.

In an unexpected twist, it is clear that biased directional cues are present - strongest at start of the gradient and tailing off further up. This is the same kind of velocity profile one would observe from a gradient on non-degradable agonist - as seen in Figure 9.a - albeit with a general reduction in response strength and range. The reduced range of chemotaxis could be explained by a very sharp gradient - meaning that the smaller concentrations, between which the largest changes in Ω occur, are present at the far LHS. The only problem with this argument is that the chemotaxis seen at the beginning of the gradient would be strong, and this is clearly not the case, so there must be an other explanation. Another possibility is that Rp-cAMPS is a partial agonist, such that a small proportion of bound receptors are activated, resulting in diminished chemotaxis. Then, even if if it mostly serves the purposes of an inhibitor, keeping bound receptors in a mostly inactive state, the increasing amounts of activation with concentration, however small, would result in an active receptor gradient of nature $\frac{\partial \Omega}{\partial x} > 0$, giving positive migration. Maths can once again be utilised to give an idea of what kind of behaviour to expect from this system. As it is expected that Rp-cAMPS is mostly an inhibitor all relevant parameters will have a subscript i. The dissociation constant shall be taken to be same as that estimated for Sp-cAMPS, so $K_i = 1\mu M$. While this may be inaccurate it will serve the purpose of ascertaining general key deductions within the system. Upon experimental comparison this parameter can be adjusted as necessary until a satisfactory match in dynamics is found. The active receptor gradient for a gradient of Rp-cAMPS can be found, as usual, using equation (5), giving

$$\Omega(x) = \frac{\frac{\alpha_i C_{1i} x}{K_i L}}{1 + \frac{C_{1i} x}{K_i L}}, \tag{57}$$

resulting in a derivative of the form

$$\frac{\partial \Omega}{\partial x} = \frac{\frac{\alpha_i C_{1i}}{K_i L}}{\left[1 + \frac{C_{1i} x}{K_i L}\right]^2}. \tag{58}$$

Now, fixing $C_{1i} = 100\mu M$ so as to emulate the gradient used in Figure 22, a heat map can be plotted with space on the x-axis and $\frac{\partial \Omega}{\partial x}$ on the z-axis. The parameter α_i can then be varied on the y-axis, allowing the strength and direction of the response at different points in the gradient to be predicted for different levels of receptor activation, as shown in Figure 23.

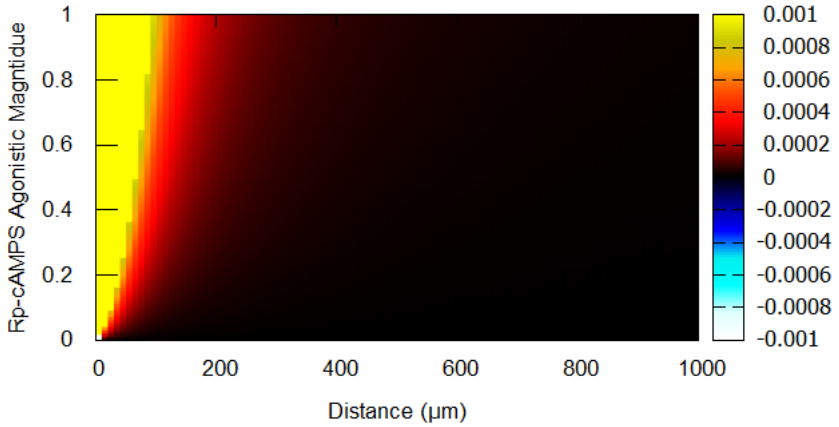

Figure 23: An analytical, chemotactic heat map. Plotted on the y-axis is the intrinsic efficacy of the gradient of imperfect inhibitor ($K_i = 1\mu M$, $C_{0i} = 0\mu M$, $C_{1i} = 100\mu M$) and the x-axis shows variation with space. The overall output indicates expected response strength and direction at different points in space, as the imperfect inhibitor intrinsic efficacy is varied. For additional details on heat map interpretation refer to Figure 4.

It should be noted that although the full range $\alpha_i \in [0, 1]$ has been included, an imperfect inhibitor would be expected to have values very much in the former part of this range. Also note that as $\alpha_i = 1$ implies that Rp-cAMPS would be a full agonist, and a final gradient concentration of $C_{1i} = 100\mu M$ has been used, this horizontal strip of data matches with the $C_{1a} = 100\mu M$ strip of data in Figure 8. No directional cues can be seen when $\alpha_i = 0$, the point at which Rp-cAMPS would serve the purpose of a full inhibitor, as expected. Upon inspection of Figure 23, it seems to be that the velocity output presented in Figure 22 could be recapitulated for values of $\alpha_i \in (0, 0.2)$, where a minute peak in chemotaxis occurs at very small distances before quickly dying out. It shall thus be assumed that RP-cAMPS is a non-degradable partial agonist, or imperfect inhibitor, with very small levels of receptor activation. Of course, it will be impossible to tell if Rp-cAMPS truly has inhibitor properties until is it competed against an agonist, and behaviours indicative of a reduction in receptor activation become apparent.

From section 3.2 there is strong proof that a gradient of agonist with $C_{0a} \neq 0$, inducing

positive migration is isolation, can be combined with an inhibitor gradient, starting from zero concentration, to induce reverse migration. If the inhibitor was imperfect, however, such as has been theorised with Rp-cAMPS, could reverse migration still be induced? If so, this would mean that two gradients giving attractive responses in isolation could, in very unintuitive fashion, be amalgamated to give a repulsive response. As usual this scenario shall first be probed from a mathematical perspective, so, labelling the imperfect inhibitor ($C_{0i} = 0\mu M$, $\alpha_i \neq 0$) with subscript i, and perfect attractant ($C_{0a} \neq 0$, $\alpha_i = 1$) with subscript a, the active receptor gradient can be found, from equation (5), as

$$\Omega(x) = \frac{\frac{1}{K_a}\left\{\left(\frac{C_{1a}-C_{0a}}{L}\right)x + C_{0a}\right\} + \frac{\alpha_i C_{1i} x}{K_i L}}{1 + \frac{1}{K_a}\left\{\left(\frac{C_{1a}-C_{0a}}{L}\right)x + C_{0a}\right\} + \frac{C_{1i}x}{K_i L}}, \tag{59}$$

giving the derivative with respect to space as

$$\frac{\partial \Omega}{\partial x} = \frac{\frac{C_{1a}-C_{0a}}{K_a L} + \frac{\alpha_i C_{1i}}{K_i L} + \frac{C_{1i}C_{0a}(\alpha_i - 1)}{K_a K_i L}}{\left[1 + \frac{1}{K_a}\left\{\left(\frac{C_{1a}-C_{0a}}{L}\right)x + C_{0a}\right\} + \frac{C_{1i}x}{K_i L}\right]^2}. \tag{60}$$

As usual, the denominator being always positive means that the sign of $\frac{\partial \Omega}{\partial x}$, and the direction of motion, depends entirely on the sign of the numerator. This means that repulsion will occur for any configuration which results in the numerator being negative, or

$$\frac{\partial \Omega}{\partial x} < 0 \quad \Leftrightarrow \quad \frac{C_{1a} - C_{0a}}{K_a L} + \frac{\alpha_i C_{1i}}{K_i L} + \frac{C_{1i}C_{0a}(\alpha_i - 1)}{K_a K_i L} < 0. \tag{61}$$

Inequality (61) can now be rearranged to give insight into conditions that will induce chemorepulsion. For this scenario, it is the effect of partial activation of the inhibitor gradient on the induction of reverse migration that is being investigated, so the most sensible parameter to focus on would be the intrinsic efficacy of the inhibitor, α_i. Rearranging (61) in this fashion attains the expression

$$\alpha_i < \frac{K_i L}{C_{1i}\left(1 + \frac{C_{0a}}{K_a}\right)}\left\{\frac{C_{1i}C_{0a}}{K_a K_i L} - \left(\frac{C_{1a} - C_{0a}}{K_a L}\right)\right\} = \alpha_i *\,. \tag{62}$$

The conclusion that can be made from this is that for a gradient of perfect non-degradable agonist with $C_{0a} \neq 0$, giving chemoattraction in isolation, and a gradient of imperfect inhibitor with $C_{0i} = 0\mu M$, also giving chemoattraction in isolation, the combination of these gradients can result in chemorepulsive behaviour as long as the level of activation of the inhibitor satisfies $\alpha_i < \alpha_i*$. Put succinctly, two gradients that attract by themselves can, quite surprisingly, be amalgamated to repulse, at least from a mathematical perspective. Any $\alpha_i > \alpha_i*$ will cause the system to shift into the regime $\frac{\partial \Omega}{\partial x} > 0$, giving exclusively positive migration. When $\alpha_i = \alpha_i*$, the magnitude of the reduction in receptor activation from the antagonistic aspect of the imperfect inhibitor exactly balances the increase in receptor activation seen from both the agonistic aspect of the imperfect inhibitor and the gradient of perfect attractant, giving no net increase or decrease in receptor activation across the gradient and

thus no biased directional cues.

These ideas can be further explored via another heat map which plots $\frac{\partial \Omega}{\partial x}$ from equation (60) on the z-axis. It has been shown that a $2 - 10\mu M$ gradient of perfect attractant, with $K_a = 1\mu M$, gives good attraction in isolation, and can be approximated using Sp-cAMPS, so this shall be the assumed attractant properties. A $0 - 100\mu M$ gradient of imperfect antagonist, with $K_i = 1\mu M$ - illustrated in Figure 23 to also give attraction in isolation - shall be additionally imposed, with its intrinsic efficacy being varied on the y-axis to investigate potential repulsion dynamics. Space, as usual, shall be plotted on the x-axis. Figure 24 shows the corresponding heat map.

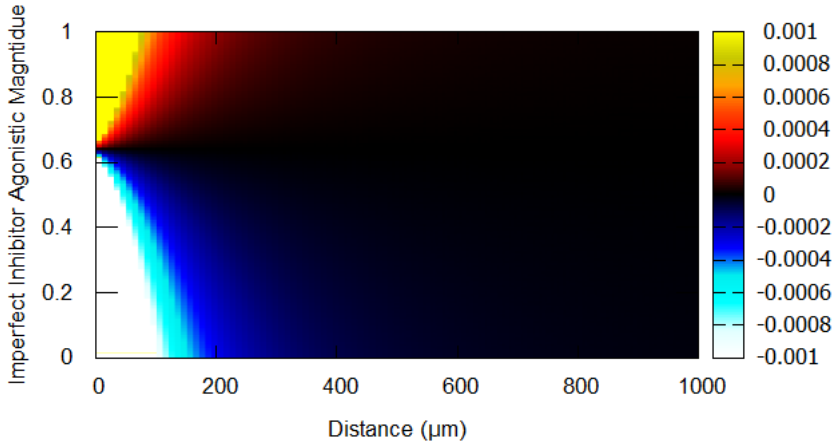

Figure 24: An analytical, chemotactic heat map. Plotted on the y-axis is the intrinsic efficacy of the gradient of imperfect inhibitor ($K_i = 1\mu M$, $C_{0i} = 0\mu M$, $C_{1i} = 100\mu M$) and the x-axis shows variation with space. A $2 - 10\mu M$ gradient of perfect attractant with $K_a = 1\mu M$ has been assumed. The overall output indicates expected response strength and direction at different points in space, as the imperfect inhibitor intrinsic efficacy is varied. For additional details on heat map interpretation refer to Figure 4.

If the parameters implemented in Figure 24 are used to calculate α_i* explicitly, using equation (62), then it can found that $\alpha_i* = 0.64$. Upon inspection of Figure 24 it can be seen that this is the point at which directional cues disappear entirely, confirming the validity of equation (62). It can be further seen that values $\alpha_i > \alpha_i*$ give chemoattraction, and values $\alpha_i < \alpha_i*$ give chemorepulsion, as predicted. Intuitively, as the imperfect inhibitor becomes increasing agonistic, from α_i*, the resultant chemoattraction becomes stronger and functions over more of the spatial range, with the strongest attraction occurring when the imperfect inhibitor has become a perfect attractant, at $\alpha_i = 1$. Similarly, as the imperfect inhibitor becomes decreasingly agonistic, from α_i*, the resultant chemorepulsion increases in intensity, with the most effective repulsion occurring when the imperfect inhibitor becomes a perfect inhibitor, at $\alpha_i* = 0$.

A simulations section shall not be included for this particular scenario. The reason for

this is that it would be, for the very much most part, an almost perfect copy of previous simulation sections, and next to no new insight would be gained. Chemical gradients will diffuse in exactly the same way, to linear equilibria, with active receptor gradients being of an exclusively chemoattractive or chemorepulsive nature for the attractant in isolation or in combination with the inhibitor, respectively. The behavioural profile will change with the evolution in the concentration gradients, and the subsequent impact on receptor binding, until the chemical steady state has been reached. At this point, the peaks in behaviour will be located at the start of the gradient, where the smaller concentrations - between which the largest changes in receptor activation occur - are located. The only difference is that the inhibitor - in isolation - will also give an evolving attractive profile, until chemical equilibrium, at which point the predictions expressed above will hold true. Perhaps the only instructive thing to do is to plot the expected active receptor gradients, in the steady state, for the chemical concentrations that are to be tested experimentally. As all gradients will be linear at equilibrium, this is a simple case of plotting the specific form of equation (12) for each scenario, using equation (5). The concentration configuration illustrated in Figure 24 is what shall be used here, as it implies that satisfactory repulsion should be seen for a large range of α_i - if Rp-cAMPS is indeed a partial agonist - and experiments have shown that individual gradients of Sp-cAMPS and Rp-cAMPS satisfying these concentration conditions give ample chemoattraction. Active receptor gradients shall be presented for the perfect attractant and imperfect inhibitor both alone and together. The same dissociation constants shall also be used and the level of activation of the imperfect inhibitor shall be assumed to be $\alpha_i = 0.2$. Again, while these assumptions may be inaccurate, this maths will be indicative of the type of behaviour one would expect from chemotactic factors with these properties. Upon experimental comparison the accuracy of these parameter assumptions can be evaluated, and an approximation to the true values of these quantities can be made. The closer the maths matches the wet lab work, the closer the parameter regime is to reality. Figure 25 shows the expected active receptor gradients for the concentration configuration which is to be tested via wet lab work.

4.3.1 Experiments

Validating the model is now a simple case of putting *D. discoideum* in an Insall chamber with all three chemical gradient permutations expressed in Figure 25, waiting for the steady state, and testing to see if the cells behave as predicted from each corresponding active receptor gradient. First, however, it should be noted that, as explained in section 3.2.3, there is always a trade off in behaviour when choosing gradients. In summary this means that a very good attractive gradient will detract from the intensity of any repulsion upon superimposing a gradient of competitive inhibitor, and, similarly, the best repulsion is seen when the attractant is a background, which gives no biased cell motion by itself. The chemical configuration that achieves a good balance between positive and reverse migration will see neither at their most intense. On top this, an additional layer of complexity has also been added here in that the gradient of inhibitor, Rp-cAMPS, must also provide some noticeable chemoattraction in

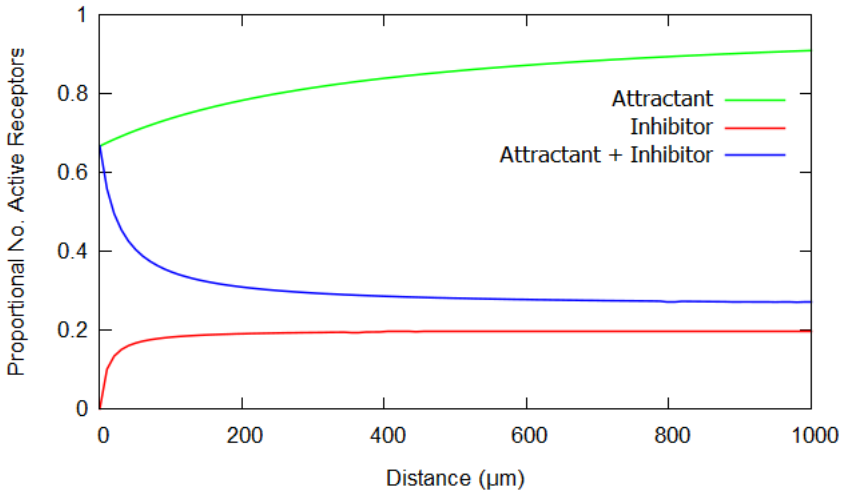

Figure 25: Analytical active receptor gradients, at equilibrium, for a non-degradable attractant ($C_{0a} = 2\mu M$, $C_{1a} = 10\mu M$, $K_a = 1\mu M$, $\alpha_a = 1$), non-degradable inhibitor ($C_{0i} = 0\mu M$, $C_{1i} = 100\mu M$, $K_i = 1\mu M$, $\alpha_i = 0.2$) and for both together.

isolation, with this small level of activation also detracting from any repulsion that may be seen upon interference with the attractant, Sp-cAMPS. This means that the perfect balance will detract even further from the positive migration of Rp-cAMPS and Sp-cAMPS alone, and the reverse migration when they are combined. In other words, overwhelming positive or reverse migration is not expected in any case, and a success would be achieved simply by showing equally weak chemotaxis - in the predicted directions - for all three cases. As a result of this, experiment snapshots shall not be included for this scenario, as overall behavioural output may be unclear from this representation. Only the velocity outputs of each case shall be included, shown in Figure 26.

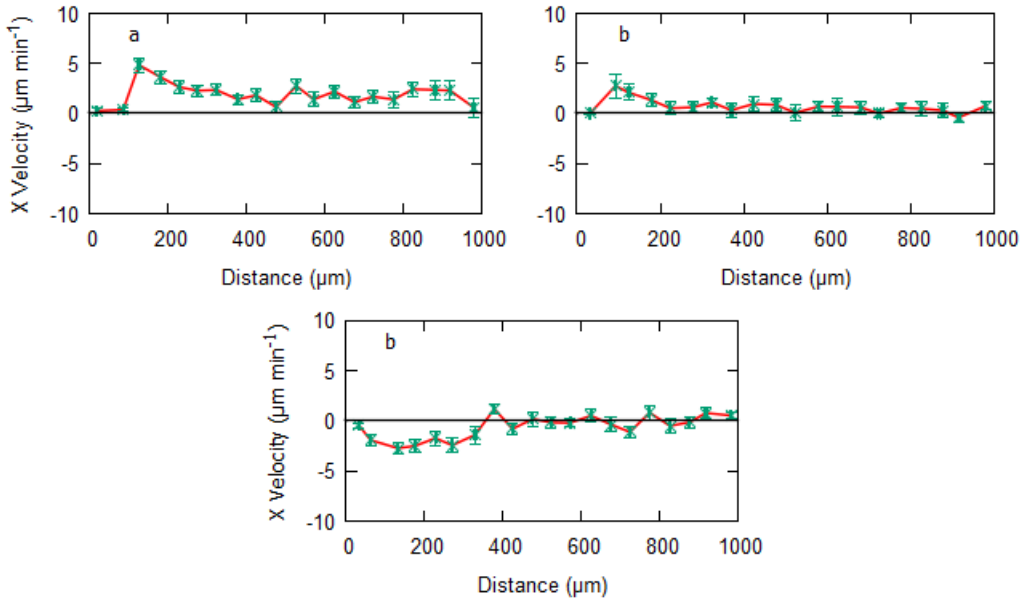

Figure 26: Average experimental cell velocities for times after 18 minutes, when the steady state has approximately been reached, for a) $2 - 10\mu M$ gradient Sp-cAMPS, b) $0 - 100\mu M$ gradient Rp-cAMPS and c) both gradients in combination, where $L = 1000\mu m$.

The predicted behaviour can indeed be seen in all three cases, with the peaks in velocity located the LHS, as expected. The chemotaxis is minimal but consistent, which, considering the complexity of the system, is a success. In conclusion, two gradients that give positive migration alone can combine to induce reverse migration.

5 Exponential Gradient Mechanics

Much insight into cell migration dynamics relative to simple linear gradients has been derived in section 3. The next logical step, from a mathematical point of view, is to consider the effect of non-linear gradients. Without biological context this mathematical evaluation would be nonsensical, but cells are in fact capable of modifying their environment through enzymatic molecular degradation - giving rise to non-linear gradient types. This occurs via localised breakdown, and can be represented mathematically using Michaelis-Menten kinetics. The specifics of the effect of enzymatic degradation on a chemical gradient, using a continuum approximation that assumes cells are packed densely and evenly across the gradient, are detailed in section 2.2. This shows that cellular breakdown in a high concentration limit can give an approximately quadratic type gradient shape, and an exponential type gradient shape can be achieved via cellular breakdown in a low concentration limit. Although these deductions were made analytically and using potentially unrealistic assumptions, they serve the purpose of effectively probing the kinds of non-linearity that may arise via enzymatic degradation. Simulations will be employed when higher levels of accuracy are required. Since biologically relevant non-linear gradient types have been identified, further analytical maths can now be utilised to probe for novel migration mechanics.

5.1 Chemorepulsion with Inhibitor Degradation

In exploring the impact of enzymatic degradation, it is instructive to compare the simple chemorepulsion case, detailed in section 3.1, with a mirror system that replaces the inhibitor with a degradable analogue. The attractant background shall remain unchanged, thus ensuring a consistent, uniform, receptor activating background. Upon changing the breakdown properties of the gradient of inhibitor, a direct comparison can be made between the effects of linear and non-linear gradient types on reverse migration. Once again, denoting the background properties with subscript b and the inhibitor properties with subscript i, it shall be assumed that the non-degradable attractant background is a perfect agonist, $\alpha_b = 1$, and the degradable inhibitor is a perfect antagonist, $\alpha_i = 0$. The form of the attractant background is trivial, $C_b(x) = C_{1b}$, but choosing the chemical gradient form of the degradable inhibitor is more complicated. This is because one of equations (21) or (26) must be chosen, depending on the type on concentration limit one wants to explore. For small concentrations $C << K_m$, equation (21) is appropriate, and, conversely, for large concentrations $C >> K_m$, equation (26) is appropriate. If, in reality, $C \approx K_m$, then the gradient shapes predicted from the analytical mathematics will diverge from their true form, the extent of which is proportional to size of the deviation from the concentration assumption. It is difficult to guess at the value of the key inhibitor parameter K_m, the concentration at which degradation rate is half its maximum value (V_{max}), but, assuming it is around the same magnitude of the dissociation constants that have been seen previously, $\approx 1\mu M$, then the regime that gives a much larger range of concentrations to work with is $C >> K_m$. As such, it is the high concentration approximation - illustrated in equation (26) - that shall be used. This means that, given a

starting inhibitor concentration of $C_{0i} = 0\mu M$, subsequent analytical maths for this section shall assume an inhibitor gradient of the form

$$C_i(x) = Qx^2 + \frac{x}{L}(C_{1i} - QL^2), \tag{63}$$

where

$$Q = \frac{V_{max}}{2D}. \tag{64}$$

Now, the active receptor gradient can be found, once again, by plugging $C_b(x)$ and $C_i(x)$ into equation (5), giving

$$\Omega(x) = \frac{\frac{C_{1b}}{K_b}}{1 + \frac{C_{1b}}{K_b} + \frac{1}{K_i}\left\{Qx^2 + \frac{x}{L}\left(C_{1i} - QL^2\right)\right\}}. \tag{65}$$

The derivative with respect to space can then be found as

$$\frac{\partial \Omega}{\partial x} = -\frac{\frac{C_{1b}}{K_i K_b}\left\{2Qx + \frac{1}{L}(C_{1i} - QL^2)\right\}}{\left[1 + \frac{C_{1b}}{K_b} + \frac{1}{K_i}\left\{Qx^2 + \frac{x}{L}(C_{1i} - QL^2)\right\}\right]^2}, \tag{66}$$

where, just to reiterate, this is a somewhat extraordinary quantity that illustrates both the expected direction and magnitude of the response at different points in space. Now, as the denominator of this relationship is always positive, the sign of $\frac{\partial \Omega}{\partial x}$ is controlled by the sign of the numerator. If the numerator is positive then then the overall expression will be negative, resulting in chemorepulsive directional cues. Conversely, a negative numerator will give chemoattractive directional cues. Before analysing this any further, it is important to bound the value of Q such that the quadratic inhibitor gradient never sees any negative, and impossible, concentration values. This could happen because the high concentration approximation assumes that all concentrations are large enough that it can be assumed that maximal degradation, V_{max}, occurs everywhere. If, in fact, some concentrations are small and do not satisfy this requirement, then the high levels of degradation imposed could cause concentration levels to dip into negative values. A simple solution to avoid this problem is to constrain the value of Q, which contains the degradation term V_{max}, such that all $C_i(x) > 0 \ \ \forall x > 0$. Put mathematically, this requires

$$Qx^2 + \frac{x}{L}(C_{1i} - QL^2) > 0, \tag{67}$$

which, rearranged for Q, attains the condition

$$Q(x) < \frac{C_{1i}}{L(L - x)}. \tag{68}$$

Now this expression gives a bound on the value of Q, for every x, that guarantees $C_i(x) > 0$. As this value is at its smallest at $x = 0$, using this value will also guarantee $C_i(x) > 0 \ \ \forall x >$

0. This critical value of Q shall be called Q^*, where

$$Q^* = \frac{C_{1i}}{L^2} \tag{69}$$

The most informative thing to do now is to insert Q^* into the numerator of equation (66) and see what conditions arise out of forcing this expression to be positive, and for cells to chemorepulse. This gives the expression

$$2\left\{\frac{C_{1i}}{L^2}\right\}x + \frac{1}{L}\left(C_{1i} - \left\{\frac{C_{1i}}{L^2}\right\}L^2\right) > 0 \quad \Rightarrow \quad x > 0. \tag{70}$$

This means that all $Q \leqslant Q^*$ guarantee that equation (66) is negative, cells reverse migrate, and $C_i(x) > 0 \ \forall x > 0$. It is also worth plotting the ratio of equations (66) and (43) for some different values of $Q \leqslant Q^*$ to probe the expected difference in cell response between the linear and non-linear systems. Denoting the non-linear derivative from equation (66) δ_{quad}, and the linear derivative from equation (43) δ_{lin}, for any $\delta_{quad}/\delta_{lin} > 1$ the non-linear system is providing a larger $\frac{\partial \Omega}{\partial x}$, and superior directional cues. Conversely, for any $\delta_{quad}/\delta_{lin} < 1$ the linear system is providing the better response. Figure 27 shows $\delta_{quad}/\delta_{lin}(x)$ for some different $Q \leqslant Q^*$. Note that the final inhibitor concentration $C_{1i} = 200\mu M$ gives $Q^* = 0.0002\ \mu M \mu m^{-2}$.

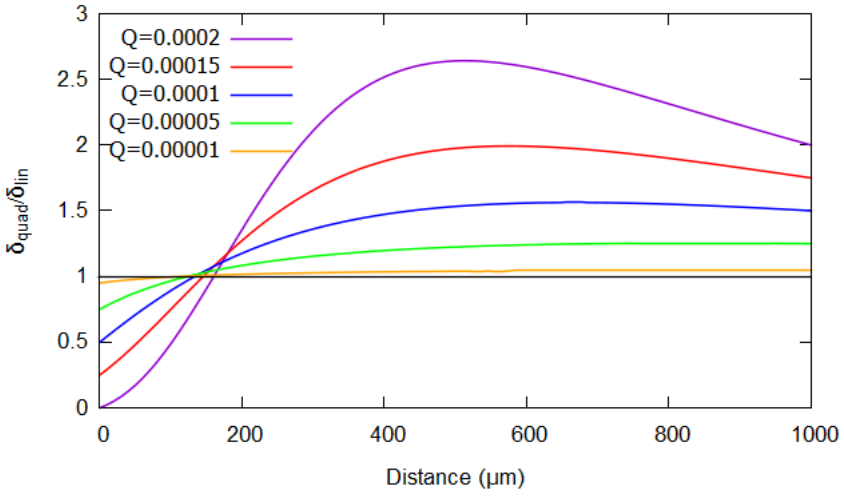

Figure 27: Ratio between $\frac{\partial \Omega}{\partial x}$ for the breakdown and non-breakdown systems, at different values of breakdown parameter Q, when: $C_{1b} = 2\mu M$, $K_b = 1\mu M$, $C_{1i} = 200\mu M$, $K_i = 10\mu M$ and $L = 1000\mu M$.

It is clear that the breakdown system provides superior directional cues over a large portion of the space for all considered values of $Q \leqslant Q^*$. There is also consistently a small region at the former part of the bridge where the linear system provides a better response, meaning that the degradation element, over this small range, actually flattens out the chemical gradient in the breakdown system, before causing a steeper gradient than would be seen in the non-breakdown system. The point at which the response profiles of both regimes intersect

is defined by the line $\frac{\delta_{quad}}{\delta_{lin}} = 1$. Intuitively, larger values of breakdown parameter Q lead to increasingly steep gradients, and better responses. This has the additional effect of flattening out the gradient slightly more, at small distances, such that the linear system is more effective over a slightly increased range. A further development that emerges from Figure 27 is the fact that the effectiveness of the degradation system, relative to the non-degradation system, has a peak. This can be seen most clearly in the curve defined by $Q = 0.0002\ \mu M \mu m^{-2}$, where the non-linear system provides the largest difference in directional cues, compared to the linear system, at $x \approx 500\mu m$, before decreasing in effectiveness as $x \to L$. It should be noted, however, that at no point beyond this peak does the linear system become more effective than the non-linear system, as is seen at small distances. As $Q \to 0$, and the effects of cellular breakdown disappear, the breakdown system tends towards the non-breakdown system, as expected. Now, selecting an appropriate value of Q, equation (66) can be plotted in the familiar heat map representation, and compared to the linear system heat map illustrated in Figure 4.

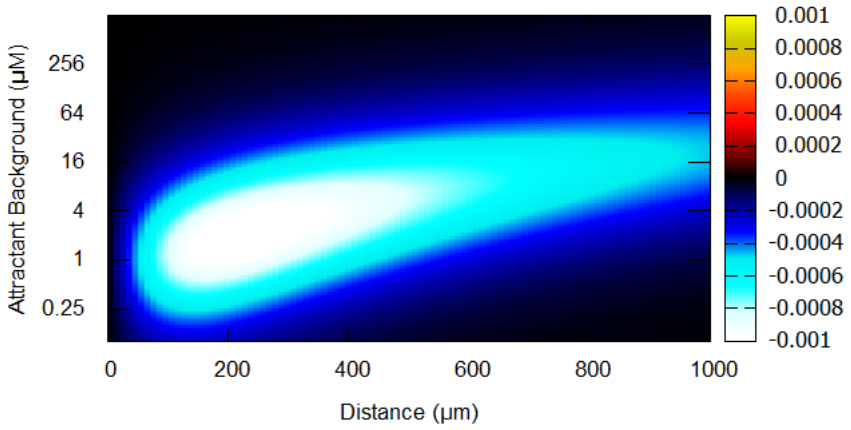

Figure 28: An analytical, chemotactic heat map. Plotted on the y-axis is the concentration of the agonist background ($K_b = 1\mu M$, $\alpha_b = 1$) and the x-axis shows variation with space. A $0 - 200\mu M$ quadratic gradient of degradable antagonist ($K_i = 10\mu M$, $\alpha_i = 0$, $Q = 0.0002\ \mu M \mu m^{-2}$) has been assumed. The overall output indicates expected response strength and direction at different points in space, as the agonist background is varied. For additional details on heat map interpretation refer to Figure 4.

Upon comparing Figures 4 and 28, it can be seen that a similar behavioural profile can be expected from the degradation case, with areas of most intense chemorepulsion generally occurring at smaller distances. Cellular breakdown, however, also leads to higher values of $\frac{\partial \Omega}{\partial x}$ at bigger distances, allowing for more effective chemotaxis over a larger range. In contrast to this, it can also be seen that behaviour at small distances actually seem less reliable than the non-breakdown case, as was hinted at in Figure 27. The better directional cues, rendered in white, occur over a smaller range of the agonist background concentration. It can also be seen that values of $\frac{\partial \Omega}{\partial x}$ do not monotonically decrease as $x \to L$, as was seen every time in the linear system. This behaviour likely arises as a result of the gradient flattening that

occurs at small distances when breakdown is present. In the non-breakdown system, where concentration changed linearly with space, it was guaranteed that largest changes in receptor binding would occur at the smallest concentrations and tail off as concentration increased, as demonstrated in Figure 2.a. This meant that there was no spatially resolved maximum in directional cues. Cells would chemotax most strongly at $x = 0$ and this behaviour would decrease in intensity as $x \to L$. In the breakdown system, however, concentration changes quadratically with space, perhaps meaning that, in a non-linear system, the largest values of $\frac{\partial \Omega}{\partial x}$ do not simply occur at the smallest chemical concentrations. If there is some kind of maximum in $\frac{\partial \Omega}{\partial x}$, with space, that arises as a result of cellular breakdown, then it an be found by maximising equation (66). This can be done by finding the next derivative with respect to space, giving

$$\frac{\partial^2 \Omega}{\partial x^2} = \frac{\frac{2C_{1b}}{K_i K_b}\left\{\frac{3Q^2x^2}{K_i} + \frac{3Qx}{K_i L}(C_{1i} - QL^2) + \frac{1}{K_i L^2}(C_{1i} - QL^2)^2 - Q\left(1 + \frac{C_{1b}}{K_b}\right)\right\}}{\left[1 + \frac{C_{1b}}{K_b} + \frac{1}{K_i}\left\{Qx^2 + \frac{x}{L}(C_{1i} - QL^2)\right\}\right]^3} \tag{71}$$

and setting this to zero. This defines the point which separates regions where $\frac{\partial \Omega}{\partial x}$ is increasing and decreasing, meaning that this is where $\frac{\partial \Omega}{\partial x}$ is at its maximum. Setting to zero and solving for the x-coordinate of the maximum, utilising the quadratic equation, attains

$$x = \frac{-\frac{3Q}{K_i L}(C_{1i} - QL^2) \pm \left[\left\{\frac{3Q}{K_i L}(C_{1i} - QL^2)\right\}^2 - \frac{12Q^2}{K_i}\left\{\frac{1}{K_i L^2}(C_{1i} - QL^2)^2 - Q\left(1 + \frac{C_{1b}}{K_b}\right)\right\}\right]^{\frac{1}{2}}}{\frac{6Q^2}{K_i}}. \tag{72}$$

For any $Q < Q^*$ the lower root is guaranteed to be negative, and unrealistic, so it can be ignored. The upper root, however, may or may not be positive, such that a maximum in $\frac{\partial \Omega}{\partial x}$ may or may not exist. For the case where $Q = Q^*$, the x-coordinate of the maximum can be found via the relationship

$$x = \frac{K_i L^4}{6C_{1i}^2}\left[\frac{12C_{1i}^3}{K_i L^6}\left(1 + \frac{C_{1b}}{K_b}\right)\right]^{\frac{1}{2}}, \tag{73}$$

by plugging equation (69) into equation (72). This means that, when $Q = Q^*$, a maximum in directional cues should be located at $x = 223\mu m$, for a system with parameters: $C_{1b} = 2\mu M$, $K_b = 1\mu M$, $C_{1i} = 200\mu M$, $K_i = 10\mu M$ and $L = 1000\mu m$ ($Q^* = 0.0002\ \mu M \mu m^{-2}$). The easiest way to test the validity of this statement would be to plot the curve $\frac{\partial \Omega}{\partial x}$ vs x, for the parameters just mentioned, when $Q = Q^*$, and identify where the peak is. Figure 29 shall illustrate this alongside curves for some other $Q < Q^*$, for completeness.

As expected, the peak in $\frac{\partial \Omega}{\partial x}$, when $Q = Q^* = 0.0002\ \mu M \mu m^{-2}$, is located at $x = 223\mu m$. Additionally, it can be seen that a further peak in directional cues can only seen for $Q = 0.00015\ \mu M \mu m^{-2}$. For all Q below this value there is no peak, only monotonic decrease in $\frac{\partial \Omega}{\partial x}$, as was seen in the linear system. This means that there is some lower bound on Q, below which the gradient flattening is not pronounced enough to give a peak in directional

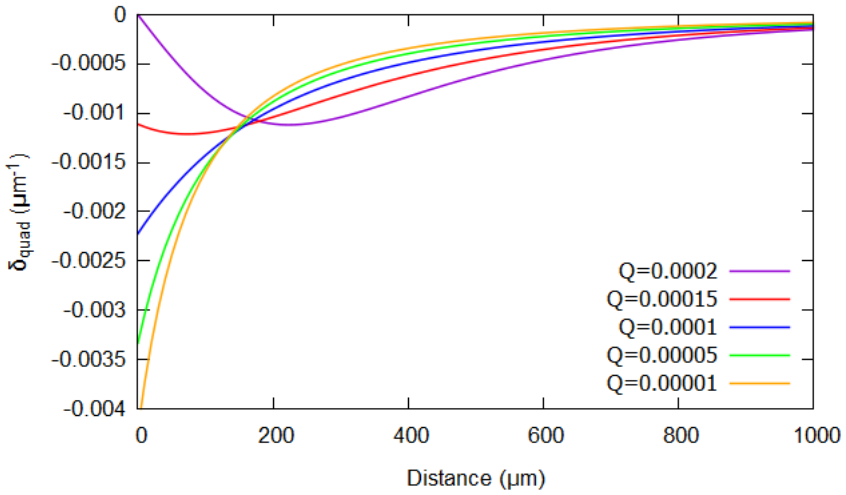

Figure 29: $\frac{\partial \Omega}{\partial x}$ with x at different values of breakdown parameter Q, when: $C_{1b} = 2\mu M$, $K_b = 1\mu M$, $C_{1i} = 200\mu M$, $K_i = 10\mu M$ and $L = 1000\mu M$.

cues. This specific value of Q could be found by setting equation (72) to zero and solving for Q, however, this would involve more algebraically heavy maths for relatively little gain. A much simpler way would be to plot the upper root in equation (72) with Q, such that the x-axis intercept gives the desired value of Q. Figure 30 demonstrates such a plot.

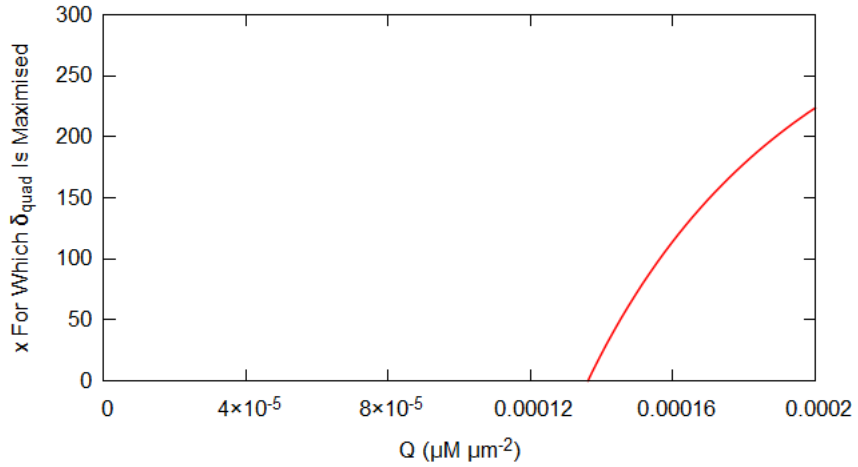

Fi

Figure 30: X-coordinate of maximum in $\frac{\partial \Omega}{\partial x}$ when: $C_{1b} = 2\mu M$, $K_b = 1\mu M$, $C_{1i} = 200\mu M$, $K_i = 10\mu M$ and $L = 1000\mu M$.

Upon inspecting Figure 30 it can be seen that the maximum at $x = 223\mu m$ has been recovered when $Q = 0.0002\ \mu M \mu m^{-2}$, as expected, and that a peak in directional cues ceases to exist for $Q \lessapprox 0.00014\ \mu M \mu m^{-2}$. The peak when $Q = 0.00015$ is located at $x \approx 50\mu m$, which can be confirmed via Figure 29 and equation (72).

Clearly, there are still larger changes in receptor binding between smaller concentrations, but the rate of concentration increase with space also plays an important role. In the case of linear increase, the largest change will always occur at smallest concentration, but in

the case of non-linear increase, where much smaller values of $\frac{\partial C}{\partial x}$ can be expected at small distances, increasing with space, the maximum in $\frac{\partial \Omega}{\partial x}$ can shift to the point where the rate of concentration increase is optimum relative to the size of the concentration at that point. Most interestingly, the statement that the strongest directional cues occur at $C \approx K_d$ concentrations, which was disproved in section 2.3.1, actually becomes somewhat relevant here. With $K_i = 10\mu M$ and $C_{1i} = 200\mu M$, it can be expected that K_i is located somewhere around $x = 50\mu m$, which, when $Q = 0.00015\ \mu M \mu m^{-2}$, is in a similar region to the maximum in $\frac{\partial \Omega}{\partial x}$. This means that, when cellular degradation is accounted for, it is possible for the maximum in directional cues to coincide with the $C \approx K_d$ concentrations. This would be a coincidence, however, as any peak in directional cues is dependent upon gradient shape, and, ultimately, enzymatic degradation. If cellular degradation were not accounted for, it is understandable how such a misconception surrounding response strengths and dissociation constant could arise.

5.1.1 Simulations

The next logical step, as before, is to test the dynamics of the degrading system using numerical mathematics. In section 3 the main advantage in using numerics was probing behaviour at early times, as the analytical maths utilised here always assumes a time independent steady state that, in general, is representative of moderate amounts of time elapsing. This is still true here, however, there is an additional benefit in that the approximations that degradation is occurring across all spatial points and concentrations are strictly in the regime $C >> K_m$ can be avoided. The continuum degradation approximation naturally disappears as the simulation models each cell in a discrete fashion, detracting from the concentration of grid points in their area of influence. There is also no need to make a concentration assumption as cells can degrade according to full Michaelis-Menten kinetics by utilising the fourth order Runge-Kutta technique. The goal here is employ precise simulations, using the general analysis in the previous section as a guide, to both build upon and verify the deductions made using the analytical maths. In doing so there is the potential to identify any regions where the analytical assumptions break down. Upon running one such simulation, the first point of interest is the evolution in time of both the degradable inhibitor gradient profile and overall active receptor gradient, as illustrated in Figure 31. The background of non-degradable agonist shall be omitted as it remains constant throughout the simulation.

As expected, the degradable inhibitor tends towards a non-linear steady state, with the corresponding active receptor gradients giving purely reverse migratory directional cues. Upon comparison with Figure 5, the same system but without inhibitor degradation mechanics, it can be seen that the active receptor gradient is, in general, steeper over a larger range, giving more robust chemotaxis. The strongest directional cues, where the active receptor gradient is most sharp, clearly does not occur purely at the lowest concentration, in contrast to the linear case. This discrepancy in behaviour was predicted from the analytical mathematics sections, and adds further validity to the theory that the largest changes in receptor binding,

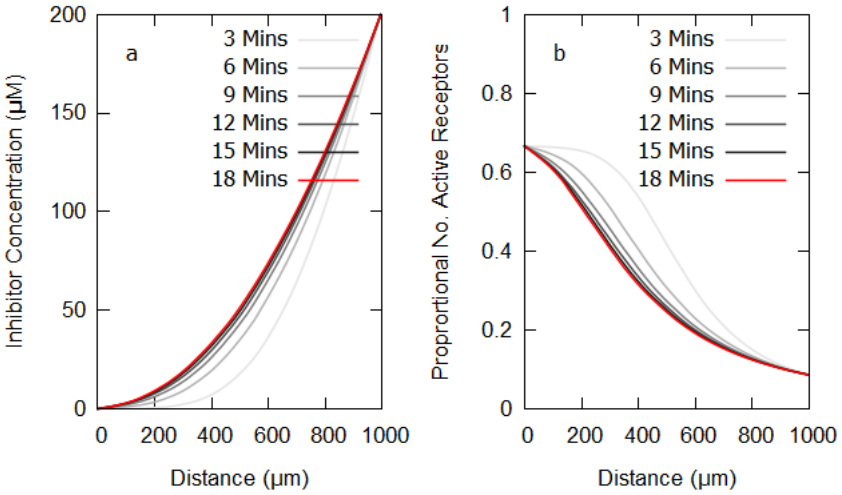

Figure 31: a) Simulated degradable inhibitor diffusing to non-linear equilibrium and b) corresponding temporal effect on the active receptor gradient when: $C_{1b} = 2\mu M$, $K_b = 1\mu M$, $C_{1i} = 200\mu M$, $K_i = 10\mu M$, $D = 20000\mu m^2 min^{-1}$, $K_m = 2\mu M$, $V_{max} = 1000\mu M min^{-1}$ and $L = 1000\mu m$

and most intense chemotaxis, occurs when the lowest concentrations are optimum relative to $\frac{\partial C}{\partial x}$, the rate of change of concentration with space. A hugely insightful comparison that can be made here is with the analytically predicted inhibitor gradient shapes, and resultant active receptor gradients, for different values of Q, shown in Figure 32.

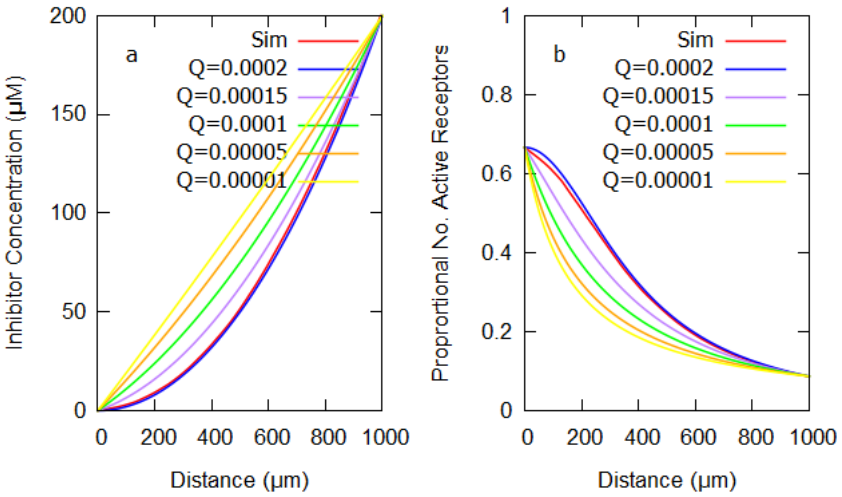

Figure 32: a) Analytical inhibitor equilibrium, in $C >> K_m$ limit, for different values of degradation parameter Q and b) corresponding active receptor gradients when: $C_{1b} = 2\mu M$, $K_b = 1\mu M$, $C_{1i} = 200\mu M$, $K_i = 10\mu M$ and $L = 1000\mu m$.

The blue curves, corresponding to $Q = 0.0002\ \mu M \mu m^{-2}$, match very well with the simulated equilibrium gradients, shown in red. This suggests not only that the high concentration approximation was an accurate assumption for this case, but also that the continuum analytical degradation parameter $Q = 0.0002\ \mu M \mu m^{-2}$ is approximately equivalent to a discrete numerical system where $V_{max} = 1000\mu M min^{-1}$, $D = 20000\mu m^2 min^{-1}$ and $K_m = 2\mu M$,

when $C_{1i} = 200\mu M$. This equivalence means that the location of the maximum in directional cues derived in equation (73), when $Q = Q^* = 0.0002\ \mu M\mu m^{-2}$, should be applicable to this simulation. One thing that should be made clear here is the discrepancy between the analytical Q value ($Q = 0.0002\ \mu M\mu m^{-2}$) and the Q value for this simulation ($Q = 0.025\ \mu M\mu m^{-2}$), as similar effects seem to have been achieved with degradation parameters that are different by about two orders of magnitude. The reasoning behind this is that the analytical maths assumes that cells are essentially densely packed over the whole space and do not move, resulting in a continuum degradation effect that consistently affects each point in space, whereas in the simulation the cells are distributed in a much sparser fashion and change location according to chemical cues. This means that identical Q values would result in a much more pronounced effect in the analytical scenario as more cells would be influencing the gradient shape, thus warping the chemical gradient to a greater degree than would be seen from a simulation in which, comparatively, sparsely populated cells employ the same degradation rates. In order for similar effects to be seen between a discrete simulation and an analytic continuum, the simulation must use greater degradation parameters. A final thing to be clarified in Figure 31 is that records of concentration and receptor activation are averaged over the y-axis in the 2D simulation, giving a 1D representation purely in the x-axis; this means that the sharp gradient micro environments that surround each cell due to localised degradation are similarly averaged out. Although this eliminates any representation of the discrete cellular mechanics at play, it gives an insightful overview of the system that allows easy comparison with both the analytical elements of thesis, which generally employ continuum mechanics, and simulations that include enzymatic degradation. A snapshot of the simulation, however, rendered in terms of $\frac{\partial \Omega}{\partial x}$, allows one to gauge the local impact of individual cells on the chemical environment. One such snapshot is demonstrated in Figure 33.

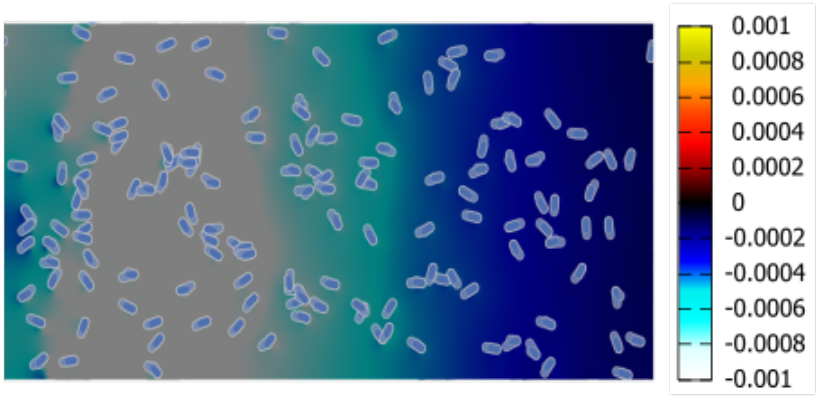

Figure 33: Simulation snapshot after 18 minutes, when the steady state has approximately been reached, for: $C_{1b} = 2\mu M$, $K_b = 1\mu M$, $C_{1i} = 200\mu M$, $K_i = 10\mu M$, $D = 20000\mu m^2 min^{-1}$, $K_m = 2\mu M$, $V_{max} = 1000\mu M min^{-1}$ and $L = 1000\mu m$.

Perturbations in receptor activation, due to localised cellular breakdown, can be seen clearly

in this Figure. It is worth comparing this with Figure 6, the non degradation system, where concentration, and receptor activation, vary only in the x direction, according to the 1D diffusion equation. One particularly fascinating feature in the breakdown system is that the cells gain not just the ability to influence the environment, but also each other. In the absence of breakdown, the chemical environment changes purely according to diffusion, such that this is also the primary factor dictating cell migration, however, when enzymatic breakdown is accounted for, cells also gain a certain measure of exertion on the chemical environment. This means that chemical concentration, and cell migration, is affected by both diffusion and the cells themselves. The obvious implication here is that cells gain the ability to modulate their own chemotaxis, but upon further consideration it is also apparent that the cells must be modulating each others' chemotaxis as well. For the system being considered here this dynamic has a additional special effect. As inhibitor generally causes an overall reduction in receptor activation, the fact that each cell is degrading it will result in a slight, localised, increase in receptor activation. This essentially means that each cell becomes a tiny peak in receptor activation, which can attract further cells. If multiple cells were to be drawn together then the effects of breakdown would stack, resulting in an even larger peak in receptor activation with a greater capacity to draw in cells. Obviously this effect is dominated by the overall repulsive bias resulting from the imposed inhibitor gradient, such that a huge clump of cells does not arise, however, it does mean that the cells are communicating and being drawn to each other as they migrate. Visually, this effect can be seen at the far left of Figure 33, where a dark blue patch represents the peak in receptor activation resulting from multiple cells breaking down the inhibitor, drawing in more cells. Also note that the peak in directional cues can be approximately read off of Figure 33, at about $x = 200\mu m$, and matches closely with the maximum calculated from equation (73), as predicted from the similarities between the analytical and simulated inhibitor equilibrium state, when $Q = Q^* = 0.0002\ \mu M \mu m^{-2}$. Finally, it is worth extracting a velocity output of cells in the simulation, for times after the the equilibrium state has approximately been reached. This will allow for an effective comparison with experimental work and ultimately give insight into the accuracy of both the parameters used and the model itself. Figure 34 shows this plot.

5.1.2 Experiments

Once again, it is vital to validate the model that has been built thus far via wet lab work, allowing greater levels of complexity to be investigated mathematically without worry of biological irrelevance. As usual, the NC4 strain of *D. discoideum* shall be used in an Insall chamber. If chemicals can be found that mirror the properties explored in the maths, and the behavioural output matches the predictions presented in previous sections, then it can be said with reasonable confidence that the model, up to this point, is sound. As usual, the background of non-degradable agonist can be supplied by using Sp-cAMPS. The gradient of degradable inhibitor is a bit trickier, but 8-CPT-cAMP was speculated to be a candidate in section 3.1.3 due to its "chemorepellent" effects [50]. It was suggested that *D. discoideum* cAMP secretion was not accounted for in this paper, potentially giving rise to an unexpected

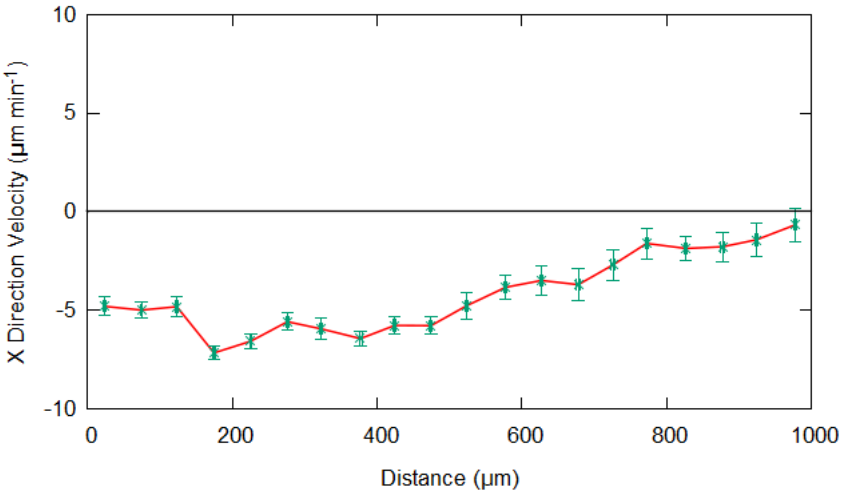

Figure 34: Average simulated velocity output for times after 18 minutes, when the steady state has approximately been reached, for: $C_{1b} = 2\mu M$, $K_b = 1\mu M$, $C_{1i} = 200\mu M$, $K_i = 10\mu M$, $D = 20000\mu m^2 min^{-1}$, $K_m = 2\mu M$, $V_{max} = 1000\mu M min^{-1}$ and $L = 1000\mu m$.

background of agonist - of which a gradient of 8-CPT-cAMP, if it served the function of an antagonist, would provide the observed repulsion. A quick and imperative control is that of a gradient of 8-CPT-cAMP with cAMP secretion blocked via caffeine, illustrated in Figure 35.

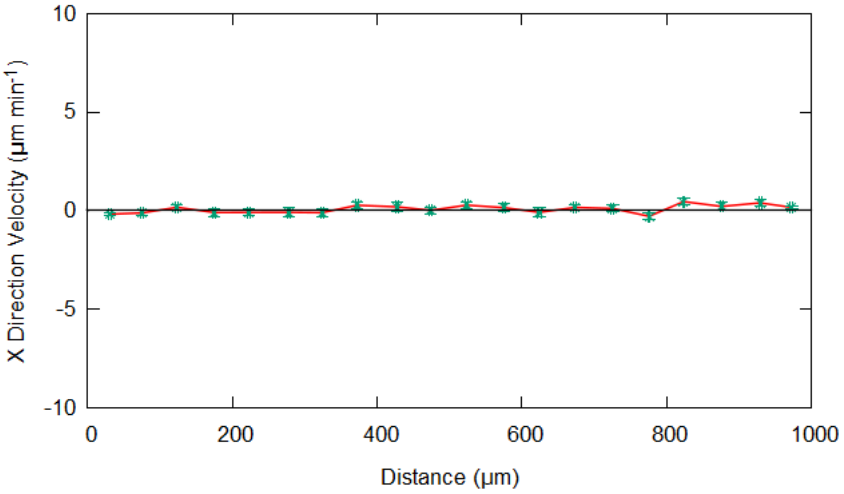

Figure 35: Measured cell velocities, at equilibrium, for $0 - 200\mu M$ gradient 8-CPT-cAMP.

It is clear that in the absence of an agonist there is no biased response, so it makes sense that 8-CPT-cAMP serves the function of an antagonist. It is difficult to make the key deduction of whether or not 8-CPT-cAMP is degradable, but as long as the response is substantially more effective - over a larger range - as predicted from the maths, than the Sp-8-CPT-cAMPS scenario, then it can be said with reasonable surety that degradation mechanics are at play for 8-CPT-cAMP. This would also further reinforce the hypothesis that Sp-8-CPT-cAMPS is phosphodiesterase resistant, giving rise to linear gradients and reduced chemotaxis. The best thing to do now is to recapitulate the chemical conditions illustrated in the simulations section, using Sp-cAMPS as the non-degradable agonist background and 8-CPT-cAMP as

the degradable antagonist gradient, and measure the cell response. A snapshot and average velocity output, in the steady state, are presented in Figures 36 and 37, respectively.

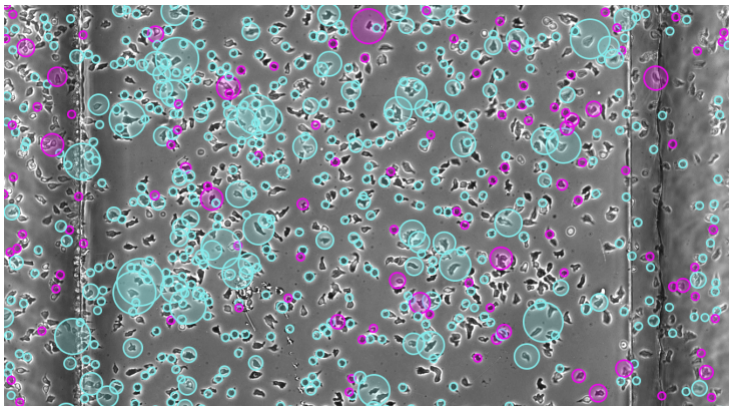

Figure 36: Experiment snapshot, at equilibrium, of NC4 strain of *D. discoideum* subject to a $2\mu M$ background Sp-cAMPS and a $0 - 200\mu M$ gradient of 8-CPT-cAMP. Cyan circles correspond to motion to the LHS (chemorepulsion) and magenta circles correspond to motion to the RHS (chemoattraction), with the size of the circle giving the magnitude of the x direction velocity.

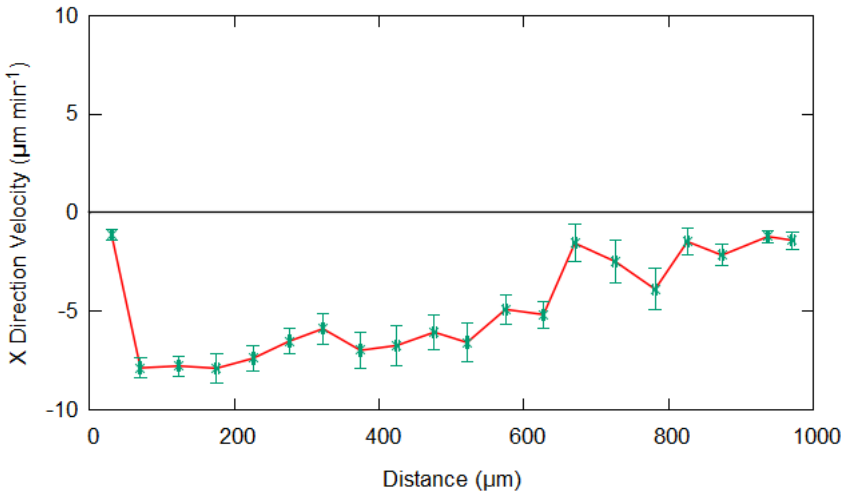

Figure 37: Measured average cell velocities, at equilibrium, of NC4 strain of *D. discoideum discoideum* subject to a $2\mu M$ background Sp-cAMPS and a $0 - 200\mu M$ gradient 8-CPT-cAMP.

Figure 36 shows a very strong reverse migratory bias, illustrated with cyan circles, that is strongest around the start of the gradient and tails off with distance. This is further reinforced with the velocity output in Figure 37. In comparison with the snapshot and velocity output of the Sp-8-CPT-cAMPS scenario, demonstrated in Figures 11 and 12, it is clear that the reverse migration is both more intense and acts over an increased range. This suggests that 8-CPT-cAMP is not only a competitive inhibitor, but also induces the increased chemotactic prowess associated with enzymatic degradation. This assumption is further strengthened by the profound similarity between the mathematical predictions surrounding a degradable inhibitor and the experimental output presented, particularly the comparison between the

simulated velocity output shown in Figure 34 and the output given in Figure 37. The only differences that really arise here are that, in real life, the response seems to be stronger, insinuating that slightly stronger degradation parameters may be closer to reality, and there is a sharper decrease in directional cues close to $x = 0$. This, however, can once again be accounted for by the solid boundary encountered at $x = 0$ in an Insall chamber, which does not exist in simulation space. This means that "cells" in the simulation experience only the strong directional cues seen at low concentrations, whereas the cells in the Insall chamber hit a wall in this same area. Overall it can be concluded that the model is sound, 8-CPT-cAMP is likely a degradable antagonist, and the parameters utilised in the mathematics are probably of the same order of magnitude as reality.

5.2 Complex Degradable Inhibitor Dynamics

If cellular degradation mechanics can lead to a peak in directional cues, which strictly cannot exist if degradation is not accounted for, then perhaps breakdown can give rise to even more intriguing and complex behaviours. In section 3.2 it was shown, mathematically, that there was a critical final inhibitor concentration, $C_{1i}*$, when a gradient of agonist is competed against a gradient of competitive inhibitor, that ultimately dictates the global directional regime. For concentrations above this value the rate of decrease in receptor activation from the antagonist is larger than the rate of increase seen from the attractant, resulting in reverse migration. Conversely, for concentrations below this value, the rate of receptor activation decrease from the inhibitor is less than the rate of increase from the attractant, resulting in reduced positive migration. This concept is summarised in equation (55), where this critical final inhibitor concentration - above which reverse migration occurs - is expressed. Note, once again, that it has been assumed that the inhibitor gradient starts from zero concentration, and that the attractant gradient start from a non-zero value, guaranteeing non-zero receptor activation at the beginning of the gradient. Now, as it is discrepancies between gradient types that are the point of interest here, it is insightful to rearrange equation (55) in terms of chemical gradient steepness, instead of final gradient concentration. In the case of these linear gradients, the steepness, M, can be found trivially as

$$M = \frac{\partial C}{\partial x} = \frac{C_1 - C_0}{L}, \tag{74}$$

where, as usual, attractant properties will be labelled with subscript a, and inhibitor properties will be labelled with subscript i. Equation (55) can now be rearranged in the form

$$\frac{\partial \Omega}{\partial x} < 0 \quad \Leftrightarrow \quad \frac{M_i}{M_a} > \frac{K_i}{C_{0a}}. \tag{75}$$

This expression is very informative, as it states that the ratio between the steepness of the inhibitor and attractant gradients must be above $\frac{K_i}{C_{0a}}$ in order to induce reverse migration. The key point here is that, for a linear regime, the values of M_i and M_a, and so the ratio $\frac{M_i}{M_a}$, are constant at all points in space. This means that if this ratio is above or below $\frac{K_i}{C_{0a}}$, then

the system will always be in a chemorepulsive or chemoattractive regime, respectively. Now consider this same system with inhibitor degradation, in the limit $C >> K_m$, resulting in a non-linear gradient shape. Referring to equation (26), the steepness of the inhibitor gradient can be found similarly as

$$M = \frac{\partial C}{\partial x} = 2Qx + \frac{1}{L}(C_{1i} - QL^2). \tag{76}$$

It can be seen clearly here that the gradient steepness now varies with space, meaning that the ratio $\frac{M_i}{M_a}$ will now also vary with space. This means that the critical ratio could exist partway along the gradient, resulting in conflicting directional regimes above and below this point. In other words, enzymatic degradation could be the key to achieving a spatially resolved turning point in cell directional cues.

From a qualitative perspective, if a gradient of non-degradable agonist is competed against a gradient of degradable antagonist, very low rates of change of inhibitor concentration at small distances should give rise to a small value of $\frac{M_i}{M_a}$, and positive migration, whereas the larger rates of change in inhibitor concentration at larger distances should give a high value of $\frac{M_i}{M_a}$, and reverse migration. This theory can, as usual, be probed explicitly by plugging gradient forms for a linear gradient of a attractant and non-linear gradient of inhibitor into equation (5), allowing analysis of the corresponding active receptor gradient for this system. Due to the complexity of the system, the immediate simplification of $C_{0a} = C_{0i} = 0\mu M$ shall be applied, giving both an attractant and inhibitor gradient that start from zero concentration. Additionally it shall also be assumed that the attractant and inhibitor are a perfect agonist and antagonist, respectively, such that $\alpha_a = 1$ and $\alpha_i = 0$. For the same reasons stated in section 4.1, the limit $C >> K_m$ shall be assumed for the inhibitor gradient, meaning it shall have the same form stated in equation (63). The linear attractant form can be deduced trivially from equation (12). Plugging all of this information into equation (5) gives

$$\Omega(x) = \frac{\frac{1}{K_a}\left\{\frac{C_{1a}x}{L}\right\}}{1 + \frac{1}{K_a}\left\{\frac{C_{1a}x}{L}\right\} + \frac{1}{K_i}\left\{Qx^2 + \frac{x}{L}\left(C_{1i} - QL^2\right)\right\}}, \tag{77}$$

meaning the derivative with respect to space can be found as

$$\frac{\partial \Omega}{\partial x} = \frac{\frac{C_{1a}}{K_a L}\left\{1 - \frac{Qx^2}{K_i}\right\}}{\left[1 + \frac{1}{K_a}\left\{\frac{C_{1a}x}{L}\right\} + \frac{1}{K_i}\left\{Qx^2 + \frac{x}{L}\left(C_{1i} - QL^2\right)\right\}\right]^2}. \tag{78}$$

As described in section 4.1, it shall always be assumed that $Q \leq Q^* = \frac{C_{1i}}{L^2}$, such that $C_i(x) > 0$ always. For relevant values of Q, the point at which $\frac{\partial \Omega}{\partial x} = 0$ separates the chemoattractive and chemorepulsive regimes, where $\frac{\partial \Omega}{\partial x} > 0$ and $\frac{\partial \Omega}{\partial x} < 0$, respectively. This means that setting equation (78) to zero will attain information about the theorised turning point in cell directional bias. Doing so and solving for the critical spatial coordinate, x^*,

gives

$$x^* = \sqrt{\frac{K_i}{Q}} \tag{79}$$

as the location of the turning point. For any $x < x^*$ there will be $\frac{\partial \Omega}{\partial x} > 0$, giving positive migration, and for any $x > x^*$ there will be $\frac{\partial \Omega}{\partial x} < 0$, giving reverse migration. Further information can be derived by considering the special case when $Q = Q^*$, and plugging equation (69) into equation (79), giving

$$x^* = \sqrt{\frac{K_i L^2}{C_{1i}}}. \tag{80}$$

This implies that high vales of the final inhibitor concentration, C_{1i}, will push the turning point to smaller distances, causing chemorepulsion to become more prevalent. Conversely, smaller inhibitor concentrations will give rise to more widespread chemoattraction. A further, and very important, deduction that can be made from equation (80) is that properties of the attractant gradient play absolutely no role in the location of the turning point.

A heap map plotting equation (78) in 3D will, once again, be an informative visualisation of these concepts by showing, graphically, both the direction and magnitude of the expected cell motion relative to space and one other chosen variable. The obvious variable to plot would be the final inhibitor concentration, C_{1i}, where a changing region separating hot and cold colors, representing the turning point in directional cues, would be fantastic validation. An issue arises here, however, in that only one value of the degradation parameter, Q, can be chosen. This means that if C_{1i} is varied on the y-axis, it is likely that the rule $Q \leq Q^*$, which guarantees non-negative values of inhibitor concentration across the gradient, will be violated at some point, as Q^* is dependent on C_{1i}. This means that values of C_{1i} and Q, satisfying $Q \leq Q^*$, must allocated first, and some other parameter must be varied on the y-axis of the heat map. If it is assumed that $Q = Q^*$ then equation (80) gives, for the standard final inhibitor concentration of $C_{1i} = 200\mu M$ seen in previous sections, a turning point at $x = 223\mu m$. If a more central turning point is desired, then a smaller value of of C_{1i} must be chosen, thus forcing the turning point to larger distances. The concentration $C_{1i} = 80\mu M$ will be selected as a compromise between trying to force the turning point as far up the gradient as possible while still maintaining the limit $C >> K_m$. The corresponding maximum possible degradation parameter, $Q = 0.00008\ \mu M \mu m^{-2}$, shall also be chosen. It is important to note here that the value $Q = 0.0002\ \mu M \mu m^{-2}$, corresponding to $V_{max} = 8\mu M min^{-1}$ when $D = 20000\mu m^2 min^{-1}$, was the analytical degradation parameter that gave closet correlation to the discrete numerical analysis in the previous section, and, by extension, because the simulations and experiments matched so closely, reality. This smaller value of Q corresponds to a smaller value of V_{max}, and will likely cause the equivalence observed between the analytical, numerical and physical systems to disappear. This means that the goal here is not to find an analytical regime that recapitulates reality, and can be used

to accurately predict behavioural profiles in different parameter regimes, but to simply give insight into overall behaviours and trends. Now, the only other parameter that influences the turning point and the direction of motion, according to equation (80), is the inhibitor dissociation constant, K_i. As such this is what shall be plotted on the y-axis of the heat map, which is demonstrated in Figure 38.

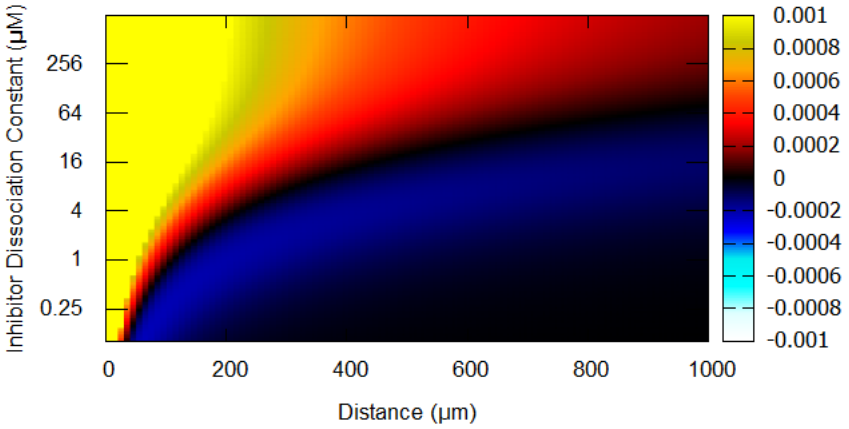

Figure 38: An analytical, chemotactic heat map. Plotted on the y-axis is the inhibitor dissociation constant ($Q = 0.00008\ \mu M \mu m^{-2}$, $C_{1i} = 80\mu M$, $\alpha_i = 0$) and the x-axis shows variation with space. A linear gradient of agonist ($K_a = 1\mu M$, $C_{1a} = 2\mu M$, $\alpha_a = 1$) has been assumed. The overall output indicates expected response strength and direction at different points in space, as the agonist background is varied. For additional details on heat map interpretation refer to Figure 4.

Illustrated beautifully here is a spatially resolved turning point in cell directional cues, the location of which is modulated via properties of a degradable competitive inhibitor. Note that the nature of this system will cause the cells to converge at the turning point.

5.2.1 Simulations

As before, numerical maths shall now be employed to investigate the kinds of behaviour that may arise at early times, and when the analytical approximations of continuum degradation and high concentration are bypassed. In doing so, further insight into the system can be gained as well as a gauge as to the validity of the analytical model, and the impact of the analytical assumptions on predictions of cell dynamics. Figure 39 provides chemical concentrations at approximate equilibrium and the evolution of the active receptor gradient, for a simulation utilising the same chemical configuration as Figure 38, with $K_i = 10\mu M$, and the same degradation parameters used in the simulations of section 4.1, which recapitulated reality to a suitably accurate degree.

It is clear that the non-degradable agonist and degradable antagonist have linear and non-linear profiles at equilibrium, respectively, and that this type of chemical regime results gives

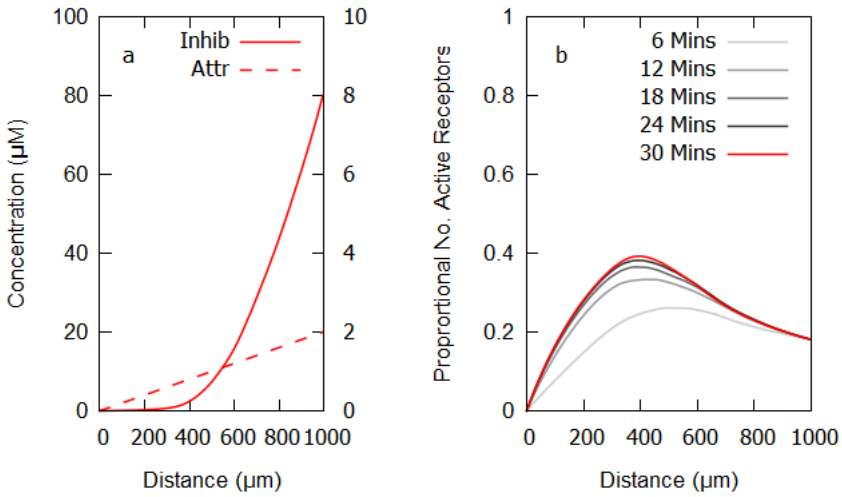

Figure 39: a) Simulated steady state concentrations (times after 30 mins) and b) temporal effect on the active receptor gradient when: $C_{1a} = 2\mu M$, $K_a = 1\mu M$, $C_{1i} = 80\mu M$, $K_i = 10\mu M$, $D = 20000\mu m^2 min^{-1}$, $K_m = 2\mu M$, $V_{max} = 1000\mu M min^{-1}$ and $L = 1000\mu m$.

rise to an active receptor gradient that provides conflicting directional cues, either side of a turning point, at each temporal coordinate. The turning point seems to drift towards smaller distances, with time, before stabilising at around $x = 400\mu m$. The analytical maths presented in Figure 38, where the turning point can be read off of the heat map on the horizontal strip corresponding to $K_i = 10\mu M$, has a turning point location at around $x = 300\mu m$. As mentioned just previously, this discrepancy is likely due to the difference in inhibitor gradient shape caused by the lack of equivalence between the continuum analytical degradation parameter $Q = 0.00008\ \mu M\mu m^{-2}$ and discrete numerical degradation parameters $K_m = 2\mu M$ and $V_{max} = 1000\ \mu M min^{-1}$. Additionally, as smaller concentrations are being utilised in this section, it is possible that the discrepancy is also representative of the assumption $C >> K_m$ beginning to fail, causing further differences between the inhibitor gradient shape in the analytical limit and when full Michaelis-Menten is accounted for. This can be further investigated by plotting the expected analytical inhibitor gradient shape, and subsequent active receptor gradient, for different values of degradation parameter Q. This is demonstrated in Figure 40.

It is clear that the sharpest possible analytical gradient, the blue curve with $Q = Q^* = 0.00008\ \mu M\mu m^{-2}$, still falls considerably short of the simulated inhibitor gradient seen in Figure 39. While the desired turning point in cell response direction is still achieved, the analytical gradient of inhibitor is clearly less flat at small distances and less sharp at larger distances, resulting in an active receptor gradient that has both a shifted turning point and is less steep, in general. This is proof that the $C >> K_m$ limit is just barely appropriate when $C_{1i} = 80\mu M$ and $K_m = 2\mu M$, although it still replicates global migration trends. Perhaps if a system was orchestrated where larger inhibitor concentrations were implemented, then the analytical maths would match more closely with full Michaelis-Menten dynamics, however, this would undoubtedly have ramifications on the location of the turning point. Returning

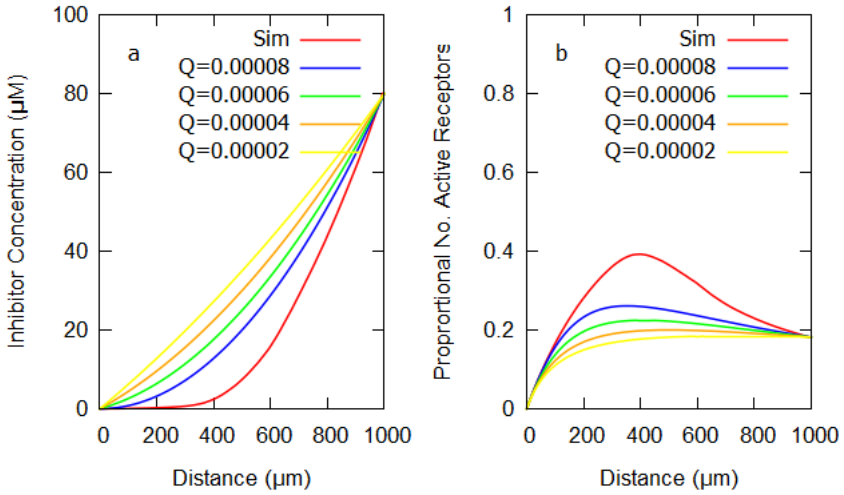

Figure 40: a) Analytical inhibitor equilibrium, in $C >> K_m$ limit, for different values of degradation parameter Q and b) corresponding active receptor gradients when: $C_{1a} = 2\mu M$, $K_b = 1\mu M$, $C_{1i} = 80\mu M$, $K_i = 10\mu M$ and $L = 1000\mu m$.

to the simulation at hand, a snapshot and average velocity output, at equilibrium, has been provided in Figures 41 and 42.

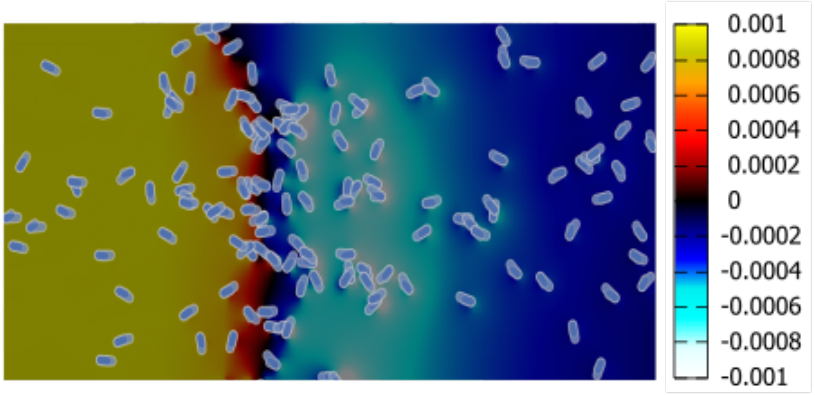

Figure 41: Simulation snapshot after 30 minutes, when the steady state has approximately been reached, for: $C_{1a} = 2\mu M$, $K_a = 1\mu M$, $C_{1i} = 80\mu M$, $K_i = 10\mu M$, $D = 20000\mu m^2 min^{-1}$, $K_m = 2\mu M$, $V_{max} = 1000\mu M min^{-1}$ and $L = 1000\mu m$.

The expected trends are seen from both the simulation rendering and the inverting of the sign of the cell velocities at $x = 400\mu M$. Furthermore, it can be seen that cells are accumulating at the turning point in the simulation snapshot. An additional simulation mechanism, which, until this point, has been discounted due to a lack of significant impact on the system and unnecessary over complication when fundamental mechanics were being investigated, becomes much more relevant in this case. This mechanism is that of cellular degradation in the source, due to cells located there. It was shown, from equation (80) that the turning point in cell directional cues varies with the final inhibitor concentration, which, if breakdown is accounted for in the source, will change with time. Specifically, as lower values of C_{1i} re-

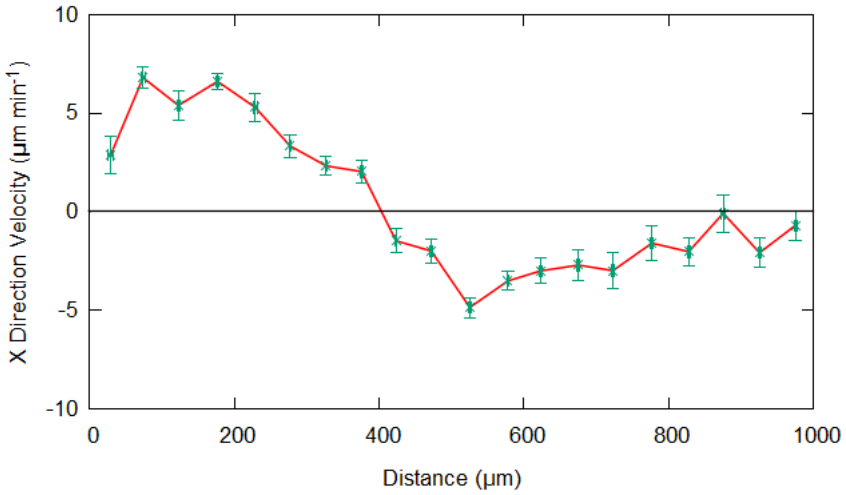

Figure 42: Average simulated velocity output for times after 30 minutes, when the steady state has approximately been reached, for: $C_{1a} = 2\mu M$, $K_a = 1\mu M$, $C_{1i} = 80\mu M$, $K_i = 10\mu M$, $D = 20000\mu m^2 min^{-1}$, $K_m = 2\mu M$, $V_{max} = 1000\mu M min^{-1}$ and $L = 1000\mu m$.

sult in increasingly prevalent positive migration, the turning point should drift towards larger distances, with time. This mechanism does essentially mean that chemical equilibrium will not exist until the final inhibitor concentration reaches zero, which may take a rather long time, however, comparisons can still be drawn over the time frames considered in the previous simulation. In order to investigate this dynamic, a mirror simulation will be run with the source volume, V, and number of cells in the source, N, being specified, allowing for a variable rate of inhibitor degradation. Figure 43 gives the chemical concentrations and the temporal progression of the active receptor gradient over the same time frames as the previous simulation.

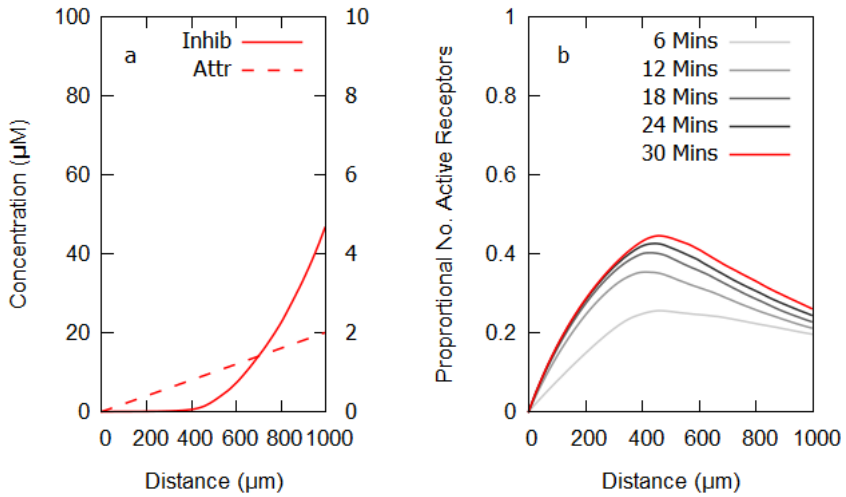

Figure 43: a) Simulated steady state concentrations (times after 30 mins) and b) temporal effect on the active receptor gradient when inhibitor breakdown in the source is accounted for, where: $C_{1a} = 2\mu M$, $K_a = 1\mu M$, $C_{1i} = 80\mu M$, $K_i = 10\mu M$, $D = 20000\mu m^2 min^{-1}$, $K_m = 2\mu M$, $V_{max} = 1000\mu M min^{-1}$, $L = 1000\mu m$, $V = 1000L^2$ and $N = 40$.

It can be seen that cellular degradation of the source of inhibitor is capable of reducing inhibitor concentrations by a significant amount over relatively short time frames. For the parameters considered here the inhibitor has decreased almost twofold from its original concentration; this should cause a marked deviation from the behaviour of the first simulation, for which the final inhibitor concentration remains constant. The corresponding effect of this breakdown on the active receptor gradient, and ultimately the cell directional bias, is to shift the turning point towards the latter end of the gradient, as predicted, such that after 30 minutes or so the turning point is more or less central at $x = 500\mu m$. Additionally, it can be seen that overall receptor activation at the far end of the gradient steadily increases with time. This is to be expected, however, as decreasing amounts of inhibitor - which in turn decreases receptor activation - will naturally increase Ω. A simulation snapshot and average velocity plot for this scenario has been provided in Figures 44 and 45, where the shifted turning point is presented clearly alongside the expected directional trends.

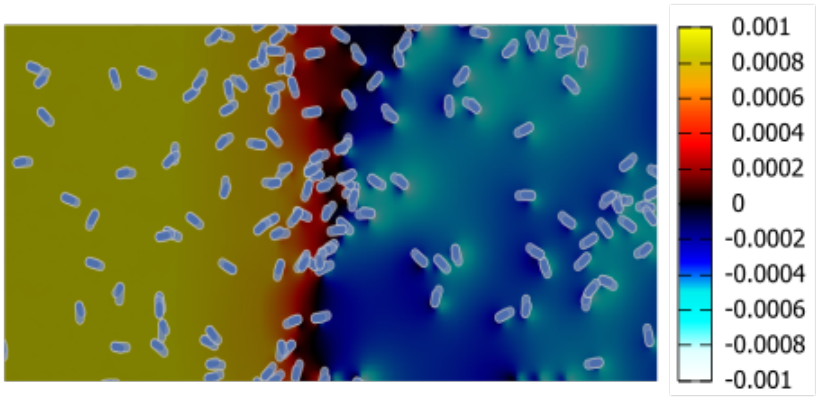

Figure 44: Simulation snapshot after 30 minutes, when the steady state has approximately been reached and inhibitor breakdown in the source is accounted for, where: $C_{1a} = 2\mu M$, $K_a = 1\mu M$, $C_{1i} = 80\mu M$, $K_i = 10\mu M$, $D = 20000\mu m^2 min^{-1}$, $K_m = 2\mu M$, $V_{max} = 1000\mu M min^{-1}$, $L = 1000\mu m$, $V = 1000L^2$ and $N = 40$.

5.2.2 Experiments

It's now an appropriate time to return, once again, to the experimental evaluation stage by testing NC4 *D. discoideum* in an Insall chemotaxis chamber. As always, the non-degradable agonist shall be provided for by Sp-cAMPS, which, until this point has supplied such accurate recapitulation of mathematical predictions that its properties are close to unquestionable. The candidate for a degradable antagonist is, once again, 8-CPT-cAMP, which gave compellingly similar behaviour to that expected of a degradable inhibitor competed against a background of attractant, in section 4.1. This particular experiment will, however, show indisputably whether or not 8-CPT-cAMP is a degradable antagonist. This is due to the fact that the conflicting directional biases presented in the maths thus far is only possible when the inhibitor gradient is exclusively non-linear, which can only come about from cellular degradation. The only thing to do now is recreate the chemical conditions utilised in the

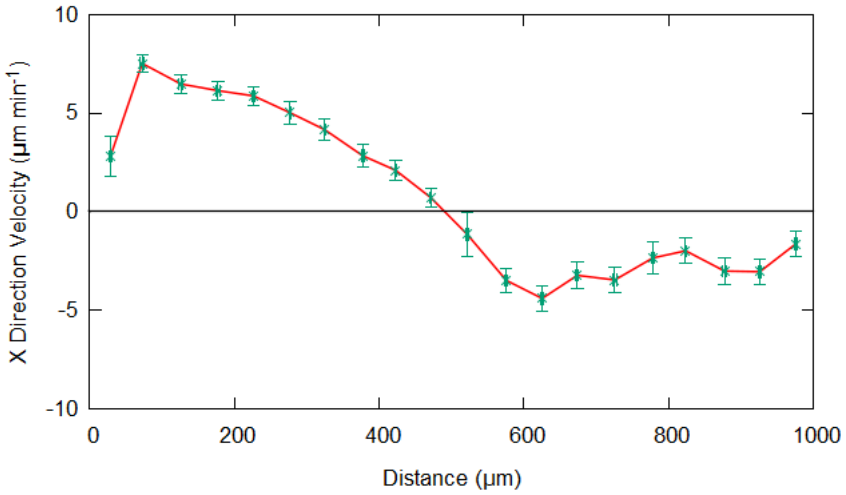

Figure 45: Average simulated velocity output for times after 30 minutes, when the steady state has approximately been reached and inhibitor breakdown in the source is accounted for, where: $C_{1a} = 2\mu M$, $K_a = 1\mu M$, $C_{1i} = 80\mu M$, $K_i = 10\mu M$, $D = 20000\mu m^2 min^{-1}$, $K_m = 2\mu M$, $V_{max} = 1000\mu M min^{-1}$, $L = 1000\mu m$, $V = 1000L^2$ and $N = 40$.

simulations section and measure the cell response. An snapshot and velocity plot of the corresponding experiment are demonstrated in Figures 46 and 47, respectively.

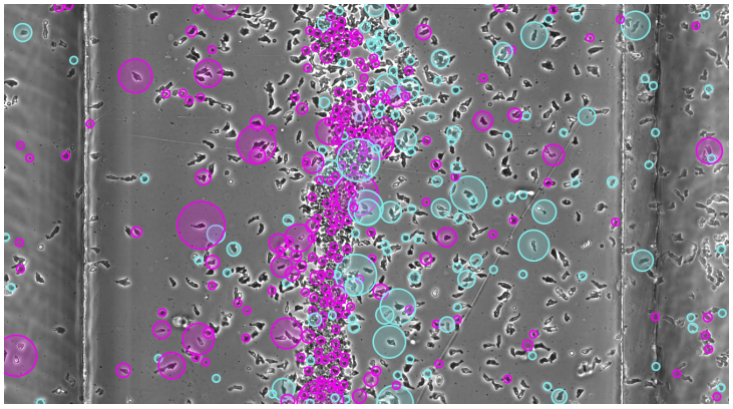

Figure 46: Experiment snapshot, at approximate equilibrium, of NC4 strain of *D. discoideum* subject to a $0-2\mu M$ gradient of Sp-cAMPS and a $0-80\mu M$ gradient of 8-CPT-cAMP. Cyan circles correspond to motion to the LHS (chemorepulsion) and magenta circles correspond to motion to the RHS (chemoattraction), with the size of the circle giving the magnitude of the x direction velocity.

Both the experiment snapshot and velocity output show, without doubt, positive migration occurring at small distances and reverse migration occurring at large distances. The snapshot shows the resultant accumulation of cells at point separating the conflicting directional regimes, located approximately centrally, in what looks like a wall of cells. Although the response seems a bit stronger in the experiment, the location of the turning point matches very well, so the parameters used in the maths are likely similar to reality. Its hard to say if inhibitor degradation in the source is a strong factor in causing the turning point to be located where it is, from a simulations perspective, as different degradation parameters could be im-

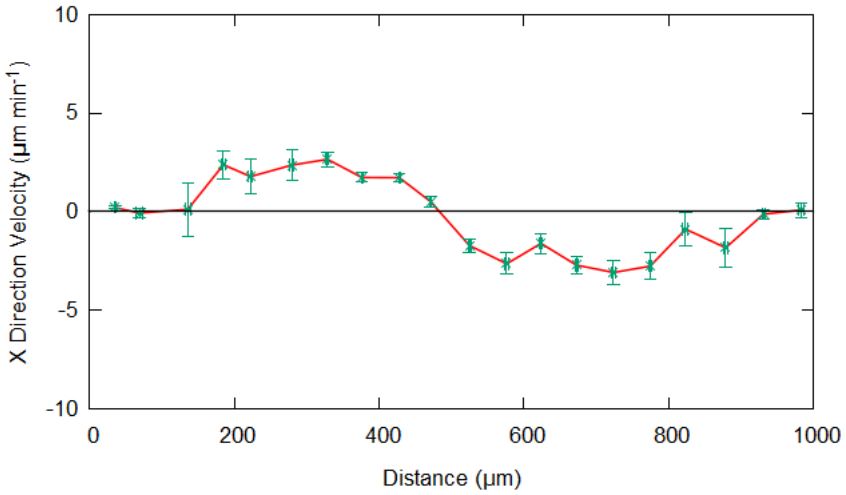

Figure 47: Measured cell velocities, at equilibrium, of NC4 strain of *D. discoideum* subject to a $0 - 2\mu M$ gradient of Sp-cAMPS and a $0 - 80\mu M$ gradient 8-CPT-cAMP.

plemented to force the turning point further up the gradient, thus achieving the same effect without accounting for inhibitor breakdown in the source. In the experiment, however, it did seem that the band of cells, indicating the turning point, drifted to the right slightly with time. This can be seen by inspecting a snapshot of a much earlier time, before approximate equilibrium, when the band of cells was just forming, shown in Figure 48. It is clear from the distribution of magenta and cyan, representing attractant and repulsion, respectively, that the turning point, at this earlier time, is located further to the left, and consequently shifts to the more central location seen in Figure 46, with time. This matches with the prediction that the turning point would drift up the gradient if the inhibitor was being broken down by cells in the source, suggesting that inhibitor breakdown in the source is playing a role in the system dynamics. It can thus be concluded that 8-CPT-cAMP is indeed a degradable competitive inhibitor, that a mixture of linear and non-linear gradient types can give rise to opposing directional responses over the gradient length, and that chemical degradation in a source should be paid attention to as a potential influencing factor over cellular responses.

A final point that should be made clear here is that this section also validates the non-degradable nature of the inhibitor Sp-8-CPT-cAMPS. This is due to the fact that, as SP-cAMPS is most definitely non-degradable, shown in Figures 8 and 9, if Sp-8-CPT-cAMPS were degradable, then the same types of conflicting directional cues seen in this section would have also become apparent in section 3.2. To recap, exclusive repulsion was seen over the space with the strongest repulsion occurring at the start of the gradient, tailing off with distance. The closest possible behaviour that could be achieved, if Sp-8-CPT-cAMPS were degradable, would be if overwhelming antagonist concentrations were used, such that the positive migration seen when the degradable inhibitor gradient is most flat, at small distances, is nullified. Even in this case there would at least be a dip in the response at this point, as the inhibitor gradient would be less steep and provides a less pronounced reduction in receptor activation. The fact that this does not occur, combined with the average

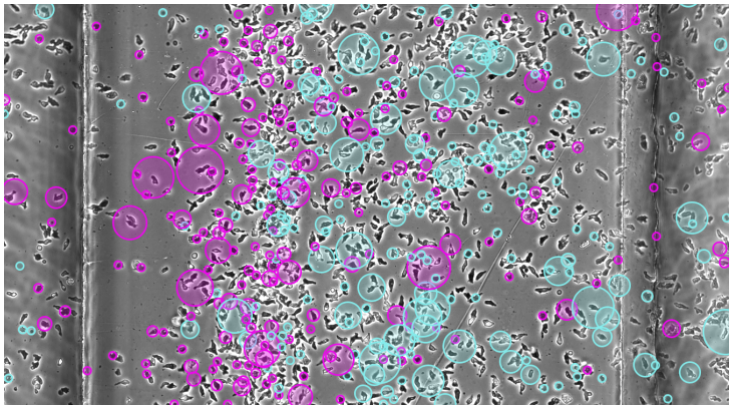

Figure 48: Experiment snapshot, at early times, of NC4 strain of *D. discoideum* subject to a $0 - 2\mu M$ gradient of Sp-cAMPS and a $0 - 80\mu M$ gradient of 8-CPT-cAMP. Cyan circles correspond to motion to the LHS (chemorepulsion) and magenta circles correspond to motion to the RHS (chemoattraction), with the size of the circle giving the magnitude of the x direction velocity.

concentrations used, is further indication that this system is linear, and Sp-8-CPT-cAMPS is non-degradable.

5.3 Complex Degradable Attractant Dynamics

So, it has been shown beyond doubt that a turning point in cell directional bias, causing a convergence of cells, can be induced using a degradable inhibitor. What conditions, then, could be used to give rise to a turning point from which cells diverge? The effect would be akin to that of Moses parting the red sea, if the sea comprised of *D. discoideum*. The most intuitive path to achieving this would be to invert the chemical conditions, such that a linear gradient of inhibitor was competed against a non-linear gradient of attractant. This should be easy to replicate experimentally as well, due to the fact that it has been proved in this thesis that Sp-8-CPT-cAMPS is a non-degradable inhibitor, and there is already clear evidence that the attractant cAMP is degradable. An immediate problem arises, however, in that if all gradients start from zero concentration, meaning no receptor activation at $x = 0$, then the reductions in receptor activation which lead to reverse migration cannot physically occur. An obvious solution to this issue is to simply start the gradient of cAMP from a non-zero concentration, guaranteeing non-zero receptor activation, but degradation could easily cause the gradient to dip - such that $\frac{\partial C}{\partial x} < 0$ for a time - before increasing to its final concentration. This type of converse gradient direction has been strictly avoided with the intention of making regions of positive or reverse migration very easy to identify. Specifically, only gradients strictly of the form $\frac{\partial C}{\partial x} > 0$ have been considered. This means that any regions where $\frac{\partial \Omega}{\partial x} > 0$ - and cells travel to the right - correspond purely to attraction, and regions where $\frac{\partial \Omega}{\partial x} < 0$ - and cells travel to the left - unequivocally imply repulsion. As the only way to guarantee $\frac{\partial C}{\partial x} > 0$, for an enzymatically degradable chemical, is to start the gradient from zero concentration, another solution must be found to give the necessary non-zero starting receptor activation.

There is a rather simple fix to this problem in that a background of Sp-cAMPS, providing a uniform background of receptor activation, can be superimposed. This gives non-zero receptor activation at the start of the gradient while still allowing all other gradients to increase monotonically with x. It is now possible for a decrease in receptor activation, due to inhibitor interference with the background of attractant, to occur at small distances. This is feasible as the gradient of cAMP will be very shallow here, and the correspondingly small rate of increase in receptor activation will not outweigh the rate of decrease seen from the linear inhibitor gradient, resulting in a net decrease, and chemorepulsion. At larger distances, however, the sharpness of the cAMP gradient will increase dramatically, causing the corresponding rate of receptor activation increase to overpower the rate of decrease from the inhibitor, resulting in a net increase, and chemoattraction. The overall effect will be a parting of cells, away from another turning point in cell directional cues. This three part system is the most complex that has been considered yet, but, as always, equation (5) can be used to find an expression that illustrates how proportional numbers of active receptors can be expected to vary with space, relative to any number of chemical gradients, allowing insight into expected response directions and strengths for this rather intricate set up. Characteristics of the non-linear gradient of attractant, linear gradient of inhibitor and background of attractant shall be denoted with subscripts a, i and b, respectively. Additionally, all attractants and inhibitors shall assumed to be perfect agonists and antagonists, such that $\alpha_a = 1$, $\alpha_i = 0$ and $\alpha_b = 1$.

The final aspect to be considered is the form of the gradient of degradable attractant, as equations (21) and (26) demonstrate gradient forms in the limit $C << K_m$ and $C >> K_m$. In sections 4.1 and 4.2, it was reasonably safe to assume the high concentration limit as large concentrations were consistently used. This was due to a theoretically and experimentally derived dissociation constant, for 8-CPT-cAMP, in about the same order of magnitude as $K_d = 10\mu M$. As the dissociation constant is the concentration at which binding is half maximal, it essentially dictates the amount of receptor binding that will occur for any given concentration. As such, this is the key parameter to consider when selecting gradient concentrations for any given system. The lower the dissociation constant, the larger the effect on receptor binding for any given concentration. The issue here is that cAMP has a reported dissociation constant of $K_d = 5nM$, which is about three orders of magnitude less than those of the chemical utilised thus far. This means that far smaller concentrations have to be used in order to elicit the same sorts of effects. Now, the elusive quantity K_m, the concentration at which degradation effects are half maximal and the key parameter in deducing which concentration limit to use, is problematic to quantify. The only clue as to its value is the harmony that has thus far been observed between simulations, for which the value $K_m = 2\mu M$ has been used, and corresponding experimental work. As simulations have matched substantially well, it can be speculated that the parameters are at least within an order of magnitude of reality. So, assuming that $K_m \approx 1\mu M$, and that this hold true for both cAMP and 8-CPT-cAMP,

it was reasonable to take the limit $C >> K_m$ when final 8-CPT-cAMP concentrations of $C_{1i} \approx 100\mu M$ were being used. Unfortunately, however, returning to the cAMP case, with the very low dissociation constant of $K_d = 5nM$, these same concentrations will completely overwhelm all other signals and any directional complexities will likely be lost. Much better would be to use concentrations of the order $C_{1a} \approx 1\mu M$, but this is very close to K_m and bodes the question of the concentration approximations failing. From the perspective of the high concentration limit, the degradation parameter $Q = 0.0002\ \mu M \mu m^{-2}$, corresponding to an analytical $V_{max} = 8\mu M min^{-1}$ when $D = 20000\ \mu m^2 min^{-1}$ - according to equation (25) - correlated very well with simulations running the discrete degradation parameters $K_m = 2\mu M$ and $V_{max} = 1000\mu M min^{-1}$, in section 4.1. This simulation, in turn, matched very well with the behavioural output of the corresponding assay that was performed. This means that an analytical $V_{max} = 8\mu M min^{-1}$, acting as a continuum, correlated well with reality. Unfortunately, in the limit $C >> K_m$, the law $Q \leq Q^*$ must be obeyed or the gradient will dip into negative concentrations and be completely irrelevant. This means that, according to equation (69), the value $V_{max} = 8\mu M min^{-1}$, and $Q = 0.0002\ \mu M \mu m^{-2}$, can only be applied to scenarios where $C_{1a} \geq 200\mu M$. Note that C_{1i} has been replaced by C_{1a} here as it is the attractant that is degradable here, not the inhibitor. In order to use the $C >> K_m$ limit for concentrations $C_{1a} \approx 1\mu M$ it would be required to reduce Q, and V_{max}, by about two order of magnitude, which guarantees this analytical maths being next to irrelevant as - with degradation parameters this low - the gradient would essentially be linear. In short, the limit $C >> K_m$ is totally unsuitable for this case, so, the only other option, from an analytical point of view, is to try the limit $C << K_m$. This limit may also be inappropriate, as concentrations close to K_m will likely have to be used, but there is also a possibility that this analysis could be useful. At least with this approximation the rate of degradation scales with concentration, meaning that negative concentrations are impossible. So, taking a linear form for the non-degradable inhibitor, a constant value for the non-degradable attractant background, and assuming the $C << K_m$ gradient form for the degradable attractant - from equation (21) - the active receptor gradient in the low concentration limit can be found, from equation (5), as

$$\Omega(x) = \frac{\frac{C_{1b}}{K_b} + \frac{1}{K_a}\left\{\frac{C_{1a}\sinh Rx}{\sinh RL}\right\}}{1 + \frac{C_{1b}}{K_b} + \frac{1}{K_i}\left\{\frac{C_{1i}x}{L}\right\} + \frac{1}{K_a}\left\{\frac{C_{1a}\sinh Rx}{\sinh RL}\right\}}. \tag{81}$$

Note that the trigonometric identity $2\sinh x = e^x - e^{-x}$ has been utilised here. Also, if required, information on the low concentration degradation parameter, R, can found in section 1.5.2, specifically equations (16) and (19). Now, the derivative of equation (81) with respect to space, giving information on both the expected direction and strength of any response in this concentration regime, can then be found as

$$\frac{\partial \Omega}{\partial x} = \frac{\frac{RC_{1a}\cosh Rx}{K_a \sinh RL}\left\{1 + \frac{C_{1i}x}{K_i L}\right\} - \frac{C_{1i}}{K_i L}\left\{\frac{C_{1b}}{K_b} + \frac{C_{1a}\sinh Rx}{K_a \sinh RL}\right\}}{\left[1 + \frac{C_{1b}}{K_b} + \frac{1}{K_i}\left\{\frac{C_{1i}x}{L}\right\} + \frac{1}{K_a}\left\{\frac{C_{1a}\sinh Rx}{\sinh RL}\right\}\right]^2}. \tag{82}$$

If there is any spatially resolved turning point then it exists at the point where this equation is equal to zero, as this is the point that separates the regimes $\frac{\partial \Omega}{\partial x} < 0$ and $\frac{\partial \Omega}{\partial x} > 0$, corresponding to negative and positive migration, respectively. Upon setting equation (82) to zero, the subsequent relationship can be rearranged easily in terms of the attractant background concentration, giving

$$\frac{\partial \Omega}{\partial x} = 0 \quad \Leftrightarrow \quad C_{1b} = K_b \left[\frac{C_{1a} K_i R L \cosh Rx}{C_{1i} K_a \sinh RL} \left\{ 1 + \frac{C_{1i} x}{K_i L} \right\} - \frac{C_{1a} \sinh Rx}{K_a \sinh RL} \right]. \tag{83}$$

This means that the regime $C << K_m$ has the capability to give rise to a turning point in cell directional that can be modulated via the attractant background. Equation (83) essentially allows one find the critical level of attractant background, given a specific configuration of system parameters, that will force the turning point to a desired location, x. Now, more information about this location could be derived by rearranging in terms of x, but, unfortunately, this is not feasible here as extracting x from both hyperbolic sine and cosine simultaneously is rather problematic. An iterative method, such as Newton-Raphson, could be employed to find x, but much of the system insight would be lost in this process. Instead, as always, it is worth plotting equation (83) in the form of a heat map, where the turning point should be clearly represented as a black boundary separating cold and hot colors. Figure 49 illustrates this, relative to a sensible parameter regime, with the attractant background being varied on the y-axis.

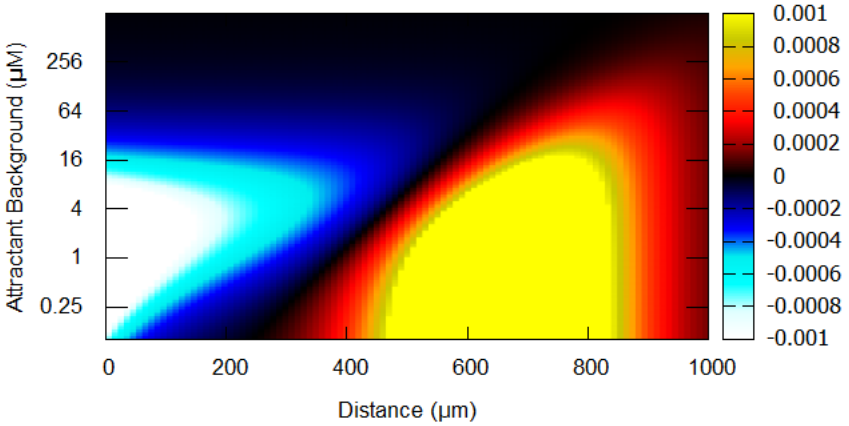

Figure 49: An analytical, chemotactic heat map. Plotted on the y-axis is the attractant background concentration ($K_b = 1\mu M$, $\alpha_b = 1$) and the x-axis shows variation with space. A linear gradient of non-degradable antagonist ($K_i = 10\mu M$, $C_{1i} = 100\mu M$, $\alpha_i = 0$) and exponential gradient of degradable agonist ($R = 0.014\mu m^{-1}$, $K_a = 0.005\mu M$, $C_{1a} = 5\mu M$, $\alpha_a = 1$), in a low concentration limit, has been assumed. The overall output indicates expected response strength and direction at different points in space, as the agonist background is varied. For additional details on heat map interpretation refer to Figure 4.

It should first be noted that the value of R used in Figure 49 was selected according to the continuum value of V_{max} which was utilised in section 4.1, because, as mentioned pre-

viously, this value this gave very good correlation between the analytical, numerical and experimental sections. This value was $V_{max} = 8\mu M min^{-1}$, which, using the usual diffusion coefficient of $D = 20000\ \mu m^2 min^{-1}$ and $K_m = 2\mu M$ - the Michaelis-Menten constant which so far has recapitulated reality to a very satisfactory degree - gives a corresponding low concentration degradation parameter of $R = 0.014\mu m^{-1}$, according to equations (19) and (16). It can be seen that the system, according to a low concentration approximation, is capable of providing a very effective turning point in cell directional cues that varies nicely with the attractant background . As the background gets smaller the region of chemorepulsion decreases in size, which makes sense as the background is required to see the decrease in receptor activation, from inhibitor binding, which induces reverse migration. The larger the background, the more there is to interfere with and the more effective the repulsion. That is, up until the point at which the background overwhelms the system and the reductions in receptor activation seen from inhibitor binding become obsolete, alongside the increases seen from the gradient of degradable attractant. The point at which the background ceases to exist is point at which reductions in receptor activation become impossible, resulting in a purely chemoattractive regime. Now, as far as choosing an attractant background concentration for simulations and experiments is concerned, it has been proved multiple times over how effective an Sp-cAMPS concentration of $2\mu M$ is as both a background and a gradient; as such, it seems wise to keep this unchanged. Additionally, and although it is expected that the gradient shape ascertained via the low concentration approximation will differ considerably from simulations - and reality - it can read from Figure 49 that a background of $2\mu M$ provides a more or less central turning point in cell directional cues, at $x \approx 400\mu m$. Even if there are discrepancies between the analytically and numerically attained gradients, the parameter configuration illustrated in Figure 49 is as good as any to begin further analysis.

5.3.1 Simulations

Simulations shall now be implemented to deduce the behavioural profile that can be expected when full Michaelis-Menten kinetics is accounted for, using the parameters described above. As always, this type of discrete numerical analysis will allow insight into non-equilibrium time frames and the effectiveness of the approximations made during the analytical maths sections. Figure 50 gives the approximate steady state concentration profiles of all chemicals present in the system and an evolution in time of the active receptor gradient, in the absence of degradation in the source.

It is clear that the desired effect of inducing a regime which causes cells to diverge from a directional turning point has been achieved, and that the degradable attractant has a non-linear profile. In comparison with Figure 39, however, it seems that the "equilibrium" is far less stable. This is obvious as, even though, after 30 minutes of simulation time, the turning point exists at approximately $x = 400\mu m$, the location orchestrated in the analytical maths section, the coordinate of the turning point seems to be changing quite rapidly with time. It can be safely assumed that this coordinate will drift to even smaller distances as more time

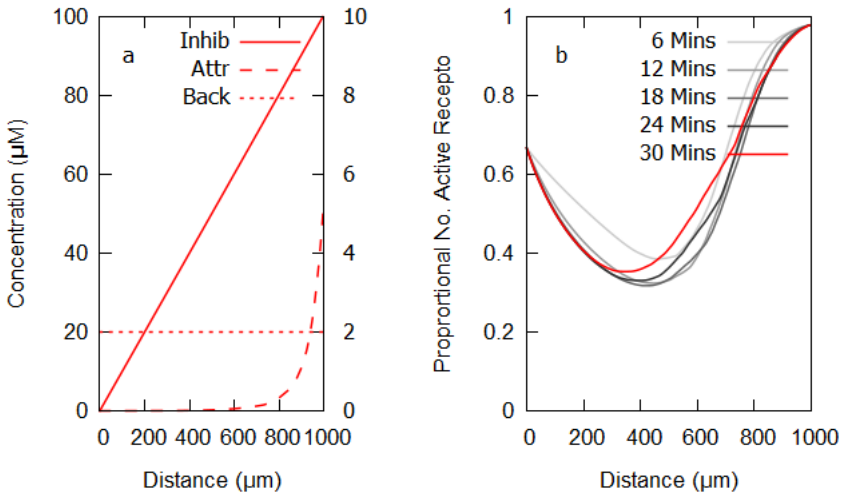

Figure 50: a) Simulated steady state concentrations (times after 30 mins) and b) temporal effect on the active receptor gradient when: $C_{1a} = 5\mu M$, $K_a = 0.005\mu M$, $C_{1i} = 100\mu M$, $K_i = 10\mu M$, $C_{1b} = 2\mu M$, $K_b = 1\mu M$, $D = 20000\mu m^2 min^{-1}$, $K_m = 2\mu M$, $V_{max} = 1000\mu M min^{-1}$ and $L = 1000\mu m$.

elapses. Conversely, Figure 39 illustrates a turning point that, 30 minutes into the simulation, has become very stable. The only difference, other than chemical parameters, between these two systems is the nature of the turning point: converging for Figure 39 and diverging for Figure 50. In a discrete system this likely becomes very important as the nature of the turning point dictates how the spatial distribution of cells changes with time. This is obviously going to affect the magnitude of degradation that occurs at each point in space, which directly impacts gradient shape and ultimately directional cues. In the converging system, the cells become increasingly tightly packed, to the point where chemical cues do not allow them to move away and their distribution essentially becomes temporally constant. This causes the degradation mechanics, and gradient shapes, to become similarly constant, leading to the steady state type behaviour seen in Figure 39. In the diverging system, however, cells are being pushed to the ends of the gradient, constantly changing the distribution of degradation, the shape of the degradable gradient and the directional cues of the cells. Perhaps the only steady state that can be achieved in this case is when cells migrate fully out of the space. The discrete nature of the simulations, where cells move and regions of degradation change with time, clearly gives rise to a feedback loop where cells are continually modulating their own chemical environment and chemotaxis. This means that a true equilibrium is essentially unattainable, however, it is clear that certain systems can encourage behaviour that will more closely resemble a steady state than others. This kind of insight could never arise from the analytical maths alone, as degradation is assumed to act as a continuum, mirroring a case where cells are evenly packed and don't move, which always leads to a solid and unchanging steady state. At this point it is also worth comparing degradable attractant gradient shapes at different values of the low concentration degradation parameter, R, and the corresponding active receptor gradients, with those of the current simulation, as demonstrated in Figure 51.

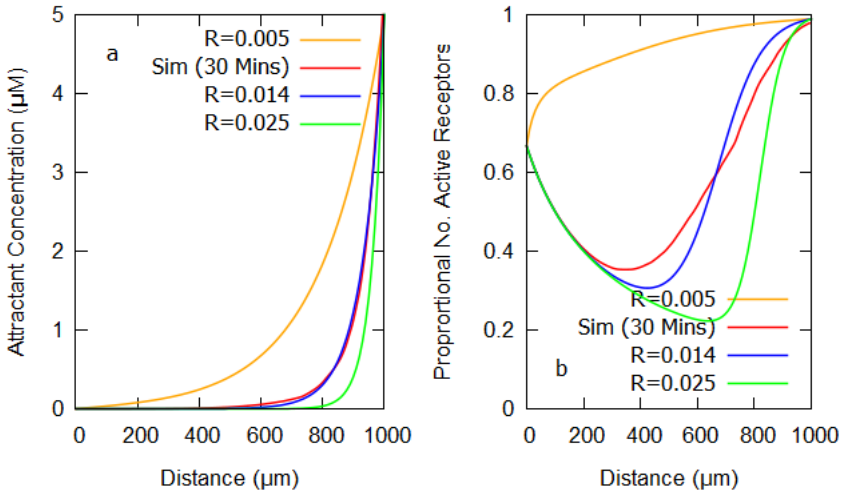

Figure 51: a) Analytical degradable attractant steady state concentration profiles in low concentration limit, for different values of R, and from simulation and b) subsequent active receptor gradients when: $C_{1a} = 5\mu M$, $K_a = 0.005\mu M$, $C_{1i} = 100\mu M$, $K_i = 10\mu M$, $C_{1b} = 2\mu M$, $K_b = 1\mu M$, $D = 20000\mu m^2 min^{-1}$, $K_m = 2\mu M$, $V_{max}(Simulation) = 1000\mu M min^{-1}$ and $L = 1000\mu m$.

In truly surprising fashion, it turns out that the low concentration approximation, $C << K_m$, is actually capable of replicating the full Michaelis-Menten system considerably well. Specifically, 30 minutes into the simulation, the analytical curve described by $R = 0.014\mu m^{-1}$ actually fits the numerically deduced attractant curve close to perfect. As was described previously this point is not an equilibrium, as can be seen from the rapid change in the form of the active receptor gradient in Figure 50.b, so it is likely that this high level of correlation will change with time, however the similarity is still remarkable. So much so, in fact, that it can be said with confidence that the low degradation parameter $R = 0.014\mu m^{-1}$ can be used as an accurate analytical approximation to simulations utilising the same system parameters as Figure 50, at least for time frames surrounding the 30 minute mark. This means that Figure 49 can likely be used to accurately predict the effect of changing the attractant background, over these same time frames. Returning to Figure 51, it can be seen that higher values of R increasingly flatten the gradient at small distances and sharpen the gradient at larger distances. This makes sense as, according to equations (16) and (19), higher values of R correspond to higher values of V_{max}, and more chemical breakdown. These very sharp gradients will allow chemorepulsion over a larger range, due to the very small rates of increase in receptor activation at smaller distances, but will cause very intense chemoattraction - the rate of increase in receptor activation completely overpowering the rate of decrease from the inhibitor - once the steep part of the gradient is reached. Conversely, as R, and V_{max}, decrease, the gradient will become increasingly linear. It can be seen from Figure 51.b that at some critically low value of R, clearly in the range $R \in [0.005, 0.014]$, the rate of increase in receptor activation seen from the attractant gradient outweighs the rate of reduction from the inhibitor at all points in in the gradient. Beyond this point it will be impossible to induce reverse migration, and a purely chemoattractive regime will emerge. This is what is observed for the orange curve, corresponding to $R = 0.005\mu m^{-1}$, in Figure 51. It would be expected

that the exponential, analytically deduced gradient - from the $C << K_m$ approximation - would be sharper than the simulated gradient at concentrations $C \approx K_m$. This is because the low concentration approximation gives steep, exponential gradients that begin to diverge from the true gradient shape as $C \to K_m$ concentrations; instead, however, this overly steep gradient matches with the gradient shape attained when numerics were employed to avoid the approximations made in the analytical maths. The unexpected correlation, at least at specific times, could potentially be because the overall directional bias for this type of system causes cells to migrate towards the gradient extrema. This means that higher than expected degradation, in simulation space, will occur at small and large distances, effectively flattening the gradient before making it sharper than it would be if the cells were evenly distributed. This could make the simulated gradient, ascertained via full Michaelis-Menten kinetics, at concentrations $C \approx K_m$, unexpectedly match the exponential gradient derived analytically using the approximation $C << K_m$. Returning to the simulation, Figure 52 supplies a snapshot at 30 minutes and Figure 53 illustrates average cell velocities for times surrounding 30 minutes. For velocity plots previous to this one, cell data for all times, after an approximate steady state was reached, was included. This made sense as the system could be seen to be essentially time independent for these times, so including all the data meant a more thorough analysis of the steady state. For this case, however, a steady state does not really seem to exist, so including a large range of times basically equates to averaging data which corresponds to a range of behavioural profiles. The output would be somewhat nonsensical. The only way to attain sensible velocity data is to focus on a small window of time, in this case times surrounding the 30 minute mark, thus guaranteeing that all measurements correspond to suitably similar response profiles. Although this only allows representation of a relatively small region in time, at least the data can be interpreted with ease.

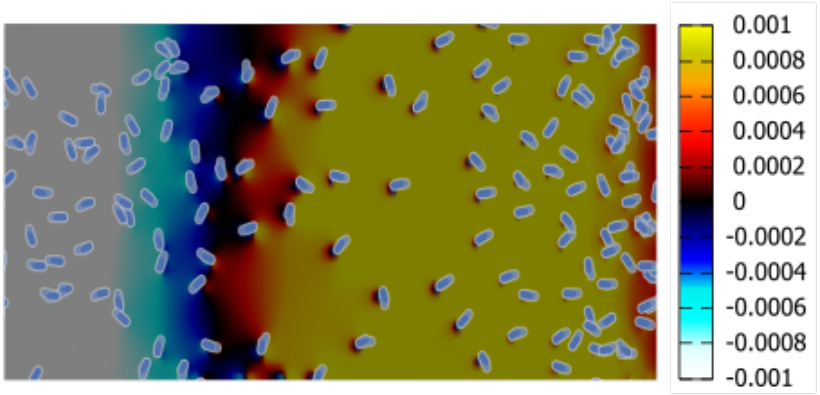

Figure 52: Simulation snapshot after 30 minutes for: $C_{1a} = 5\mu M$, $K_a = 0.005\mu M$, $C_{1i} = 100\mu M$, $K_i = 10\mu M$, $C_{1b} = 2\mu M$, $K_b = 1\mu M$, $D = 20000\mu m^2 min^{-1}$, $K_m = 2\mu M$, $V_{max} = 1000\mu M min^{-1}$ and $L = 1000\mu m$.

Both the simulation rendering and velocity data further reinforce the existence of a diverging turning point in cell directional cues. Although the location of this turning point is rather

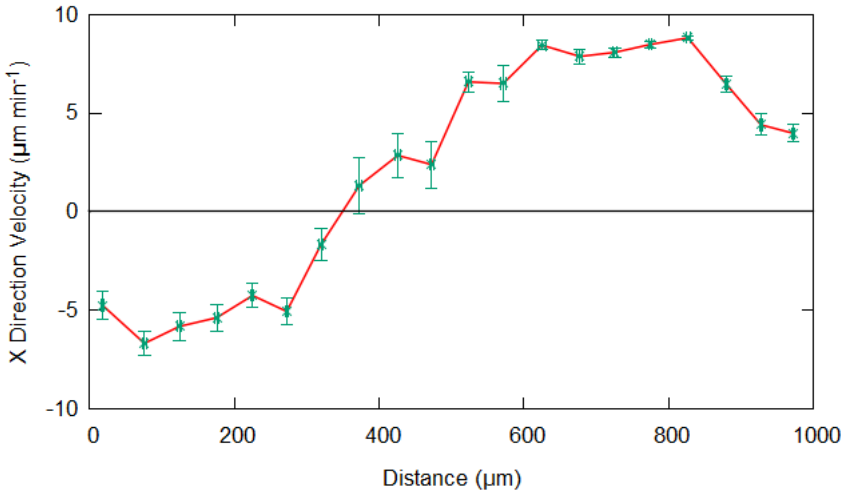

Figure 53: Average simulated velocity output for times surrounding 30 minutes when: $C_{1a} = 5\mu M$, $K_a = 0.005\mu M$, $C_{1i} = 100\mu M$, $K_i = 10\mu M$, $C_{1b} = 2\mu M$, $K_b = 1\mu M$, $D = 20000\mu m^2 min^{-1}$, $K_m = 2\mu M$, $V_{max} = 1000\mu M min^{-1}$ and $L = 1000\mu m$.

temporally inconsistent, it can be read from Figure 53 to exist at around $x = 350\mu m$, 30 minutes into the simulation. A further point of interest that arises from Figure 52 is the discrepancy in the level of influence each cell exerts on its environment. As described previously, environmental modifications can, naturally, only occur when a chemical is degradable, thus allowing cells to directly influence the number of molecules in the local area. Regions where this exertion plays a noticeable role in global levels of receptor activation, and consequently impacts cell directional cues, can be identified when the immediate area surrounding a cell has inconsistent receptor activation rendering. This inconsistency corresponds to the steeper degradable gradient which surrounds each cell, and the subsequent perturbation in receptor binding and activation. With this in mind, it can be seen from Figure 52 that cells at the beginning of the gradient have little to no influence on global directional cues. This makes sense upon inspecting the simulated degradable attractant gradient form in Figure 51.a, where it is clear that only very small amounts of degradable attractant are present in the initial parts of the gradient. If there is no attractant present then there is nothing for the cells to degrade, and no way for the cell to influence its environment. In this region the cells are completely under the influence of the non-degradable aspects of the system, specifically the background of non-degradable attractant and linear gradient of non-degradable inhibitor, resulting in a chemorepulsive regime over which the cells have no sway. About halfway up the gradient, it can be seen that cells are surrounded by a small micro environment of receptor activation, suggesting that levels of cellular breakdown are significant enough for cells to begin to change the amounts of receptor activation in their immediate area. As it is the attractant which is degradable, the effect of breakdown is to lower levels of receptor activation. This means that each cell becomes a small receptor activation sink which effectively repels other cells, which always travel in the directional of receptor activation increase. The inverse to this situation was seen in Figure 33, where it was inhibitor which was degradable and the result of the degradation was to increase local levels of receptor activation. This

turned each cell into a local peak in receptor activation, capable of attracting other cells and further compounding the effect. Now, further up the gradient in Figure 52, the cell micro environments seems to steadily disappear as the gradient comes to an end. This seems counter intuitive as larger concentrations correspond to larger levels of enzymatic breakdown, upto the the maximum rate of degradation, V_{max}, which surely must correspond to a larger impact on the chemotactic environment. The key to understanding what is happening here is to, once again, think in terms of receptor binding. Returning to Figure 2.a, it was clear that larger changes in receptor binding, the factor that translates directly into receptor activation and chemotaxis, occur at lower concentrations. This means that the overall difference in concentration has a different impact on receptor binding depending on where this difference lies in concentration space. As a result, a smaller amount of degradation, at lower concentrations, can have a larger impact on the chemotactic environment than a larger difference at higher concentrations, which is exactly what is seen in the latter part of the gradient in Figure 52. A final numerical exercise worth running is this same situation but also accounting for enzymatic degradation of the attractant in the source. In section 4.2 it became clear that this dynamic, relative to inhibitor degradation, played an important role in the migration mechanics. This was due to the mathematically predicted, and experimentally verified, drifting of the directional turning point to larger distances, which would only occur if source levels of inhibitor were decreasing with time. For this simulation both the volume of the source, V, and number of cells in the source, N, shall once again be specified in order to probe the effect of a specific rate of degradation. Figure 54 illustrates the new chemical profiles and subsequent temporal effect on active receptor gradient with this additional dynamic.

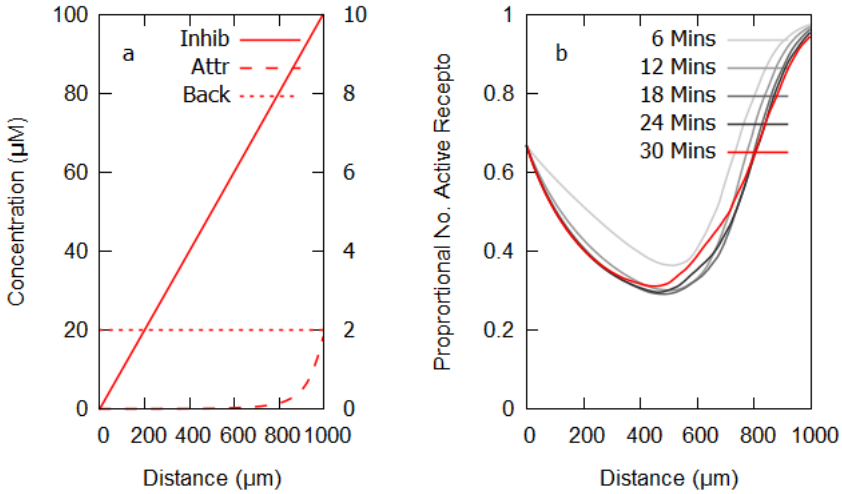

Figure 54: a) Simulated steady state concentrations (after 30 mins) and b) temporal effect on the active receptor gradient when attractant breakdown in the source is accounted for, for: $C_{1a} = 5\mu M$, $K_a = 0.005\mu M$, $C_{1i} = 100\mu M$, $K_i = 10\mu M$, $C_{1b} = 2\mu M$, $K_b = 1\mu M$, $D = 20000\mu m^2 min^{-1}$, $K_m = 2\mu M$, $V_{max} = 1000\mu M min^{-1}$, $L = 1000\mu m$, $V = 1000L^2$ and $N = 75$.

For this case, by the time 30 minutes of simulation time has elapsed, the concentration of attractant in the source has reduced to less than half its initial value. In comparison with Fig-

ure 50, it seems that the effect of this source degradation is to slow the drifting of the turning point to smaller distances, as can be seen from the much more tightly packed active receptor curves. This makes sense as less attractant in the source is going to reduce the chemoattractive aspect of the system, causing the chemorepulsive window, which arises from the unchanging non-degradable chemicals, to become increasingly prevalent, pushing the turning point to larger distances. However, as the nature of the non source degradation system causes the directional turning point to drift rapidly to smaller distances, the effect essentially balances this drift and stabilises the turning point, resulting in something resembling a steady state. As a result, after 30 minutes, the turning point is located much more centrally than in the non source degradation case. Figures 55 and 56 give a simulation snapshot and velocity plot for times surrounding the 30 minute mark, further illustrating the shifted tuning point.

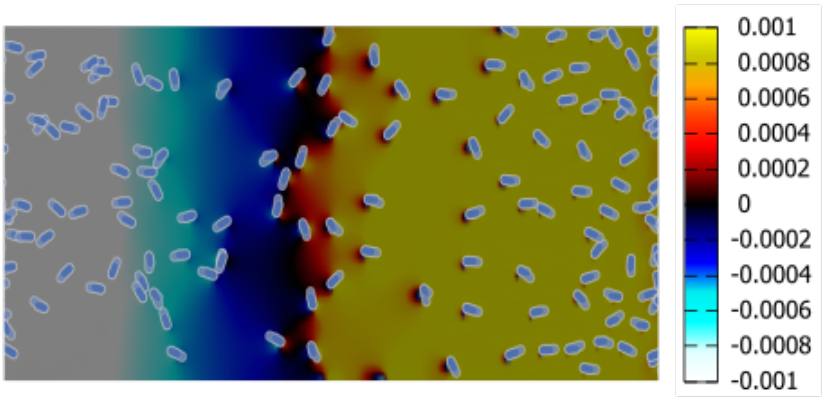

Figure 55: Simulation snapshot after 30 minutes, when attractant breakdown in the source is accounted for, where: $C_{1a} = 5\mu M$, $K_a = 0.005\mu M$, $C_{1i} = 100\mu M$, $K_i = 10\mu M$, $C_{1b} = 2\mu M$, $K_b = 1\mu M$, $D = 20000\mu m^2 min^{-1}$, $K_m = 2\mu M$, $V_{max} = 1000\mu M min^{-1}$, $L = 1000\mu m$, $V = 1000L^2$ and $N = 75$.

5.3.2 Experiments

Finally, it is time to test out this most complicated of models on NC4 *D. discoideum* in an Insall chemotaxis chamber. The non-degradable attractant background shall be provided for using Sp-cAMPs, the non-degradable inhibitor gradient using Sp-8-CPT-cAMPS, and the degradable attractant gradient using cAMP. Through repeated accurate recapitulation of mathematically predicted behaviour, the chemicals Sp-cAMPS and Sp-8-CPT-cAMPS have been proven to express the qualities inherent of a non-degradable agonist and antagonist, with dissociation constants close to those demonstrated in the mathematical analysis. If this model can also be recreated experimentally then this is but further proof of these properties. The nature and dissociation constant of cAMP has already been investigated and inserted into the mathematical model, with the only unknown quantities residing in the degradation mechanics in the form of the maximum rate of degradation, V_{max}, and the concentration at which half maximal degradation occurs, K_m. These have been guessed at from previous correlations between predictions and experiments, but their validity will only become apparent

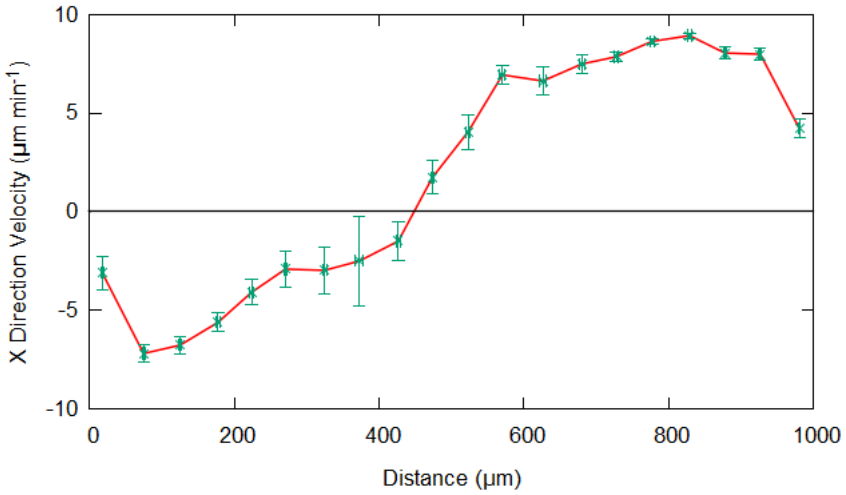

Figure 56: Average simulated velocity output for times surrounding 30 minutes, when attractant breakdown in the source is accounted for, where: $C_{1a} = 5\mu M$, $K_a = 0.005\mu M$, $C_{1i} = 100\mu M$, $K_i = 10\mu M$, $C_{1b} = 2\mu M$, $K_b = 1\mu M$, $D = 20000\mu m^2 min^{-1}$, $K_m = 2\mu M$, $V = 1000L^2$ and $N = 75$.

upon comparison between the experimental output and the mathematical analysis presented. The cell behaviour upon applying the same concentration regime utilised in the simulations section can be summarised in the temporally distinct experiment snapshots of Figures 57 and 58.

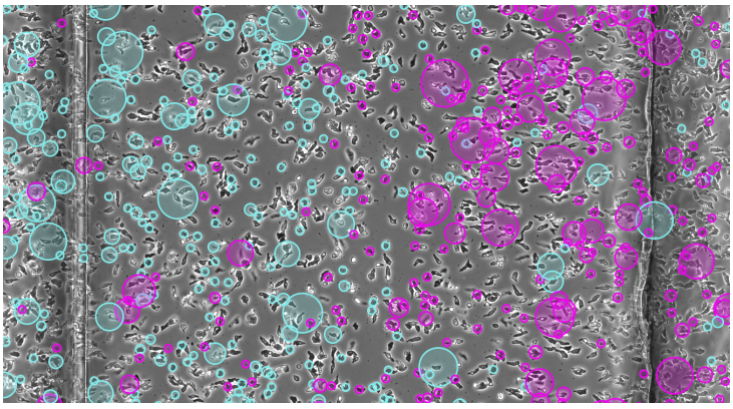

Figure 57: Experiment snapshot, at early times, of NC4 strain of *D. discoideum* subject to a $0 - 100\mu M$ gradient of Sp-8-CPT-cAMPS, a $2\mu M$ background Sp-cAMPS and a $0 - 5\mu M$ gradient of cAMP. Cyan circles correspond to motion to the LHS (chemorepulsion) and magenta circles correspond to motion to the RHS (chemoattraction), with the size of the circle giving the magnitude of the x direction velocity.

It can be immediately observed that desired migratory pattern has been achieved, with strong positive and reverse migration occurring at large and small distances, respectively. Cells clearly diverge away from the boundary between these directional regimes, which is located approximately centrally. Furthermore, upon inspecting for any discrepancies in the location of this turning point between the two figures, it can be seen that the turning point is very temporally stable. This matches perfectly with the prediction that degradation of cAMP in

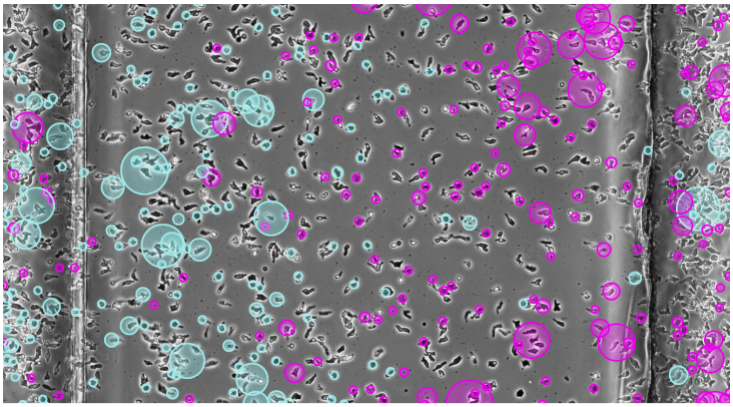

Figure 58: Experiment snapshot, at later times, of NC4 strain of *D. discoideum* subject to a $0 - 100\mu M$ gradient of Sp-8-CPT-cAMPS, a $2\mu M$ background Sp-cAMPS and a $0 - 5\mu M$ gradient of cAMP. Cyan circles correspond to motion to the LHS (chemorepulsion) and magenta circles correspond to motion to the RHS (chemoattraction), with the size of the circle giving the magnitude of the x direction velocity.

the source stabilises the turning point, leading to a pseudo steady state. Of course, once all the cAMP has been degraded, only the unchanging quantities of non-degradable SP-8-CPT-cAMPS and Sp-cAMPS will remain, resulting in a purely chemorepulsive regime. This means that the ultimate steady state of this system will be purely reverse migratory, however, for a substantial amount of time, the balance between spatially and temporally varying degradation mechanics, due to biased cell motion, and changing amounts of cAMP in the source, due to breakdown, could trick one into believing that the equilibrium state is actually of diverging chemotactic nature. Regardless, the stability of the diverging system over large time frames means that velocity measurements can be extracted over similarly large time frames for an accurate quantification of the variation in cell velocities over the bridge length, illustrated in Figure 59.

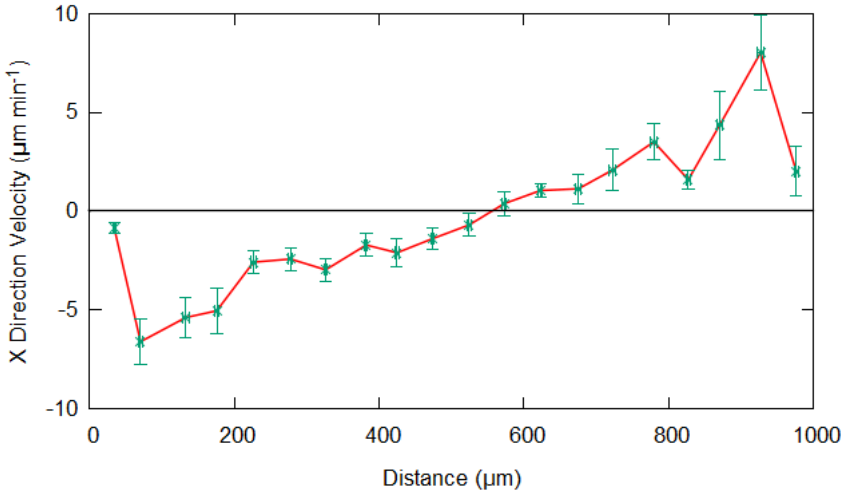

Figure 59: Measured average cell velocities, for times over which the system is temporally stable, of NC4 strain of *D. discoideum* subject to a $0-100\mu M$ gradient of Sp-8-CPT-cAMPS, a $2\mu M$ background Sp-cAMPS and a $0 - 5\mu M$ gradient of cAMP.

In comparison with Figure 56, it seems that the simulated response is somewhat stronger than reality and the turning point is shifted slightly further up the gradient. This suggests that there are some minor discrepancies between the two systems, perhaps the estimated dissociation constants or degradation parameters, however, considering the complexity of the model, this can still be regarded as a fantastic mathematical recapitulation. As an additional point, if it was at all uncertain that cAMP was degradable then this is concrete proof that it must be. A diverging turning point in cell directional cues simply could not occur unless the chemicals at play had the hypothesised properties. Finally, it is worth noting the strength of the model that has been presented thus far. Starting from the simple idea that a competitive inhibitor could be used to interfere with the receptor activation that arises from a gradient of chemoattractant, and ultimately alter expected chemotactic biases, mathematics has been used to probe increasingly complex permutations of this concept, culminating in some truly novel predictions on cell migrations dynamics. By itself this could never evolve beyond a simply intriguing concept, but upon repeated experimental verification it becomes clear that this model cannot be anything other than true.

6 Discussion

Most key observations have been noted alongside the corresponding result in the previous section. By placing these key deductions directly in their context it is hoped that the greatest possible understanding and intuition can be achieved. There are, however, a few points of particular import that should be discussed.

Firstly is the robust mechanism by chemorepulsion can be mediated. It has been shown beyond doubt - via modelling and experimental verification in sections 3.1 and 3.2 - that chemorepulsion can be effectively induced relative to a gradient of chemoattractant if an appropriate gradient of antagonist is superimposed. Repulsion is achieved if the rate of receptor blocking, due to the antagonist, outweighs the rate of receptor activation, due to the agonist, with space. This causes an inversion of the direction in which the fractional number of active receptors increases across the cell length, and chemorepulsion. To put this another way, cells travel in the direction in which there is most active receptors, which, in a gradient of attractant, is up the gradient. A superimposed gradient of antagonist acts to interfere with this dynamic of receptor activation by keeping receptors in an inactive state, increasingly so at higher concentrations. If this interference is such that the number of active receptors can be made to increase away from the source of attractant, then chemorepulsion is achieved. It has been postulated previously that "chemorepellents," primarily 8-CPT-cAMP, cause an inversion of intracellular dynamics, leading to reverse migration [50, 242]. The results of this thesis would conclude that this inversion actually occurs as a result of an inversion of spatial receptor activation dynamics, which arises due to an interplay between an agonist - which activates receptors - and an inhibitor - which blocks receptors. Furthermore, it has been shown, in Figures 35 and 37 respectively, that 8-CPT-cAMP elicits no chemotactic response in environments treated with caffeine - suppressing cAMP, and agonist, secretion - and elicits reverse migration in environments supplied with a background of agonist. This suggests that cAMP secretion has not been accounted for in previous works, leading to the false assumption that 8-CPT-cAMP is a "chemorepellent," when in fact it is an antagonist interfering with the receptor activation dynamics of unaccounted sources of agonist, leading to the observed chemorepulsion.

Secondly is the dogma that cells are most chemotactically sensitive at K_d concentrations [116]. This is a fundamental, and very widely accepted, principle upon which much science is founded - and its wrong. Considering the most basic chemical configuration from a mathematical perspective, a linear gradient of attractant, it was shown in Figure 8 that the biggest changes in receptor binding with space - leading to the biggest differences in receptor activation across cell extrema and the best chemotaxis - always occur at the smallest concentrations in the gradient. This remained consistent, in a linear regime, regardless of the combination of agonist or antagonist gradients that were considered; the best chemotaxis occurs at low concentrations, not K_d, and these finding were repeatedly recapitulated upon experimental

verification. Interestingly, upon attempting to prove that the best directional cues occur at K_d concentrations - in section 2.2 - an alternative interpretation of the significance of K_d relative to chemotaxis was found. Having K_d located at a certain point in a chemical gradient maximises directional cues at that point, but doesn't optimise chemotaxis relative to the whole gradient. For example, if K_d is located halfway along the gradient, then a cell will chemotax as effectively as is possible halfway along the gradient - but will still chemotax better at the start of the gradient. This interpretation much more accurately matches with observed cellular behaviours throughout this thesis.

Lastly is the dogma that cells requires a minimum of a 1% difference in receptor activation across their length in order to induce chemotaxis [214]; this is also plainly untrue. This can be seen by taking the steepness of active receptors, with space, required to cause a 1% difference in active receptors across a cell length (δ_{min}) and comparing this to the expected steepness of active receptors at each point in space across a chemical gradient ($\delta(x)$). If cells do indeed require this 1% difference, then for any points in space that $\delta(x) < \delta_{min}$ cells will be unable to chemotax, thus allowing one to map out which regions in a given gradient cells should be capable of chemotaxis. This analysis was performed in section 2 and - as illustrated in Figure 2.b - found that a *D. discoideum* of length 10μm should be incapable of chemotaxing over most of a $0 - 2\mu$M linear gradient of Sp-cAMPS. Upon inspection of Figure 9.a, it is clear that cells can actually chemotax well over the entire bridge for this chemical configuration. Working backwards, this would imply that *D. discoideum* are chemotactic down to at least a 0.2% difference in receptor activation across their extrema, perhaps less.

Relative to the above points, it seems that future work should focus on dissecting true K_d mechanics. This is because the role that K_d occupies has clearly been misunderstood, and, as K_d concentrations are crucial for comprehending how external concentrations translate into receptor occupancy - and ultimately cell directional cues - its possible that many chemotaxis investigations have been misinterpreted. It could also be possible that measurements on K_d are also incorrect, leading to further complication and increased margins for misinterpretation. Based on the results of this thesis, it is apparent that there is a sound method for deducing the true K_d for a given agonist. As chemotaxis is maximised at a given point when K_d is located there, it is possible to identify K_d by testing a series of linear gradients. By plotting the resultant cellular velocities for each gradient at a specific point, say halfway along the gradient, there should be a defined maximum in velocity for one of the gradients. The concentration at this point, for this gradient, is where K_d is located. Note that a true maximum must be observed, in other words the gradients above and below the critical gradient must see a reduction in velocity. The only real issue here is mediating a true linear gradient, as many processes - such as receptor recycling and enzymatic degradation - actively work against establishing the required linearity. This becomes easier when one considers *D. discoideum*, however, as many enzyme resistant analogues of cAMP have been manufactured. If the ligand in question is an antagonist then K_d can still be extracted

in the same way, however, there must be a background of agonist with known K_d present, and a more complicated relationship allowing correlation between the point of maximum velocity and the antagonist K_d must be derived. To take this a step further, once the K_d of an agonist - that elicits a linear gradient - has been deduced, it would be a relatively simple process to deduce the true minimum difference in receptor activation across a cell length that is required to induce chemotaxis. All that would be required is to test a particularly shallow, or steep, gradient for which chemotaxis very clearly stops at some point along the gradient. This would be the point for which average x direction velocity drops to 0 μm min^{-1}. Upon plotting the derivative of the active receptor gradient, with space, for this scenario, this point can be easily related to an absolute minimum rate of change of active receptors with space that induces chemotaxis (δ_{min}). The desired minimum can then be found trivially by multiplying δ_{min} by the width of a cell. Note that a very good estimate as to the ligand K_d is required so that the point at which chemotaxis stops can be accurately correlated with active receptor dynamics.

The mechanics underlying many chemotactic behaviours in complex systems, such as the immune system, have remained very much elusive. One such behaviour is that of chemorepulsion of neutrophils back into the vasculature, after chemoattracting to a source of stimulus to engulf and destroy foreign material via phagocytosis. The results of this thesis, however, provide - perhaps for the first time - a strong theory as to what might be occurring here, as well for other complex migration behaviours. Simply put, all that needs to be introduced into a chemotactic system in order to alter migration in unexpected ways is a competing ligand. Specifically, for the case of reverse migration of neutrophils, all that is required is a competitive inhibitor for the same receptor that drove the initial chemoattraction - released at the correct moment and in the correct quantity. This could easily cause the profile of active receptors to invert, driving the cells back into the vasculature via the same molecular mechanisms that mediated the initial chemoattraction. That is what makes this model so elegant: it provides a mechanism by which the biology of complex migration remains exactly the same as the biology of simple migration. There are no secret signalling pathways that have somehow remained undiscovered. Additionally, chemotactic systems in the body tend to involve a large pool of chemokines competing for smaller pool of receptors, so it makes sense that ligand competition can accommodate complex migration behaviours. The main issue seems to be that ligands are studied individually, meaning that any competition based effects are completely missed. For instance, as has been illustrated in this thesis, competitive inhibitors will not elicit any measurable effect on chemotaxis unless competed against an agonist. It is vital to investigate both individual and combined effects of ligands if complex chemotactic behaviours are to be understood.

Some final points should be made discussing chemotaxis models that have come before, in particular the Keller-Segel model [243]. This model provides an explanation of bulk chemotactic trends and pattern formation based on an interplay between cellular density and

a chemical gradient. While this model clearly recapitulates some bulk cellular behaviours there is a vital mechanism missing: binding of ligand molecules to cellular receptors. As has been mentioned previously, cells do not see chemical concentration; what they both see and respond to is information relayed through activated receptors on the cell surface. Therefore, the relationship between cell motion and chemical concentration is indirect, and the relationship between chemical concentration and receptor activation - the missing link as it were - is highly non linear, especially when multiple signals of different intrinsic efficacies are present. This means that there is quite a lot of information missing, and conclusions drawn may be skewed. Furthermore, Keller-Segel models cannot accommodate more than one signal affecting resultant chemotaxis - which is usually the case in any realistic chemotactic system - without causing the model to become arduously complex. As such, the amount of insight that can be obtained is both limited and painful to extract. In comparison, if receptor binding is accounted for then any number of external signals can be included into the model almost trivially, as they reduce to the single quantity of receptor activation. In order to bridge the gap of receptor binding dynamics, and accurately relate changes in chemical concentration to a cellular response, the constants of proportionality present in a Keller-Segel model must be skilfully adapted. While this may work, however, physical relevance and intuitive understanding of these compensatory parameters becomes lost.

7 Conclusion

To conclude, chemotaxis can only be truly understood through comprehension of spatial variations in receptor activation across the cell length. This is because the chemotactic response is proportional to the difference in receptor activation across the cell extrema, with the cell travelling in the direction for which the fractional proportion of active receptors increases. This means that the rate at which the fractional proportion of active receptors changes with space is the key to comprehending chemotaxis. If this quantity is large then there is a correspondingly large difference in receptor activation across the cell length, and strong chemotaxis. If this quantity is negative then the fractional proportion of active receptors is decreasing as the gradient increases, so the cell will travel down the chemical gradient, chemorepelling. Mathematics has proved very effective in bridging the gap between chemical concentration and this crucial quantity of receptor activation, providing an elegant and potent tool for analysing the intricacies of chemotaxis. By considering chemotaxis in this way, any chemical gradient or system of gradients can be mapped to an expected - spatially resolved - chemotactic response, with live cells accurately recapitulating these predictions. As a result of this insight, chemorepulsion - a migration style of which the mechanics have so far proven elusive - has been comprehended with relative ease, with further and unforeseen complexities - such as inversions of chemotactic directionality over the same gradient, or two chemotactic factors that attract in isolation combining to give repulsion - being predicted and successfully verified.

References

[1] Peter JM Van Haastert and Peter N Devreotes. Chemotaxis: signalling the way forward. *Nature reviews Molecular cell biology*, 5(8):626–634, 2004.

[2] Pablo A Iglesias and Peter N Devreotes. Navigating through models of chemotaxis. *Current opinion in cell biology*, 20(1):35–40, 2008.

[3] William G Tharp, R Yadav, D Irimia, A Upadhyaya, A Samadani, O Hurtado, S-Y Liu, S Munisamy, DM Brainard, MJ Mahon, et al. Neutrophil chemorepulsion in defined interleukin-8 gradients in vitro and in vivo. *Journal of leukocyte biology*, 79(3):539–554, 2006.

[4] Anthony W Ford-Hutchinson and Jillian F Evans. [7] neutrophil aggregation and chemokinesis assays. *Methods in enzymology*, 162:72–78, 1988.

[5] Tian Jin, Xuehua Xu, and Dale Hereld. Chemotaxis, chemokine receptors and human disease. *Cytokine*, 44(1):1–8, 2008.

[6] Marco Baggiolini. Chemokines and leukocyte traffic. *Nature*, 392(6676):565–568, 1998.

[7] Bruce Alberts, Dennis Bray, Karen Hopkin, Alexander D Johnson, Julian Lewis, Martin Raff, Keith Roberts, and Peter Walter. *Essential cell biology*. Garland Science, 2015.

[8] Björn Petri and Maria-Jesús Sanz. Neutrophil chemotaxis. *Cell and tissue research*, 371(3):425–436, 2018.

[9] Dominik Alexander Bloes, Dorothee Kretschmer, and Andreas Peschel. Enemy attraction: bacterial agonists for leukocyte chemotaxis receptors. *Nature Reviews Microbiology*, 13(2):95–104, 2015.

[10] Roel P Gazendam, Annemarie van de Geer, Dirk Roos, Timo K van den Berg, and Taco W Kuijpers. How neutrophils kill fungi. *Immunological reviews*, 273(1):299–311, 2016.

[11] Marije B Overdijk, Sandra Verploegen, Marijn Bögels, Marjolein van Egmond, Jeroen J Lammerts van Bueren, Tuna Mutis, Richard WJ Groen, Esther Breij, Anton CM Martens, Wim K Bleeker, et al. Antibody-mediated phagocytosis contributes to the anti-tumor activity of the therapeutic antibody daratumumab in lymphoma and multiple myeloma. In *MAbs*, volume 7, pages 311–320. Taylor & Francis, 2015.

[12] Ulrich H Von Andrian and Charles R Mackay. T-cell function and migration—two sides of the same coin. *New England Journal of Medicine*, 343(14):1020–1034, 2000.

[13] Federica Sallusto, Danielle Lenig, Reinhold Förster, Martin Lipp, and Antonio Lanzavecchia. Two subsets of memory t lymphocytes with distinct homing potentials and effector functions. *Nature*, 401(6754):708–712, 1999.

[14] Edward A Clark and Jeffrey A Ledbetter. How b and t cells talk to each other. *Nature*, 367(6462):425–428, 1994.

[15] Philip M Murphy. The molecular biology of leukocyte chemoattractant receptors. *Annual review of immunology*, 12(1):593–633, 1994.

[16] Beatriz M Tavares-Murta, Mateus Zaparoli, Rogério B Ferreira, Mário León Silva-Vergara, Cristina HB Oliveira, Eddie Fernando C Murta, Sérgio H Ferreira, and Fernando Q Cunha. Failure of neutrophil chemotactic function in septic patients. *Critical care medicine*, 30(5):1056–1061, 2002.

[17] Marianne Bronner-Fraser. Neural crest cell formation and migration in the developing embryo. *The FASEB Journal*, 8(10):699–706, 1994.

[18] Eric Theveneau and Roberto Mayor. Neural crest delamination and migration: from epithelium-to-mesenchyme transition to collective cell migration. *Developmental biology*, 366(1):34–54, 2012.

[19] Mary E Hatten. Central nervous system neuronal migration. *Annual review of neuroscience*, 22(1):511–539, 1999.

[20] John G Parnavelas. The origin and migration of cortical neurones: new vistas. *Trends in neurosciences*, 23(3):126–131, 2000.

[21] JB Angevine and Richard L Sidman. Autoradiographic study of cell migration during histogenesis of cerebral cortex in the mouse. *Nature*, 192(4804):766–768, 1961.

[22] Oscar Marín and John LR Rubenstein. A long, remarkable journey: tangential migration in the telencephalon. *Nature Reviews Neuroscience*, 2(11):780–790, 2001.

[23] TN Behar, MM Dugich-Djordjevic, Y-X Li, W Ma, R Somogyi, X Wen, E Brown, C Scott, RDG McKay, and JL Barker. Neurotrophins stimulate chemotaxis of embryonic cortical neurons. *European Journal of Neuroscience*, 9(12):2561–2570, 1997.

[24] Guo-li Ming, Scott T Wong, John Henley, Xiao-bing Yuan, Hong-jun Song, Nicholas C Spitzer, and Mu-ming Poo. Adaptation in the chemotactic guidance of nerve growth cones. *Nature*, 417(6887):411–418, 2002.

[25] Paul D Griffiths. Schizencephaly revisited. *Neuroradiology*, 60(9):945–960, 2018.

[26] Delphine Denis, Jean-François Chateil, Muriel Brun, Olivier Brissaud, Didier Lacombe, Daniel Fontan, Véronique Flurin, and Jean-Michel Pedespan. Schizencephaly: clinical and imaging features in 30 infantile cases. *Brain and Development*, 22(8):475–483, 2000.

[27] Brian E Richardson and Ruth Lehmann. Mechanisms guiding primordial germ cell migration: strategies from different organisms. *Nature reviews Molecular cell biology*, 11(1):37–49, 2010.

[28] Eleni Mylona, Kristen A Jones, Stephen T Mills, and Grace K Pavlath. Cd44 regulates myoblast migration and differentiation. *Journal of cellular physiology*, 209(2):314–321, 2006.

[29] Kathleen A Molyneaux, Hélène Zinszner, Prabhat S Kunwar, Kyle Schaible, Jürg Stebler, Mary Jean Sunshine, William O'Brien, Erez Raz, Dan Littman, Chris Wylie, et al. The chemokine sdf1/cxcl12 and its receptor cxcr4 regulate mouse germ cell migration and survival. *Development*, 130(18):4279–4286, 2003.

[30] William Gilbert, Robert Bragg, Ahmed M Elmansi, Meghan E McGee-Lawrence, Carlos M Isales, Mark W Hamrick, William D Hill, and Sadanand Fulzele. Stromal cell-derived factor-1 (cxcl12) and its role in bone and muscle biology. *Cytokine*, 123:154783, 2019.

[31] II George Broughton, Jeffrey E Janis, and Christopher E Attinger. The basic science of wound healing. *Plastic and reconstructive surgery*, 117(7S):12S–34S, 2006.

[32] S al Guo and Luisa A DiPietro. Factors affecting wound healing. *Journal of dental research*, 89(3):219–229, 2010.

[33] David M Mosser and Justin P Edwards. Exploring the full spectrum of macrophage activation. *Nature reviews immunology*, 8(12):958–969, 2008.

[34] Gary R Grotendorst, Yoshinao Soma, Kazuhiko Takehara, and Marc Charette. Egf and tgf-alpha are potent chemoattractants for endothelial cells and egf-like peptides are present at sites of tissue regeneration. *Journal of cellular physiology*, 139(3):617–623, 1989.

[35] Mark C Regan, Stephen J Kirk, Hannah L Wasserkrug, and Adrian Barbul. The wound environment as a regulator of fibroblast phenotype. *Journal of Surgical Research*, 50(5):442–448, 1991.

[36] Linda Schneider, Michael Cammer, Jonathan Lehman, Sonja K Nielsen, Charles F Guerra, Iben R Veland, Christian Stock, Else K Hoffmann, Bradley K Yoder, Albrecht Schwab, et al. Directional cell migration and chemotaxis in wound healing response to pdgf-aa are coordinated by the primary cilium in fibroblasts. *Cellular physiology and Biochemistry*, 25(2-3):279–292, 2010.

[37] Marie N Menke, Nathan B Menke, Cecelia H Boardman, and Robert F Diegelmann. Biologic therapeutics and molecular profiling to optimize wound healing. *Gynecologic oncology*, 111(2):S87–S91, 2008.

[38] John Condeelis, Robert H Singer, and Jeffrey E Segall. The great escape: when cancer cells hijack the genes for chemotaxis and motility. *Annu. Rev. Cell Dev. Biol.*, 21:695–718, 2005.

[39] Patrick Mehlen and Alain Puisieux. Metastasis: a question of life or death. *Nature reviews cancer*, 6(6):449–458, 2006.

[40] Evanthia T Roussos, John S Condeelis, and Antonia Patsialou. Chemotaxis in cancer. *Nature Reviews Cancer*, 11(8):573–587, 2011.

[41] Beverly A Teicher and Simon P Fricker. Cxcl12 (sdf-1)/cxcr4 pathway in cancer. *Clinical cancer research*, 16(11):2927–2931, 2010.

[42] Huaiyu Hu. Chemorepulsion of neuronal migration by slit2 in the developing mammalian forebrain. *Neuron*, 23(4):703–711, 1999.

[43] Jonathan R Mathias, Benjamin J Perrin, Ting-Xi Liu, John Kanki, A Thomas Look, and Anna Huttenlocher. Resolution of inflammation by retrograde chemotaxis of neutrophils in transgenic zebrafish. *Journal of leukocyte biology*, 80(6):1281–1288, 2006.

[44] Jennifer Kathleen Quint and Jadwiga Anna Wedzicha. The neutrophil in chronic obstructive pulmonary disease. *Journal of Allergy and Clinical Immunology*, 119(5):1065–1071, 2007.

[45] Sofia De Oliveira, Emily E Rosowski, and Anna Huttenlocher. Neutrophil migration in infection and wound repair: going forward in reverse. *Nature Reviews Immunology*, 16(6):378, 2016.

[46] Mark C Poznansky, Ivona T Olszak, Russell Foxall, Richard H Evans, Andrew D Luster, and David T Scadden. Active movement of t cells away from a chemokine. *Nature medicine*, 6(5):543–548, 2000.

[47] Fabrizio Vianello, Natalia Papeta, Tao Chen, Paul Kraft, Natasha White, William K Hart, Moritz F Kircher, Eric Swart, Sarah Rhee, Giorgio Palù, et al. Murine b16 melanomas expressing high levels of the chemokine stromal-derived factor-1/cxcl12 induce tumor-specific t cell chemorepulsion and escape from immune control. *The Journal of Immunology*, 176(5):2902–2914, 2006.

[48] Kristen M Consalvo, Ramesh Rijal, Yu Tang, Sara A Kirolos, Morgan R Smith, and Richard H Gomer. Extracellular signaling in dictyostelium. *The International journal of developmental biology*, 63(8-9-10):395, 2019.

[49] Edmund William Samuel. Orientation and rate of locomotion of individual amebas in the life cycle of the cellular slime mold dictyostelium mucoroides. *Developmental biology*, 3(3):317–335, 1961.

[50] Louise P Cramer, Robert R Kay, and Evgeny Zatulovskiy. Repellent and attractant guidance cues initiate cell migration by distinct rear-driven and front-driven cytoskeletal mechanisms. *Current Biology*, 28(6):995–1004, 2018.

[51] Jonathan E Phillips and Richard H Gomer. A secreted protein is an endogenous chemorepellant in dictyostelium discoideum. *Proceedings of the National Academy of Sciences*, 109(27):10990–10995, 2012.

[52] Naama Barkai and Stan Leibler. Robustness in simple biochemical networks. *Nature*, 387(6636):913–917, 1997.

[53] Renate Lux and Wenyuan Shi. Chemotaxis-guided movements in bacteria. *Critical Reviews in Oral Biology & Medicine*, 15(4):207–220, 2004.

[54] IJ Uings and SN Farrow. Cell receptors and cell signalling. *Molecular Pathology*, 53(6):295, 2000.

[55] Ioin D Cambell. The modular architecture of leukocyte cell-surface receptors. *Immunological reviews*, 163(1):11–18, 1998.

[56] Borko Amulic, Christel Cazalet, Garret L Hayes, Kathleen D Metzler, and Arturo Zychlinsky. Neutrophil function: from mechanisms to disease. *Annual review of immunology*, 30:459–489, 2012.

[57] Guillaume Gaud, Renaud Lesourne, and Paul E Love. Regulatory mechanisms in t cell receptor signalling. *Nature Reviews Immunology*, 18(8):485–497, 2018.

[58] John T Hancock. *Cell signalling*. Oxford University Press, 2017.

[59] Peter Wallimann, Thomas Marti, Andreas Fürer, and François Diederich. Steroids in molecular recognition. *Chemical reviews*, 97(5):1567–1608, 1997.

[60] Baojun Wang, Mauricio Barahona, and Martin Buck. Amplification of small molecule-inducible gene expression via tuning of intracellular receptor densities. *Nucleic acids research*, 43(3):1955–1964, 2015.

[61] Jun Yang and Morag J Young. The mineralocorticoid receptor and its coregulators. *Journal of molecular endocrinology*, 43(2):53–64, 2009.

[62] Rainer Rupprecht, Johannes MHM Reul, Thorsten Trapp, Bas van Steensel, Christian Wetzel, Klaus Damm, Walter Zieglgänsberger, and Florian Holsboer. Progesterone receptor-mediated effects of neuroactive steroids. *Neuron*, 11(3):523–530, 1993.

[63] Brigitte Anliker and Jerold Chun. Cell surface receptors in lysophospholipid signaling. In *Seminars in cell & developmental biology*, volume 15, pages 457–465. Elsevier, 2004.

[64] Ferdinand HUCHO. The nicotinic acetylcholine receptor and its ion channel. *European journal of biochemistry*, 158(2):211–225, 1986.

[65] Ferdinand Hucho and Christoph Weise. Ligand-gated ion channels. *Angewandte Chemie International Edition*, 40(17):3100–3116, 2001.

[66] Geoffrey Burnstock. P2x ion channel receptors and inflammation. *Purinergic signalling*, 12(1):59–67, 2016.

[67] Bruce Alberts, Alexander Johnson, Julian Lewis, Martin Raff, Keith Roberts, and Peter Walter. Signaling through enzyme-linked cell-surface receptors. In *Molecular Biology of the Cell. 4th edition*. Garland Science, 2002.

[68] Axel Ullrich and Joseph Schlessinger. Signal transduction by receptors with tyrosine kinase activity. *Cell*, 61(2):203–212, 1990.

[69] J Schlessinger and A Ullrich. Growth factor signaling by receptor tyrosine kinases. *Neuron*, 9(3):383–391, 1992.

[70] Zhenfang Du and Christine M Lovly. Mechanisms of receptor tyrosine kinase activation in cancer. *Molecular cancer*, 17(1):1–13, 2018.

[71] François Fagotto and Barry M Gumbiner. Cell contact-dependent signaling. *Developmental biology*, 180(2):445–454, 1996.

[72] E Hafen, B Dickson, T Raabe, D Brunner, N Oellers, and A van der Straten. Genetic analysis of the sevenless signal transduction pathway of drosophila. *Development*, 119(Supplement):41–46, 1993.

[73] Sacha J Holland, Elior Peles, Tony Pawson, and Joseph Schlessinger. Cell-contact-dependent signalling in axon growth and guidance: Eph receptor tyrosine kinases and receptor protein tyrosine phosphatase β. *Current opinion in neurobiology*, 8(1):117–127, 1998.

[74] M Naveen Kumar, Shivaleela Biradar, and RL Babu. Cell signaling and apoptosis in animals. In *Advances in Animal Genomics*, pages 199–218. Elsevier, 2021.

[75] XH Yuan and ZH Jin. Paracrine regulation of melanogenesis. *British Journal of Dermatology*, 178(3):632–639, 2018.

[76] Thomas C. King. 3 - tissue homeostasis, damage, and repair. In Thomas C. King, editor, *Elsevier's Integrated Pathology*, pages 59–88. Mosby, Philadelphia, 2007.

[77] Wolfgang G Junger. Immune cell regulation by autocrine purinergic signalling. *Nature Reviews Immunology*, 11(3):201–212, 2011.

[78] Martin Jechlinger, Andreas Sommer, Richard Moriggl, Peter Seither, Norbert Kraut, Paola Capodiecci, Michael Donovan, Carlos Cordon-Cardo, Hartmut Beug, Stefan Grünert, et al. Autocrine pdgfr signaling promotes mammary cancer metastasis. *The Journal of clinical investigation*, 116(6):1561–1570, 2006.

[79] Mary B Kennedy. Synaptic signaling in learning and memory. *Cold Spring Harbor perspectives in biology*, 8(2):a016824, 2016.

[80] Shih-Chun Lin and Dwight E Bergles. Synaptic signaling between neurons and glia. *Glia*, 47(3):290–298, 2004.

[81] Stanley C Froehner. Regulation of ion channel distribution at synapses. *Annual review of neuroscience*, 16(1):347–368, 1993.

[82] Guilherme Neves, Sam F Cooke, and Tim VP Bliss. Synaptic plasticity, memory and the hippocampus: a neural network approach to causality. *Nature Reviews Neuroscience*, 9(1):65–75, 2008.

[83] Shlomo Melmed, Kenneth S Polonsky, P Reed Larsen, and Henry M Kronenberg. *Williams Textbook of Endocrinology E-Book*. Elsevier Health Sciences, 2015.

[84] Susanne Hiller-Sturmhöfel and Andrzej Bartke. The endocrine system: an overview. *Alcohol health and research world*, 22(3):153, 1998.

[85] Andrew Constanti. *Basic endocrinology for students of pharmacy and allied health sciences*. CRC Press, 1998.

[86] Darcy L Johannsen, Jose E Galgani, Neil M Johannsen, Zhengyu Zhang, Jeffrey D Covington, and Eric Ravussin. Effect of short-term thyroxine administration on energy metabolism and mitochondrial efficiency in humans. *PLoS One*, 7(7):e40837, 2012.

[87] Anne-Gaëlle Lafont, Yi-Fang Wang, Gen-Der Chen, Bo-Kai Liao, Yung-Che Tseng, Chang-Jen Huang, and Pung-Pung Hwang. Involvement of calcitonin and its receptor in the control of calcium-regulating genes and calcium homeostasis in zebrafish (danio rerio). *Journal of bone and mineral research*, 26(5):1072–1083, 2011.

[88] Wesley K Kroeze, Douglas J Sheffler, and Bryan L Roth. G-protein-coupled receptors at a glance. *Journal of cell science*, 116(24):4867–4869, 2003.

[89] Adam I Cygankiewicz, Alicja Maslowska, and Wanda M Krajewska. Molecular basis of taste sense: involvement of gpcr receptors. *Critical reviews in food science and nutrition*, 54(6):771–780, 2014.

[90] Catherine D Strader, Tung Ming Fong, Michael R Tota, Dennis Underwood, and Richard AF Dixon. Structure and function of g protein-coupled receptors. *Annual review of biochemistry*, 63(1):101–132, 1994.

[91] Maria Julia Marinissen and J Silvio Gutkind. G-protein-coupled receptors and signaling networks: emerging paradigms. *Trends in pharmacological sciences*, 22(7):368–376, 2001.

[92] Caitlin D Hanlon and Deborah J Andrew. Outside-in signaling–a brief review of gpcr signaling with a focus on the drosophila gpcr family. *Journal of cell science*, 128(19):3533–3542, 2015.

[93] Susana R Neves, Prahlad T Ram, and Ravi Iyengar. G protein pathways. *Science*, 296(5573):1636–1639, 2002.

[94] Sudarshan Rajagopal and Sudha K Shenoy. Gpcr desensitization: acute and prolonged phases. *Cellular signalling*, 41:9–16, 2018.

[95] Vsevolod V Gurevich and Eugenia V Gurevich. Gpcr signaling regulation: the role of grks and arrestins. *Frontiers in pharmacology*, 10:125, 2019.

[96] Alfred G Gilman. G proteins: transducers of receptor-generated signals. *Annual review of biochemistry*, 56(1):615–649, 1987.

[97] Alfred G Gilman. G proteins and regulation of adenylyl cyclase. *Jama*, 262(13):1819–1825, 1989.

[98] Michael G Ziegler, Hamzeh Elayan, Milos Milic, Ping Sun, and Munir Gharaibeh. Epinephrine and the metabolic syndrome. *Current hypertension reports*, 14(1):1–7, 2012.

[99] Antonio Porcellini, Samantha Messina, Giorgia De Gregorio, Antonio Feliciello, Annalisa Carlucci, Mariavittoria Barone, Antonietta Picascia, Antonio De Blasi, and Enrico V Avvedimento. The expression of the thyroid-stimulating hormone (tsh) receptor and the camp-dependent protein kinase rii β regulatory subunit confers tsh-camp-dependent growth to mouse fibroblasts. *Journal of Biological Chemistry*, 278(42):40621–40630, 2003.

[100] John M Busillo and Jeffrey L Benovic. Regulation of cxcr4 signaling. *Biochimica et Biophysica Acta (BBA)-Biomembranes*, 1768(4):952–963, 2007.

[101] Atsuo T Sasaki and Richard A Firtel. Regulation of chemotaxis by the orchestrated activation of ras, pi3k, and tor. *European journal of cell biology*, 85(9-10):873–895, 2006.

[102] Richard B Clark, Brian J Knoll, and Roger Barber. Partial agonists and g protein-coupled receptor desensitization. *Trends in pharmacological sciences*, 20(7):279–286, 1999.

[103] Charles R Cantor and Paul R Schimmel. *Biophysical chemistry: Part III: the behavior of biological macromolecules*. Macmillan, 1980.

[104] Terrence P Kenakin. *Molecular pharmacology: a short course*. Blackwell science, 1997.

[105] PJ Woodroffe, LJ Bridge, JR King, and SJ Hill. Modelling the activation of g-protein coupled receptors by a single drug. *Mathematical biosciences*, 219(1):32–55, 2009.

[106] Norman Calvey and Norton Williams. *Principles and practice of pharmacology for anaesthetists*. John Wiley & Sons, 2009.

[107] AA Bolonna and RW Kerwin. Partial agonism and schizophrenia. *The British Journal of Psychiatry*, 186(1):7–10, 2005.

[108] Tian Jin. Gradient sensing during chemotaxis. *Current opinion in cell biology*, 25(5):532–537, 2013.

[109] Huaqing Cai and Peter N Devreotes. Moving in the right direction: how eukaryotic cells migrate along chemical gradients. In *Seminars in cell & developmental biology*, volume 22, pages 834–841. Elsevier, 2011.

[110] Zhan Xiao, Ning Zhang, Douglas B Murphy, and Peter N Devreotes. Dynamic distribution of chemoattractant receptors in living cells during chemotaxis and persistent stimulation. *The Journal of cell biology*, 139(2):365–374, 1997.

[111] Tian Jin, Ning Zhang, Yu Long, Carole A Parent, and Peter N Devreotes. Localization of the g protein $\beta\gamma$ complex in living cells during chemotaxis. *Science*, 287(5455):1034–1036, 2000.

[112] Miho Iijima, Yi Elaine Huang, and Peter Devreotes. Temporal and spatial regulation of chemotaxis. *Developmental cell*, 3(4):469–478, 2002.

[113] Theo M Konijn, JG Van De Meene, John T Bonner, and David S Barkley. The acrasin activity of adenosine-3', 5'-cyclic phosphate. *Proceedings of the National Academy of Sciences of the United States of America*, 58(3):1152, 1967.

[114] Jason S King and Robert H Insall. Chemotaxis: finding the way forward with dictyostelium. *Trends in cell biology*, 19(10):523–530, 2009.

[115] John ME Nichols, Douwe Veltman, and Robert R Kay. Chemotaxis of a model organism: progress with dictyostelium. *Current opinion in cell biology*, 36:7–12, 2015.

[116] Peter N Devreotes and Sally H Zigmond. Chemotaxis in eukaryotic cells: a focus on leukocytes and dictyostelium. *Annual review of cell biology*, 4(1):649–686, 1988.

[117] Robert J Eddy, Lynda M Pierini, Fumio Matsumura, and Frederick R Maxfield. Ca2+-dependent myosin ii activation is required for uropod retraction during neutrophil migration. *Journal of cell science*, 113(7):1287–1298, 2000.

[118] Liang Li, Simon F Nørrelykke, and Edward C Cox. Persistent cell motion in the absence of external signals: a search strategy for eukaryotic cells. *PLoS one*, 3(5):e2093, 2008.

[119] Yoshio Fukui. Mechanistics of amoeboid locomotion: signal to forces. *Cell biology international*, 26(11):933–944, 2002.

[120] Orion D Weiner. Regulation of cell polarity during eukaryotic chemotaxis: the chemotactic compass. *Current opinion in cell biology*, 14(2):196–202, 2002.

[121] Carole A Parent and Peter N Devreotes. A cell's sense of direction. *Science*, 284(5415):765–770, 1999.

[122] Chang Y Chung, Satoru Funamoto, and Richard A Firtel. Signaling pathways controlling cell polarity and chemotaxis. *Trends in biochemical sciences*, 26(9):557–566, 2001.

[123] Peter Devreotes and Chris Janetopoulos. Eukaryotic chemotaxis: distinctions between directional sensing and polarization. *Journal of biological chemistry*, 278(23):20445–20448, 2003.

[124] Stephanie Levi, Mark V Polyakov, and Thomas T Egelhoff. Myosin ii dynamics in dictyostelium: determinants for filament assembly and translocation to the cell cortex during chemoattractant responses. *Cell motility and the cytoskeleton*, 53(3):177–188, 2002.

[125] Yu Wang, Chun-Lin Chen, and Miho Iijima. Signaling mechanisms for chemotaxis. *Development, growth & differentiation*, 53(4):495–502, 2011.

[126] Chris Janetopoulos, Tian Jin, and Peter Devreotes. Receptor-mediated activation of heterotrimeric g-proteins in living cells. *Science*, 291(5512):2408–2411, 2001.

[127] Akiko Kumagai, JA Hadwiger, M Pupillo, and Richard A Firtel. Molecular genetic analysis of two g alpha protein subunits in dictyostelium. *Journal of Biological Chemistry*, 266(2):1220–1228, 1991.

[128] Tian Jin. Gpcr-controlled chemotaxis in dictyostelium discoideum. *Wiley Interdisciplinary Reviews: Systems Biology and Medicine*, 3(6):717–727, 2011.

[129] Parvin Bolourani, George B Spiegelman, and Gerald Weeks. Delineation of the roles played by rasg and rasc in camp-dependent signal transduction during the early development of dictyostelium discoideum. *Molecular biology of the cell*, 17(10):4543–4550, 2006.

[130] Yi Elaine Huang, Miho Iijima, Carole A Parent, Satoru Funamoto, Richard A Firtel, and Peter Devreotes. Receptor-mediated regulation of pi3ks confines pi (3, 4, 5) p3 to the leading edge of chemotaxing cells. *Molecular biology of the cell*, 14(5):1913–1922, 2003.

[131] Verena Kolsch, Pascale G Charest, and Richard A Firtel. The regulation of cell motility and chemotaxis by phospholipid signaling. *Journal of cell science*, 121(5):551–559, 2008.

[132] Kyung Chan Park, Francisco Rivero, Ruedi Meili, Susan Lee, Fabio Apone, and Richard A Firtel. Rac regulation of chemotaxis and morphogenesis in dictyostelium. *The EMBO journal*, 23(21):4177–4189, 2004.

[133] Heidi CE Welch, W John Coadwell, Len R Stephens, and Phillip T Hawkins. Phosphoinositide 3-kinase-dependent activation of rac. *FEBS letters*, 546(1):93–97, 2003.

[134] Alice Y Pollitt and Robert H Insall. Wasp and scar/wave proteins: the drivers of actin assembly. *Journal of cell science*, 122(15):2575–2578, 2009.

[135] Thomas H Millard, Stewart J Sharp, and Laura M Machesky. Signalling to actin assembly via the wasp (wiskott-aldrich syndrome protein)-family proteins and the arp2/3 complex. *Biochemical Journal*, 380(1):1–17, 2004.

[136] Oliver Hoeller and Robert R Kay. Chemotaxis in the absence of pip3 gradients. *Current Biology*, 17(9):813–817, 2007.

[137] Leonard Bosgraaf, Ineke Keizer-Gunnink, and Peter JM Van Haastert. Pi3-kinase signaling contributes to orientation in shallow gradients and enhances speed in steep chemoattractant gradients. *Journal of cell science*, 121(21):3589–3597, 2008.

[138] Jianshe Yan, Vassil Mihaylov, Xuehua Xu, Joseph A Brzostowski, Hongyan Li, Lunhua Liu, Timothy D Veenstra, Carole A Parent, and Tian Jin. A g$\beta\gamma$ effector, elmoe, transduces gpcr signaling to the actin network during chemotaxis. *Developmental cell*, 22(1):92–103, 2012.

[139] Tim Lämmermann, Bernhard L Bader, Susan J Monkley, Tim Worbs, Roland Wedlich-Söldner, Karin Hirsch, Markus Keller, Reinhold Förster, David R Critchley, Reinhard Fässler, et al. Rapid leukocyte migration by integrin-independent flowing and squeezing. *Nature*, 453(7191):51–55, 2008.

[140] Anh N Hoang, Caroline N Jones, Laurie Dimisko, Bashar Hamza, Joseph Martel, Nikola Kojic, and Daniel Irimia. Measuring neutrophil speed and directionality during chemotaxis, directly from a droplet of whole blood. *Technology*, 1(01):49–57, 2013.

[141] Vesna Stepanovic, Deborah Wessels, Karla Daniels, William F Loomis, and David R Soll. Intracellular role of adenylyl cyclase in regulation of lateral pseudopod formation during dictyostelium chemotaxis. *Eukaryotic Cell*, 4(4):775–786, 2005.

[142] Yulia Artemenko, Thomas J Lampert, and Peter N Devreotes. Moving towards a paradigm: common mechanisms of chemotactic signaling in dictyostelium and mammalian leukocytes. *Cellular and molecular life sciences*, 71(19):3711–3747, 2014.

[143] Philip M Murphy. International union of pharmacology. xxx. update on chemokine receptor nomenclature. *Pharmacological reviews*, 54(2):227–229, 2002.

[144] Mei-Yu Chen, Robert H Insall, and Peter N Devreotes. Signaling through chemoattractant receptors in dictyostelium. *Trends in genetics*, 12(2):52–57, 1996.

[145] Ning Zhang, Yu Long, and Peter N Devreotes. Gγ in dictyostelium: its role in localization of g$\beta\gamma$ to the membrane is required for chemotaxis in shallow gradients. *Molecular biology of the cell*, 12(10):3204–3213, 2001.

[146] Yan-Jun Liu, Maël Le Berre, Franziska Lautenschlaeger, Paolo Maiuri, Andrew Callan-Jones, Mélina Heuzé, Tohru Takaki, Raphaël Voituriez, and Matthieu Piel. Confinement and low adhesion induce fast amoeboid migration of slow mesenchymal cells. *Cell*, 160(4):659–672, 2015.

[147] Kazuki Nabeshima, Teruhiko Inoue, Yoshiya Shimao, and Tetsuro Sameshima. Matrix metalloproteinases in tumor invasion: role for cell migration. *Pathology international*, 52(4):255–264, 2002.

[148] Ewa K Paluch and Erez Raz. The role and regulation of blebs in cell migration. *Current opinion in cell biology*, 25(5):582–590, 2013.

[149] Martin Bergert, Stanley D Chandradoss, Ravi A Desai, and Ewa Paluch. Cell mechanics control rapid transitions between blebs and lamellipodia during migration. *Proceedings of the National Academy of Sciences*, 109(36):14434–14439, 2012.

[150] NO Carragher, SM Walker, LA Scott Carragher, F Harris, TK Sawyer, VG Brunton, BW Ozanne, and MC Frame. Calpain 2 and src dependence distinguishes mesenchymal and amoeboid modes of tumour cell invasion: a link to integrin function. *Oncogene*, 25(42):5726–5740, 2006.

[151] K Paňková, D Rösel, M Novotnỳ, and Jan Brábek. The molecular mechanisms of transition between mesenchymal and amoeboid invasiveness in tumor cells. *Cellular and molecular life sciences*, 67(1):63–71, 2010.

[152] Evgeny Zatulovskiy, Richard Tyson, Till Bretschneider, and Robert R Kay. Bleb-driven chemotaxis of dictyostelium cells. *Journal of Cell Biology*, 204(6):1027–1044, 2014.

[153] Jose M Mato, Antonia Losada, Vidyanand Nanjundiah, and Theo M Konijn. Signal input for a chemotactic response in the cellular slime mold dictyostelium discoideum. *Proceedings of the National Academy of Sciences*, 72(12):4991–4993, 1975.

[154] Howard C Berg and Edward M Purcell. Physics of chemoreception. *Biophysical journal*, 20(2):193–219, 1977.

[155] Robert M Macnab and Daniel E Koshland. The gradient-sensing mechanism in bacterial chemotaxis. *Proceedings of the National Academy of Sciences*, 69(9):2509–2512, 1972.

[156] Victor Sourjik and Judith P Armitage. Spatial organization in bacterial chemotaxis. *The EMBO journal*, 29(16):2724–2733, 2010.

[157] Victor Sourjik and Ned S Wingreen. Responding to chemical gradients: bacterial chemotaxis. *Current opinion in cell biology*, 24(2):262–268, 2012.

[158] Judith P Armitage and John Michael Lackie. *Biology of the chemotactic response*, volume 46. Cambridge University Press, 1990.

[159] Julius Adler. My life with nature. *Annual review of biochemistry*, 80:42–70, 2011.

[160] Linda Turner, William S Ryu, and Howard C Berg. Real-time imaging of fluorescent flagellar filaments. *Journal of bacteriology*, 182(10):2793–2801, 2000.

[161] Judith P Armitage and Rudiger Schmitt. Bacterial chemotaxis: Rhodobacter sphaeroide and sinorhizobium meliloti-variations on a theme? *Microbiology*, 143(12):3671–3682, 1997.

[162] Gerald L Hazelbauer. Bacterial chemoreceptors. *Current Opinion in Structural Biology*, 2(4):505–510, 1992.

[163] George H Wadhams and Judith P Armitage. Making sense of it all: bacterial chemotaxis. *Nature reviews Molecular cell biology*, 5(12):1024–1037, 2004.

[164] Abu Iftiaf Md Salah Ud-Din and Anna Roujeinikova. Methyl-accepting chemotaxis proteins: a core sensing element in prokaryotes and archaea. *Cellular and Molecular Life Sciences*, 74(18):3293–3303, 2017.

[165] Kyeong Kyu Kim, Hisao Yokota, and Sung-Hou Kim. Four-helical-bundle structure of the cytoplasmic domain of a serine chemotaxis receptor. *Nature*, 400(6746):787–792, 1999.

[166] Julie A Gegner, Daniel R Graham, Amy F Roth, and Frederick W Dahlquist. Assembly of an mcp receptor, chew, and kinase chea complex in the bacterial chemotaxis signal transduction pathway. *Cell*, 70(6):975–982, 1992.

[167] Katherine A Borkovich, Nachum Kaplan, J Fred Hess, and Melvin I Simon. Transmembrane signal transduction in bacterial chemotaxis involves ligand-dependent activation of phosphate group transfer. *Proceedings of the National Academy of Sciences*, 86(4):1208–1212, 1989.

[168] J Fred Hess, Kenji Oosawa, Nachum Kaplan, and Melvin I Simon. Phosphorylation of three proteins in the signaling pathway of bacterial chemotaxis. *Cell*, 53(1):79–87, 1988.

[169] Katherine A Borkovich, Lisa A Alex, and Melvin I Simon. Attenuation of sensory receptor signaling by covalent modification. *Proceedings of the National Academy of Sciences*, 89(15):6756–6760, 1992.

[170] Ganesh S Anand, Paul N Goudreau, and Ann M Stock. Activation of methylesterase cheb: evidence of a dual role for the regulatory domain. *Biochemistry*, 37(40):14038–14047, 1998.

[171] EG Ninfa, Ann Stock, S Mowbray, and J Stock. Reconstitution of the bacterial chemotaxis signal transduction system from purified components. *Journal of Biological Chemistry*, 266(15):9764–9770, 1991.

[172] Joseph J Falke and Gerald L Hazelbauer. Transmembrane signaling in bacterial chemoreceptors. *Trends in biochemical sciences*, 26(4):257–265, 2001.

[173] David F Blair. How bacteria sense and swim. *Annual review of microbiology*, 49(1):489–520, 1995.

[174] Joseph J Falke, Randal B Bass, Scott L Butler, Stephen A Chervitz, and Mark A Danielson. The two-component signaling pathway of bacterial chemotaxis: a molecular view of signal transduction by receptors, kinases, and adaptation enzymes. *Annual review of cell and developmental biology*, 13(1):457–512, 1997.

[175] Snezana Djordjevic and Ann M Stock. Structural analysis of bacterial chemotaxis proteins: components of a dynamic signaling system. *Journal of structural biology*, 124(2-3):189–200, 1998.

[176] J Fred Hess, Robert B Bourret, and Melvin I Simon. Histidine phosphorylation and phosphoryl group transfer in bacterial chemotaxis. *Nature*, 336(6195):139–143, 1988.

[177] Carol L Manahan, Pablo A Iglesias, Yu Long, and Peter N Devreotes. Chemoattractant signaling in dictyostelium discoideum. *Annu. Rev. Cell Dev. Biol.*, 20:223–253, 2004.

[178] Pauline Schaap, Martine van Ments-Cohen, RD Soede, Raymond Brandt, Richard A Firtel, Wolfgang Dostmann, Hans-Gottfried Genieser, Bernd Jastorff, and PJ Van Haastert. Cell-permeable non-hydrolyzable camp derivatives as tools for analysis of signaling pathways controlling gene regulation in dictyostelium. *Journal of Biological Chemistry*, 268(9):6323–6331, 1993.

[179] Huaqing Cai, Chuan-Hsiang Huang, Peter N Devreotes, and Miho Iijima. Analysis of chemotaxis in dictyostelium. In *Integrin and Cell Adhesion Molecules*, pages 451–468. Springer, 2011.

[180] BARBARA VARNUM and DAVID R SOLL. Chemoresponsiveness to camp and folic acid during growth, development, and dedifferentiation in dictyostelium discoideum. *Differentiation*, 18(1-3):151–160, 1981.

[181] Si I Li and Michael D Purugganan. The cooperative amoeba: Dictyostelium as a model for social evolution. *Trends in Genetics*, 27(2):48–54, 2011.

[182] Kenneth B Raper and Nathan R Smith. The growth of dictyostelium discoideum upon pathogenic bacteria. *Journal of bacteriology*, 38(4):431–445, 1939.

[183] Miao Pan, Xuehua Xu, Yong Chen, and Tian Jin. Identification of a chemoattractant g-protein-coupled receptor for folic acid that controls both chemotaxis and phagocytosis. *Developmental cell*, 36(4):428–439, 2016.

[184] Peter Devreotes. Dictyostelium discoideum: a model system for cell-cell interactions in development. *Science*, 245(4922):1054–1058, 1989.

[185] Dirk Dormann, Bakhtier Vasiev, and Cornelis J Weijer. The control of chemotactic cell movement during dictyostelium morphogenesis. *Philosophical Transactions of the Royal Society of London. Series B: Biological Sciences*, 355(1399):983–991, 2000.

[186] Kathy Fosnaugh, Danny Fuller, and William F Loomis. Structural roles of the spore coat proteins in dictyostelium discoideum. *Developmental biology*, 166(2):823–825, 1994.

[187] Hideko Urushihara and Tetsuya Muramoto. Genes involved in dictyostelium discoideum sexual reproduction. *European journal of cell biology*, 85(9-10):961–968, 2006.

[188] MF Filosa and RE Dengler. Ultrastructure of macrocyst formation in the cellular slime mold, dictyostelium mucoroides: extensive phagocytosis of amoebae by a specialized cell. *Developmental biology*, 29(1):1–16, 1972.

[189] Richard H Kessin. *Dictyostelium: evolution, cell biology, and the development of multicellularity*. Number 38. Cambridge University Press, 2001.

[190] Regina Teo, Kimberley J Lewis, Josephine E Forde, W Jonathan Ryves, Jonathan V Reddy, Benjamin J Rogers, and Adrian J Harwood. Glycogen synthase kinase-3 is required for efficient dictyostelium chemotaxis. *Molecular biology of the cell*, 21(15):2788–2796, 2010.

[191] RenéJ W De Wit and Roman Bulgakov. 2-deaminofolic acid elicits desensitization without excitation of the cyclic gmp response in dictyostelium discoideum. *Biochimica et Biophysica Acta (BBA)-Molecular Cell Research*, 887(2):242–247, 1986.

[192] RenéJ W de Wit, Roman Bulgakov, Johan E Pinas, and Theo M Konijn. Relationships between the ligand specificity of cell surface folate binding sites, folate degrading enzymes and cellular responses in dictyostelium discoideum. *Biochimica et Biophysica Acta (BBA)-Biomembranes*, 814(2):214–226, 1985.

[193] Roel VAN DRIEL. Binding of the chemoattractant folic acid by dictyostelium discoideum cells. *European journal of biochemistry*, 115(2):391–395, 1981.

[194] T Julia Sun and PN Devreotes. Gene targeting of the aggregation stage camp receptor car1 in dictyostelium. *Genes & Development*, 5(4):572–582, 1991.

[195] Sonya Bader, Arjan Kortholt, and Peter JM Van Haastert. Seven dictyostelium discoideum phosphodiesterases degrade three pools of camp and cgmp. *Biochemical Journal*, 402(1):153–161, 2007.

[196] Ronald L Johnson, PJ Van Haastert, Alan R Kimmel, CL Saxe 3rd, Bernd Jastorff, and Peter N Devreotes. The cyclic nucleotide specificity of three camp receptors in dictyostelium. *Journal of Biological Chemistry*, 267(7):4600–4607, 1992.

[197] PJ Van Haastert, Bernd Jastorff, Johan E Pinas, and Theo M Konijn. Analogs of cyclic amp as chemoattractants and inhibitors of dictyostelium chemotaxis. *Journal of Bacteriology*, 149(1):99–105, 1982.

[198] Wolfgang RG Dostmann. (r p)-camps inhibits the camp-dependent protein kinase by blocking the camp-induced conformational transition. *FEBS letters*, 375(3):231–234, 1995.

[199] PJ Van Haastert and Erik Kien. Binding of camp derivatives to dictyostelium discoideum cells. activation mechanism of the cell surface camp receptor. *Journal of Biological Chemistry*, 258(16):9636–9642, 1983.

[200] Peter S Klein, Tzeli J Sun, Charles L Saxe, Alan R Kimmel, Ronald L Johnson, and Peter N Devreotes. A chemoattractant receptor controls development in dictyostelium discoideum. *Science*, 241(4872):1467–1472, 1988.

[201] Günther Gerisch. Chemotaxis in dictyostelium. *Annual Review of Physiology*, 44(1):535–552, 1982.

[202] Dale Hereld and Peter N Devreotes. The camp receptor family of dictyostelium. *International review of cytology*, 137:35–47, 1993.

[203] Michael Brenner and Stephen D Thoms. Caffeine blocks activation of cyclic amp synthesis in dictyostelium discoideum. *Developmental biology*, 101(1):136–146, 1984.

[204] Theo M Konijn and Peter JM Van Haastert. Measurement of chemotaxis in dictyostelium. *Methods in cell biology*, 28:283–298, 1987.

[205] David Woznica and David A Knecht. Under-agarose chemotaxis of dictyostelium discoideum. In *Dictyostelium discoideum protocols*, pages 311–325. Springer, 2006.

[206] Evgeny Zatulovskiy and Robert R Kay. Chemotactic blebbing in dictyostelium cells. In *Chemotaxis*, pages 97–105. Springer, 2016.

[207] Gary Laevsky and David A Knecht. Under-agarose folate chemotaxis of dictyostelium discoideum amoebae in permissive and mechanically inhibited conditions. *Biotechniques*, 31(5):1140–1149, 2001.

[208] Hang-jun Wu, Yi-jun Liu, Hui-quan Li, Cong Chen, Ying Dou, Hui-fang Lou, Margaret S Ho, Xiao-ming Li, Zhihua Gao, and Shumin Duan. Analysis of microglial migration by a micropipette assay. *nature protocols*, 9(2):491–500, 2014.

[209] Yulia Artemenko, Kristen F Swaney, and Peter N Devreotes. Assessment of development and chemotaxis in dictyostelium discoideum mutants. In *Cell Migration*, pages 287–309. Springer, 2011.

[210] Carsten Beta and Eberhard Bodenschatz. Microfluidic tools for quantitative studies of eukaryotic chemotaxis. *European journal of cell biology*, 90(10):811–816, 2011.

[211] Noo Li Jeon, Harihara Baskaran, Stephan KW Dertinger, George M Whitesides, Livingston Van De Water, and Mehmet Toner. Neutrophil chemotaxis in linear and complex gradients of interleukin-8 formed in a microfabricated device. *Nature biotechnology*, 20(8):826–830, 2002.

[212] Sally H Zigmond. [6] orientation chamber in chemotaxis. *Methods in enzymology*, 162:65–72, 1988.

[213] Sanjay Chaubey, Anne J Ridley, and Claire M Wells. Using the dunn chemotaxis chamber to analyze primary cell migration in real time. In *Cell Migration*, pages 41–51. Springer, 2011.

[214] Sally H Zigmond. Ability of polymorphonuclear leukocytes to orient in gradients of chemotactic factors. *The Journal of cell biology*, 75(2):606–616, 1977.

[215] Daniel Zicha, Graham A Dunn, and Alastair F Brown. A new direct-viewing chemotaxis chamber. *Journal of cell science*, 99(4):769–775, 1991.

[216] Daniel Zicha, Graham Dunn, and Gareth Jones. Analyzing chemotaxis using the dunn direct-viewing chamber. *Basic Cell Culture Protocols*, pages 449–457, 1997.

[217] Andrew J Muinonen-Martin, David A Knecht, Douwe M Veltman, Peter A Thomason, Gabriela Kalna, and Robert H Insall. Measuring chemotaxis using direct visualization microscope chambers. In *Adhesion Protein Protocols*, pages 307–321. Springer, 2013.

[218] Andrew J Muinonen-Martin, Douwe M Veltman, Gabriela Kalna, and Robert H Insall. An improved chamber for direct visualisation of chemotaxis. *PloS one*, 5(12):e15309, 2010.

[219] Jason M Haugh. Deterministic model of dermal wound invasion incorporating receptor-mediated signal transduction and spatial gradient sensing. *Biophysical Journal*, 90(7):2297–2308, 2006.

[220] Luke Tweedy, Olivia Susanto, and Robert H Insall. Self-generated chemotactic gradients—cells steering themselves. *Current opinion in cell biology*, 42:46–51, 2016.

[221] Luke Tweedy, Peter A Thomason, Peggy I Paschke, Kirsty Martin, Laura M Machesky, Michele Zagnoni, and Robert H Insall. Seeing around corners: Cells solve mazes and respond at a distance using attractant breakdown. *Science*, 369(6507):eaay9792, 2020.

[222] Luke Tweedy, David A Knecht, Gillian M Mackay, and Robert H Insall. Self-generated chemoattractant gradients: attractant depletion extends the range and robustness of chemotaxis. *PLoS biology*, 14(3):e1002404, 2016.

[223] RL Bernstein, M Tabler, D Vestweber, and R Van Driel. Extracellular folate deaminase of dictyostelium discoideum. *Biochimica et Biophysica Acta (BBA)-General Subjects*, 677(2):295–302, 1981.

[224] Andrew J Muinonen-Martin, Olivia Susanto, Qifeng Zhang, Elizabeth Smethurst, William J Faller, Douwe M Veltman, Gabriela Kalna, Colin Lindsay, Dorothy C Bennett, Owen J Sansom, et al. Melanoma cells break down lpa to establish local gradients that drive chemotactic dispersal. *PLoS biology*, 12(10):e1001966, 2014.

[225] Olivia Susanto, Yvette WH Koh, Nick Morrice, Sergey Tumanov, Peter A Thomason, Matthew Nielson, Luke Tweedy, Andrew J Muinonen-Martin, Jurre J Kamphorst, Gillian M Mackay, et al. Lpp3 mediates self-generation of chemotactic lpa gradients by melanoma cells. *Journal of cell science*, 130(20):3455–3466, 2017.

[226] Christine Williams and Stephen J Hill. Gpcr signaling: understanding the pathway to successful drug discovery. *G protein-coupled receptors in drug discovery*, pages 39–50, 2009.

[227] Helen M Roberts, Martin R Ling, Robert Insall, Gabriela Kalna, Julia Spengler, Melissa M Grant, and Iain LC Chapple. Impaired neutrophil directional chemotactic accuracy in chronic periodontitis patients. *Journal of clinical periodontology*, 42(1):1–11, 2015.

[228] Masahiro Ueda, Yasushi Sako, Toshiki Tanaka, Peter Devreotes, and Toshio Yanagida. Single-molecule analysis of chemotactic signaling in dictyostelium cells. *Science*, 294(5543):864–867, 2001.

[229] Douglas A Lauffenburger and Jennifer J Linderman. *Receptors: models for binding, trafficking, and signaling*. Oxford University Press on Demand, 1996.

[230] Péter Érdi and János Tóth. *Mathematical models of chemical reactions: theory and applications of deterministic and stochastic models*. Manchester University Press, 1989.

[231] Terry Kenakin. Quantifying biological activity in chemical terms: a pharmacology primer to describe drug effect, 2009.

[232] Rudolf Gesztelyi, Judit Zsuga, Adam Kemeny-Beke, Balazs Varga, Bela Juhasz, and Arpad Tosaki. The hill equation and the origin of quantitative pharmacology. *Archive for history of exact sciences*, 66(4):427–438, 2012.

[233] Tony Warne, Rouslan Moukhametzianov, Jillian G Baker, Rony Nehmé, Patricia C Edwards, Andrew GW Leslie, Gebhard FX Schertler, and Christopher G Tate. The structural basis for agonist and partial agonist action on a β1-adrenergic receptor. *Nature*, 469(7329):241–244, 2011.

[234] RP Stephenson. A modification of receptor theory. *British journal of pharmacology and chemotherapy*, 11(4):379–393, 1956.

[235] Monica Gotta and Julie Ahringer. Distinct roles for gα and g$\beta\gamma$ in regulating spindle position and orientation in caenorhabditis elegans embryos. *Nature cell biology*, 3(3):297–300, 2001.

[236] Charles Parnot, Stéphanie Miserey-Lenkei, Sabine Bardin, Pierre Corvol, and Eric Clauser. Lessons from constitutively active mutants of g protein-coupled receptors. *Trends in Endocrinology & Metabolism*, 13(8):336–343, 2002.

[237] Michael Renardy and Robert C Rogers. *An introduction to partial differential equations*, volume 13. Springer Science & Business Media, 2006.

[238] JR Lowney and RD Larrabee. The use of fick's law in modeling diffusion processes. *IEEE Transactions on Electron Devices*, 27(9):1795–1798, 1980.

[239] Stanley Ainsworth. Michaelis-menten kinetics. In *Steady-state enzyme kinetics*, pages 43–73. Springer, 1977.

[240] Alice Y Pollitt, Simone L Blagg, Neysi Ibarra, and Robert H Insall. Cell motility and scar localisation in axenically growing dictyostelium cells. *European journal of cell biology*, 85(9-10):1091–1098, 2006.

[241] N OH. Sp-8-cpt-cyclic amps (sodium salt).

[242] Ineke Keizer-Gunnink, Arjan Kortholt, and Peter JM Van Haastert. Chemoattractants and chemorepellents act by inducing opposite polarity in phospholipase c and pi3-kinase signaling. *The Journal of cell biology*, 177(4):579–585, 2007.

[243] Gurusamy Arumugam and Jagmohan Tyagi. Keller-segel chemotaxis models: a review. *Acta Applicandae Mathematicae*, 171(1):1–82, 2021.